January 2015

Fatigue Behavior of Complex Geometries Produced via Additive Manufacturing

Lena Huynh
Purdue University

Graduate School Form 30
Updated 1/15/2015

PURDUE UNIVERSITY
GRADUATE SCHOOL
Thesis/Dissertation Acceptance

This is to certify that the thesis/dissertation prepared

By Lena Huynh

Entitled

Fatigue Behavior of Complex Geometries Produced via Additive Manufacturing

For the degree of Master of Science in Aeronautics and Astronautics

Is approved by the final examining committee:

Prof. Michael Sangid
Chair

Prof. Alten Grandt

Prof. Stephen Heister

To the best of my knowledge and as understood by the student in the Thesis/Dissertation Agreement, Publication Delay, and Certification Disclaimer (Graduate School Form 32), this thesis/dissertation adheres to the provisions of Purdue University's "Policy of Integrity in Research" and the use of copyright material.

Approved by Major Professor(s): Prof. Michael Sangid

Approved by: Prof. Weinong Chen 12/4/2015

Head of the Departmental Graduate Program Date

FATIGUE BEHAVIOR OF COMPLEX GEOMETRIES PRODUCED VIA ADDITIVE MANUFACTURING

A Thesis

Submitted to the Faculty

of

Purdue University

by

Lena Huynh

In Partial Fulfillment of the

Requirements for the Degree

of

Master of Science in Aeronautics and Astronautics

December 2015

Purdue University

West Lafayette, Indiana

ACKNOWLEDGEMENTS

I would firstly like to acknowledge my Major Professor, Dr. Michael Sangid, for his guidance, support and mentorship over the 16 month program. He and his ACME^2 lab group have provided no small amount of help and assistance in getting this research completed. It has been a wonderful experience to work among such a motivated and adventurous group of people. Special mention to John Rotella, for your friendship and support and all of the hours spent helping and supervising me in the SEM despite having mountains of your own work to do.

Thanks also go to my fellow Aussie, Chris Kourloufas, for all your help in getting me settled in the US, and our Coast Guard brethren, Jesse Hyles, Armell Balmaceda and Matt Schibbler for their company during those many hours spent studying.

To Mike Knauf, Becky Cutting and Michael Fruhnert; thank you for your encouragement and friendship. Without you, Purdue, classes and research would not have been the enjoyable and interesting experience that it was.

Lastly, but most wholeheartedly, I'd like to thank the Hyles Family; Jesse, Stacey, Lucas and Olivia (and Harold and Betty), for welcoming me into your family. Purdue would have been a bleak experience without the warmth of your friendship and company.

Thank you.

TABLE OF CONTENTS

Page

Page

Page

Page

LIST OF FIGURES

Figure Page

Figure Page

Figure Page

Figure Page

Figure Page

LIST OF TABLES

ABSTRACT

Huynh, Lena M.S.A.A., Purdue University, December 2015. Fatigue Behavior of Complex Geometries Produced via Additive Manufacturing. Major Professor: Dr. Michael Sangid

Advances in additive manufacturing are enabling the design and production of part geometries that have previously been unrealistic and/or economically infeasible. Direct metal laser sintering, in particular, is an additive manufacturing method that is capable of producing parts from high strength and temperature resistant materials including the nickel-based superalloy, Inconel 718, which is the material used in this thesis.

This present work focuses on two geometries. The first is a test sample with one or two spherical (three-dimensional) voids in the test section; of particular interest was the behavior of the void(s) under fatigue loading, especially, the behavior of two voids as they coalesced. For the geometries tested, fracture surface analysis showed that cracks grew radially from the voids and coalescence occurred secondary to the radial crack growth. Perhaps more interestingly, despite the stress concentration due to the voids, half of the samples failed at locations away from the void(s) indicating that the additively manufacture samples had defects with stress concentrations of similar magnitude to the void(s) elsewhere in the material.

The second geometry is a cellular microlattice or microtruss type structure. The microtrusses were tested under fatigue loading and with a range of stress amplitudes. The failure of the microtrusses was observed and fracture surface analysis carried out on some of the failed ligaments. More work is required to determine the factors that make a ligament susceptible to failure, through preliminary results suggest that surface defects play a significant role. The testing also suggested that the notch sensitivity of the microtruss ligaments decreases as the load is increased.

CHAPTER 1. INTRODUCTION

Rapid prototyping and 3D printing are both terms used to describe the layer-wise production of a part from a Computer-Aided Design (CAD) model, free from the requirements for part-specific process planning and tooling. As the capability of this process has improved and become increasingly economical, industry has recognized that its use has developed beyond prototyping and design and moved into the realms of being a practical production process and technique. The American Society for Testing and Materials (ASTM) technical committee formed to address this process focused on the additive approach common to this technique and adopted the term additive manufacturing [1].

The interest in this technique is two-fold; first, additive manufacturing enables the design and production of part geometries that were unrealistic and/or economically infeasible using traditional methods. Second, additive manufacturing is a relatively new production process whose effect on material properties is yet to be fully quantified.

Additive Manufacturing encompasses a range of methods and associated materials; from vat polymerization, where directed light is used to selectively cure a photopolymer, to extrusion based systems where the base material is melted then extruded through a nozzle to form a layer of a part. Of particular interest to the aerospace industry is Powder Bed Fusion (PBF), where a layer of the base material, in the form of a powder, is spread over

a bed, and a laser then used to sinter or melt a layer of part from the powder. Another layer of powder is spread over the part and the process is repeated. This method, known as Direct Melt Laser Sintering (DMLS), is capable of additively manufacturing a range of high strength and temperature resistant materials including titanium and nickel alloys like Ti6Al4V and Inconel 718 (IN718), both commonly used in the aircraft industry. The nickel-based superalloy, IN718 will be used as the base material in this thesis.

The samples tested as part of this thesis have spherical (3D) void(s) in the center of the test section. Previously, this could only be achieved by techniques like adding impurities to a casting, finding the impurities, then machining a test specimen around them; an onerous and potentially expensive process. With additive manufacturing, these part geometries can be produced consistently and economically. By taking advantage of the unique capability of additive manufacturing, the behavior of a single or a pair of 3D spherical voids, under fatigue loading, can be studied.

The second portion of this thesis looks at cellular structures. Cellular structures are seen extensively in nature and at the very basic level, are packed assemblies of cells that fill space; wood, sea sponges and bone are just a few examples of these structures. Artificial cellular solids have found a myriad of uses, from cushions to insulation. What sets these solids apart is the relative density, a ratio between the density of the cellular structure and the solid material. This can also be expressed as a volume fraction (ratio between the volume of the solid and the volume of the cell. Typically, to be considered a cellular solid, the structure should have a relative density of less than 0.3 [2]. Microlattices or microtrusses like that shown in Figure 1 are cellular solids with high stiffness-to-weight

ratios and the ability to absorb impact loads. They are particularly suited to fabrication via additive manufacturing [3]. The second portion of this research looks at the fatigue behavior of these microtruss structures.

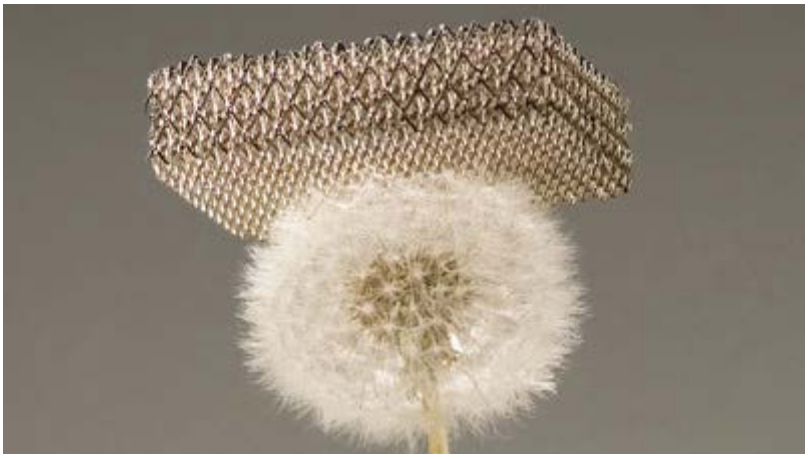

Figure 1 Cellular microlattice structure
formed from hollow Nickel-Phosphorus tubes [4].

CHAPTER 2. LITERATURE REVIEW

2.1 Direct Metal Laser Sintering (DMLS)

Direct Metal Laser Sintering (DMLS) is an additive manufacturing process that uses a laser to sinter a part, layer-by-layer, out of a bed metallic powder. Though this selective laser sintering process can be applied to a range of materials, including thermoplastics and ceramic composites [1], the focus of this research will be on metals. The DMLS process is typically carried out as part of a Powder Bed Fusion (PBF) system. Figure 2 shows a schematic of a PBF process presented by Gibson *et al.* [1] in their text on additive manufacturing. The basis of the process itself is quite simple, a layer of powder is spread over the build platform then the laser sinters the powder into a layer of the part. The build platform drops down and another layer of powder is deposited, ready for sintering. This process is repeated until the entirety of the part is built.

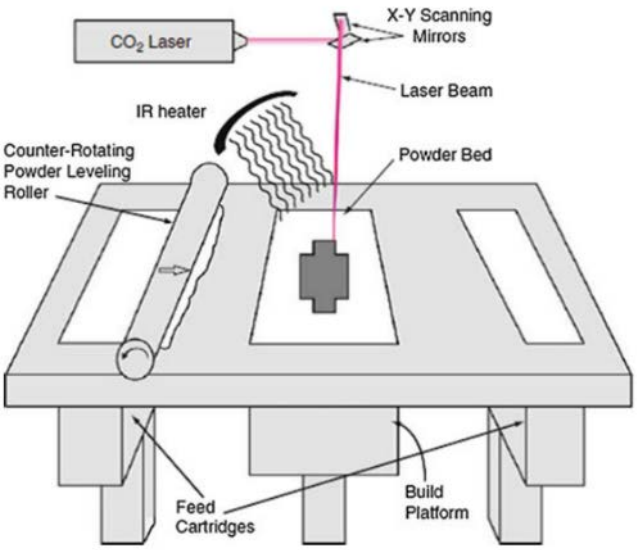

Figure 2 Schematic of a selective laser sintering process ([1] Fig 5.1).

A range of parameters and methods distinguishes one manufacturer's process from another's; these include things like the method of deposition and thickness of the powder layer, and the power and scan speed of the laser. Typically, the process parameters and settings are deemed proprietary by the manufacturer, so the focus of this work will be on connecting structure to performance, neglecting the role of processing.

Though DMLS uses the term sintering, the process used to produce the material tested in this thesis melts the powder and part of the underlying layer. This is sometimes referred to in the literature as Direct Metal Laser Melting (DMLM), which more accurately describes the fabrication process. The advantage of melting over a sintering based approach centers around the rate at which solidification of the material can be achieved. As a process, the sintering rate decreases as the particles agglomerate and fuse (the rate of sintering is proportional to ratio between the free surface area and volume); therefore, to fully sinter a region (i.e. remove all porosity) requires a long time or a high energy. The

limit of the increase in energy is the point where the laser melts rather than sinters the powder layer [1].

2.2 Elastic stress concentration factor – $K_{t\text{-}gross}$ vs $K_{t\text{-}net}$

The choice of nominal stress must be considered when determining the elastic stress concentration factor in a finite body. A stress concentration typically occurs at a reduction in the cross sectional area of a specimen, the stress concentration can therefore be considered a ratio between the maximum stress and the stress in the reduced cross section ($K_{t\text{-}net}$) or a ratio between the maximum stress and the stress in the cross section away from the reduction ($K_{t\text{-}gross}$). $K_{t\text{-}net}$ and $K_{t\text{-}gross}$ can be related via the following expression:

$$K_{t-net} = K_{t-gross} \frac{reduced\ (net)\ cross\ sectional\ area}{gross\ cross\ sectional\ area} \quad (1)$$

In an infinite body $K_{t\text{-}net} = K_{t\text{-}gross}$ as the reduced cross section is approximately equal to the gross cross section.

2.3 Stress concentrations in fatigue

The following is a summary on the effect of notches on fatigue strength based on the information provided in Grandt [5].

The fatigue behavior of a material is typically characterized by testing smooth specimens. However, like the study of stress concentrations under static loads, it is important to understand how stress concentrations behave under fatigue loading. Figure 3 shows the stress life curve of a notched specimen compared to as smooth specimen. Here, the nominal stress is the remote stress applied to the specimen. The fatigue performance of

the notched specimen is typically worse than that of the smooth specimen. Depending on the material, the difference may reduce at higher loads due to plastic deformation at the crack tip.

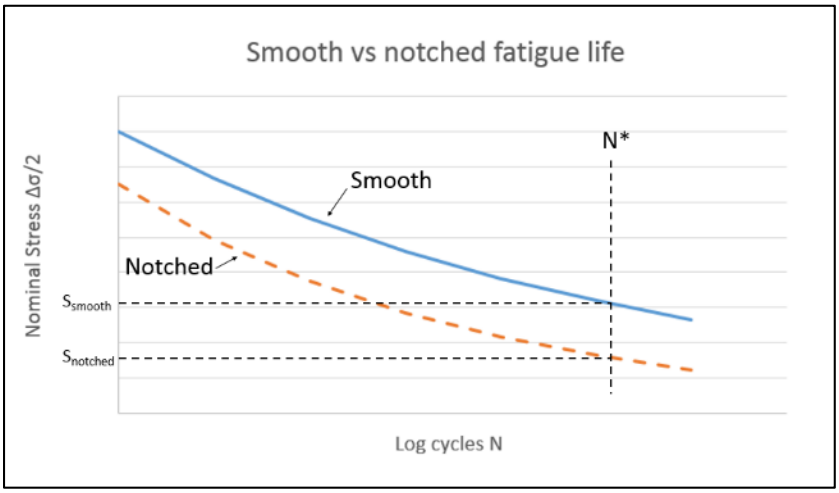

Figure 3 Comparison between smooth and notched fatigue life, based on Figure 9.15 [5].

For a given life (N*), the ratio between the nominal applied stress for the smooth specimen (S_{smooth}) and the notched specimen ($S_{notched}$) gives the fatigue notch concentration factor (K_f). K_f is analogous to K_t, the elastic stress concentration factor in static loading.

$$K_f = \left.\frac{S_{smooth}}{S_{notch}}\right|_{Life\ N^*} \tag{2}$$

K_f is usually given based on an N* in the high cycle fatigue regime (10^6 – 10^7 cycles) and with zero mean stress. Typically $1 \leq K_f \leq K_t$; if $K_f = K_t$ then the notch is considered fully effective, in other words, the material remains fully elastic, which is the case for brittle materials. If $K_f = 1$, then the notch is considered to have no effect on the fatigue life.

Note that K_f will vary depending on the fatigue life (N*) at which S_{smooth} is compared to $S_{notched}$.

Equation (3) gives the expression for the notch sensitivity factor, q, which compares the elastic stress concentration factor with the fatigue notch concentration factor.

$$q = \frac{K_f - 1}{K_t - 1} \tag{3}$$

The notch sensitivity factor is typically $0 \leq q \leq 1$. With q = 0 being a material that is notch insensitive and q = 1 being completely notch sensitive. Note that since K_f (fatigue notch concentration factor) varies with the N* value at which it is measured, q is also dependent on the N* value at which it is measured.

Both Neuber [6] and Peterson [7] developed approximations for q [8]:

Neuber: $$q = \frac{1}{1 + \sqrt{\frac{\rho^*}{r}}} \tag{4}$$

Peterson: $$q = \frac{1}{1 + \frac{\alpha^*}{\rho}} \tag{5}$$

Where ρ^* and α^* are characteristic lengths for a material and r and ρ are the notch-tip radii. Empirical values for the characteristic lengths are available for some materials (primarily steels) but are not available for IN718.

Quantification of notch behavior in fatigue is almost exclusively conducted under load (i.e. stress) control due the difficulty in measuring and controlling for strain in the vicinity of the notch. Additionally, even under load-controlled cycling, the notch

typically sees strain-controlled cycling due to the constraining effect of the surrounding material ([5] p267). Load controlled fatigue testing is addressed in ASTM E466 *Standard Practice for Conducting Force Controlled Constant Amplitude Axial Fatigue Tests of Metallic Materials* [9].

2.4 Microtruss structures

Cellular structures are desirable for their high stiffness-to-weight ratios and ability to absorb impact [3]. Metal foams, in particular, have great potential for use in lightweight sandwich structures [10]. However, the stochastic nature of traditional foamed metals, like that described by Gibson [2], result in inhomogeneity within the structure. When used in designs, this inhomogeneity must be managed conservatively, making the foamed metal less suitable for use in structures that require a high level of optimization [11]. The homogeneity of microlattice or microtruss designs offer an attractive alternative to the metal foams while retaining or improving on the characteristics that make cellular structures so desirable [12].

Prior to additive manufacturing, regular microtruss designs were formed via techniques like gluing and stacking corrugated sheets ([2] page 4) or weaving wire arrangements [13]. These methods are capable of producing a very limited range of cellular designs. Additive manufacturing removes the manufacturing restrictions on cellular designs enabling complex three-dimensional cellular structures to be built and tested experimentally, though it does come with its own concerns and issues [3].

Research into additively manufactured cellular structures is focused on three different but related aspects [14]. The first is the design and mechanical response of the cellular

structure [3, 11], the second is the mechanical performance of the bulk additively manufactured material based on processing parameters and post-processing treatments [15, 16], the third is the most relevant to this thesis, and addresses the microstructure specific to additively manufactured cellular structures and its effect on performance and response [14, 17].

Experimental testing of microtruss structures in compressive fatigue showed failure was precipitated by the localization of strain in the structure. The strain localization began with fatigue cracking in some of the ligaments, followed by extensive cracking and ligament failure. Fracture surface analysis of the failed ligaments found that the fatigue cracking initiated at the root of defects on the surface of the ligament and highlighted the importance of surface finish on the fatigue life of the microtruss [17].

CHAPTER 3. EXPERIMENTAL SETUP

3.1 Actuator, load frame and transducer

The custom-built MTS load frame shown in Figure 4a was used to apply the loads to the samples. An MTS model 244.12 hydraulic actuator applied the loads; the actuator was capable of applying 25 kN with a dynamic stroke of 76 mm. The samples were gripped using the 30 kN advantage edge action grips shown in Figure 4b. The loads were measured using an MTS model 661.20E-01 force transducer with a capacity of 25 kN.

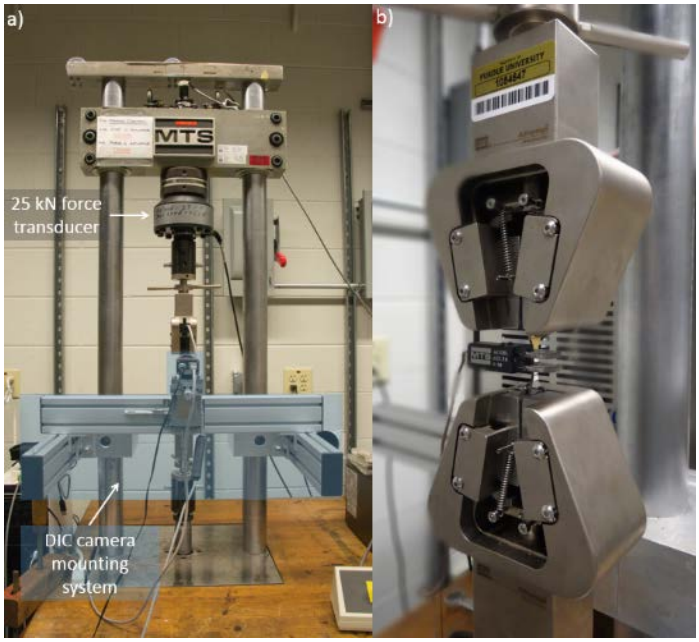

Figure 4 MTS actuator, load frame and grips.
a) MTS actuator and load frame used to apply the loads to the samples. The DIC camera mounting system is shaded in blue. b) 30 kN MTS Advantage wedge action grips.

The MTS was controlled using MTS TestSuite ™ Multipurpose Elite Software. This software allows the user to build test sequences to be run on the MTS. The test sequence for the majority of the samples was a sinusoidal, force controlled, fatigue test that would pause at user-defined intervals to allow DIC images of the sample to be acquired. The test also controlled data acquisition and break detection.

3.2 Extensometer

An MTS Model 632.26 B-30 clip on extensometer (gage length = 0.3” or 7.62 mm) was used to measure strain in the sample. Figure 5a shows the extensometer attached to a sample in situ. The extensometer had to be small enough to fit between the grips during testing. Figure 5b shows an ex situ image of the extensometer. The springs around the half-moon sections hold the specimen against the knife edges shown in Figure 5c. The knife edges are pointed and double beveled to ensure the extensometer does not slip on the sample. This was necessary given the hardness of the sample material.

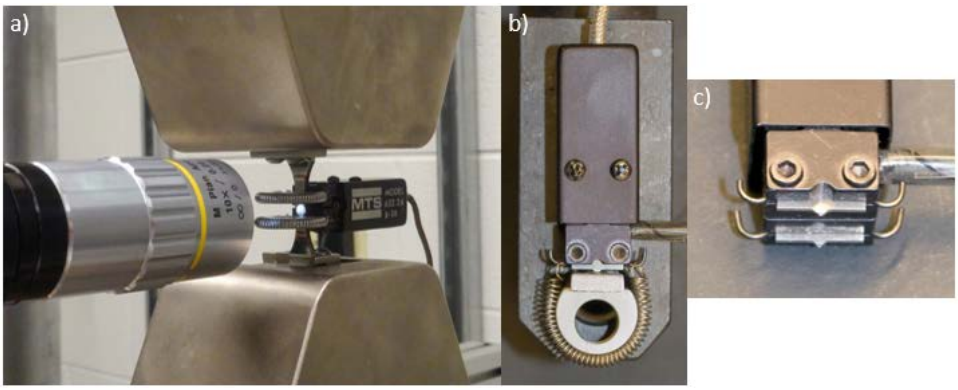

Figure 5 Extensometer used during testing.
a) Extensometer attached to sample in situ. b) Extensometer attached to a dummy sample ex situ showing the spring and half-moon sections holding the sample against the knife edges. c) Close-up of the pointed, double-beveled knife edges.

The extensometer was primarily used to determine the stress-strain data used to characterize the material. One of each of the void samples was also tested with the extensometer in place. The extensometer use was then discontinued as there was concern that cracks were initiating where the knife edge touched the specimen, though fracture surface analysis later determined that this was not the case.

3.3 Digital Image Correlation (DIC)

In situ digital image correlation was used in an attempt to measure the strain on the surface of the sample. The approach to the DIC was adjusted based on the sample. A pattern was stamped onto the surface of the void samples whereas the surface roughness was used for the microtrusses samples.

3.3.1 Image acquisition

DIC images were acquired using an Allied Vision Technologies Manta Model 201B 14 Megapixel camera, capable of up to 14 fps. The camera was mounted to a Newport 462-XYZ-M ULTRAlign™ Precision Integrated Crossed-Roller Bearing Linear Stage allowing the camera to be precisely adjusted in three dimensions. The linear stage was mounted to a framework that was attached to the upright columns of the load frame. The framework allowed the position of the linear stage to be coarsely adjusted while keeping the camera in a fixed position for the duration of the testing.

Figure 6 shows the image acquisition setup for the void samples. In this case, a 10x Mitutoyo lens with a working distance of 33.5 mm was used to magnify the image. The lens was coupled to the camera using a Navitar coupling system, which included an in-line lighting attachment. The lighting had two intensity settings though only the lowest

setting was used. This setup is capable of imaging an area approximately 750 μm wide and 580 μm tall.

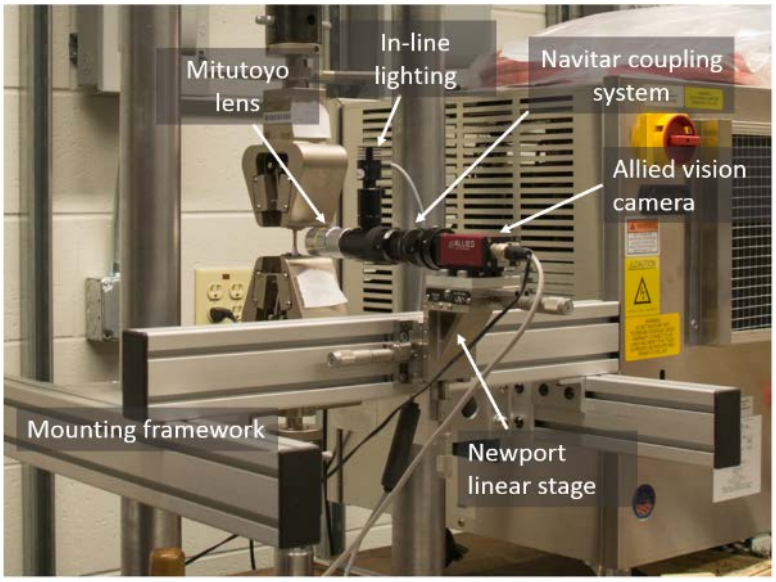

Figure 6 DIC Image acquisition system setup for void samples.

Figure 7a shows the image acquisition setup for the microtruss samples. The aim of the system was to image the entire microtruss as shown in Figure 7b (an area of approximately 20 mm x 20 mm). A 0.5x Navitar lens was used to acquire the image, this required adjustment of the mounting framework to accommodate the 24” working distance. Due to the distance between the camera and the microtruss, and the surface roughness of the microtruss, the in-line lighting was insufficient. Instead, an annular light was mounted close to the sample instead. The image was acquired through the center of the light source.

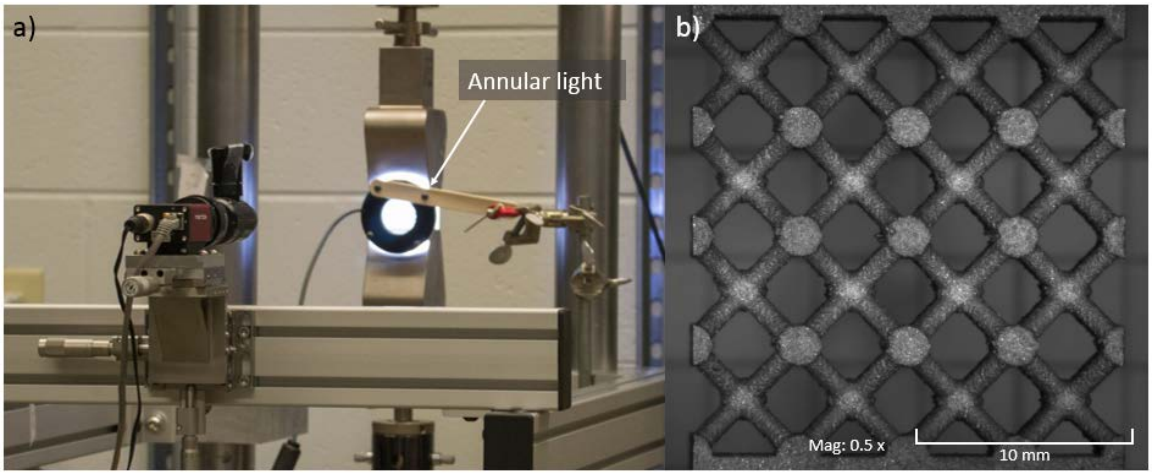

Figure 7 Digital Image Correlation (DIC) Setup.
a) DIC image acquisition system setup for microtruss samples.
b) Acquired microtruss image.

Allied Visions GigE Viewer software was used to capture the images. Images were acquired manually while the fatigue test program paused at maximum load. For one of the microtruss samples, though DIC images were taken using the GigE Viewer software, Matlab's Image Acquisition App was also used to record video of the microtruss undergoing the fatigue loading and failure.

3.3.2 Image processing

Digital Image Correlation (DIC) of the acquired images was conducted in Vic-2D, a software program produced by Correlated Solutions. The program compares the images of deformed samples with an undeformed (reference) image. The movement of patterns on the surface of the sample is tracked and the movement determines the change in pixel location, which is then differentiated to calculate strain. The result is a 2D strain map of the surface of the sample.

The Vic 2D output can be used directly or exported as a .csv file and manipulated and plotted in Matlab. Doing so, allows the user to scale the data, if required, and gives the user greater control over the plotting and color scale. In this case, a colormap has been developed that plots the data so that tension is red and compression is blue. White was used to indicate the absence of strain. Figure 8 shows the original, strained, DIC image with a comparison between the default Vic 2D/Matlab color scale and the developed user defined scale. The user defined scale more intuitively differentiates between tension and compression in the sample.

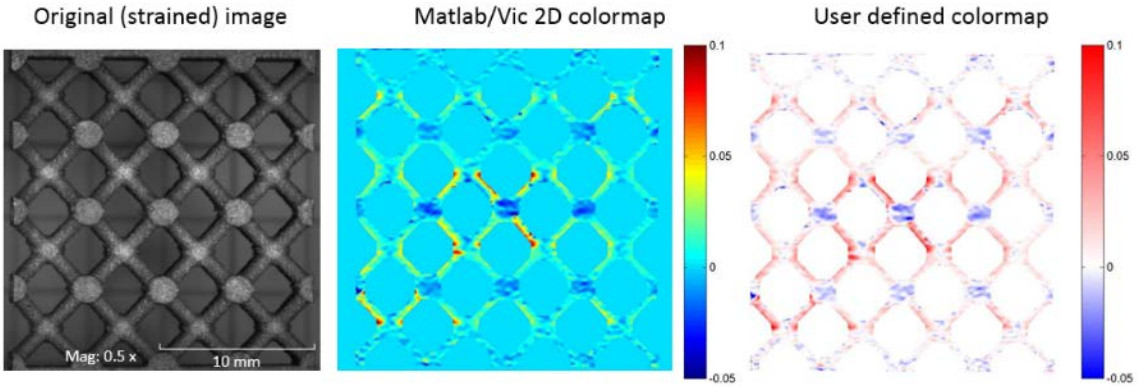

Figure 8 Comparison between DIC image, Vic 2D and Matlab results.
This image compares the default Vic 2D/Matlab strain map and the strain map produced by the user-defined scale that shows tension in red and compression in blue. The image is of a microtruss at maximum load after 4855 cycles of fatigue loading.

3.3.3 Void samples

The accuracy of the DIC can be enhanced by applying a high contrast pattern to the surface [18]. Figure 9 is an in situ image of the applied pattern taken with the image acquisition setup shown in Figure 6. The pattern was applied to the surface using the method detailed in [18].

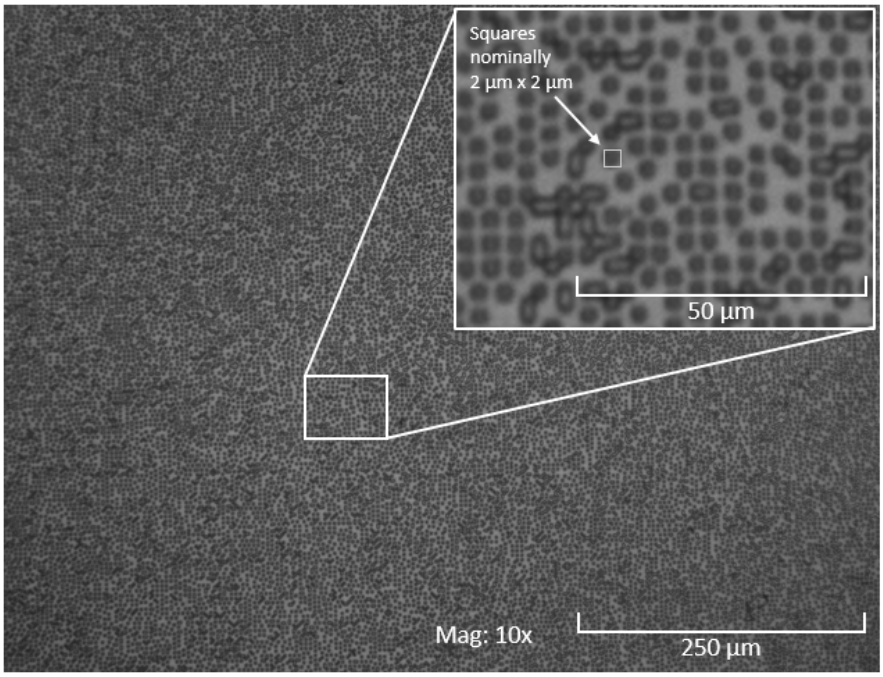

Figure 9 Pattern applied to the surface of the void samples.
Each square is nominally 2 µm.

A major issue with DIC was movement of the sample towards and away from the camera. Some small movement is expected due to the Poisson effect of the load applied to the sample but some of the movement may have been a result of poor grip alignment. Since the strain being measured is very small, any movement towards or away from the camera was interpreted by the DIC software as an expansion or contraction of the sample. This issue was exacerbated by the small focus depth (3.5 µm) of the 10x lens, as any movement also required the image to be refocused, which introduced more variation to the images.

Additionally, if the camera and the sample are not perfectly aligned, then only a portion of the DIC image is in focus. In taking in situ images, care had to be taken to ensure that the same area in successive images was in focus.

The average strain results as a function of the number of cycles for one of the void samples is shown in Figure 10. The convention in Vic 2D gives tension as a positive strain, the results in Figure 10 show that Vic 2D has calculated that the sample is in compression and that the sample becomes more compressed as the fatigue loading continues. These results are obviously incorrect.

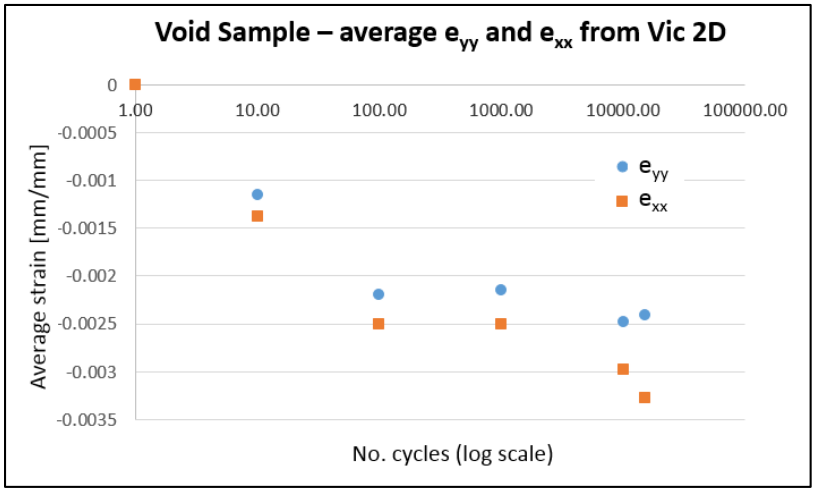

Figure 10 Plot showing Vic 2D strain outputs for a void sample.

Except for the initial image, all of the DIC images are taken while the sample is at maximum load. If the issue were with only the initial image, then the average strain would show an increasing trend as strain accumulated in the sample due to the fatigue loading. Instead, Figure 10 shows a decreasing trend in the average strain. This may have been caused by the Poisson contraction of the sample, but ultimately means that the strain data from Vic 2D is not usable as a quantitative measure of strain in the sample. Further investigation into the cause of the incorrect strain readings is required if the strain results are to be used quantitatively in future tests.

However, the data is useful in showing relative strain in a particular image. For example, Figure 11 shows the DIC image and the corresponding strain map after just one cycle (note that the images are taken at maximum load). The strain map shows a region of relatively high strain that initiates and grows into the crack seen in the DIC image at 25,000 cycles (the crack is first recorded as breaching the surface in the DIC image taken at 15,000 cycles).

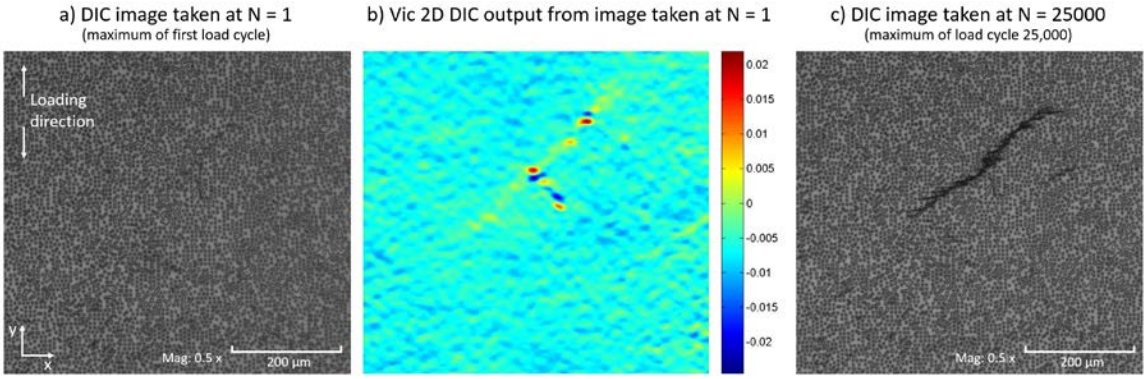

Figure 11 DIC images and outputs from a void sample.
a) DIC image taken during the first cycle while the sample is under maximum load. b) The Vic-2D strain map (e_{yy}) of the image shown in a). The image was compared to an unloaded reference image. Note the region of relatively high strain. c) The same area at maximum load after 25,000. Note that a crack has developed in the region that had relatively high strain after just one cycle.

The DIC images of the void samples were taken with the expectation that the images could be used to quantitatively measure the strain and determine local strain accumulation in the sample. Unfortunately, the results demonstrated that the images could only be used to qualitatively show relative strain accumulation in a particular image.

3.3.4 Microtruss samples

The extensometer that was used on the void samples could not be used on the microtruss due to the geometry of the sample. Instead, the plan was to use the DIC images to measure strain. Unlike the void samples, since the microtruss surface was left in its as-delivered state, the surface roughness was able to provide sufficient contrast to allow DIC without further the requirement to apply a pattern to the surface. An example of the DIC microtruss images is shown in Figure 12a.

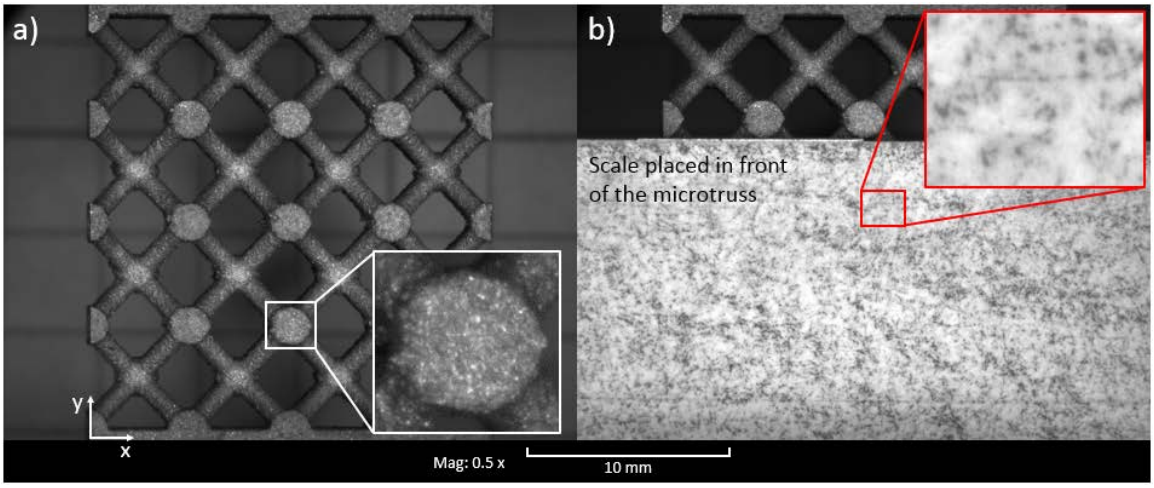

Figure 12 Image for Microtruss DIC.
a) Image of the microtruss taken for DIC showing a zoomed-in view of the surface.
b) Image of the microtruss and undeformed scale used to quantify movement towards and away from the camera. A scale image like this one was taken each time an image for DIC was taken.

To try and avoid some of the issues that were seen in processing the DIC images of the void samples, a scale image was used to try and quantify the change in strain due to movement of the sample towards and away from the camera. A number of materials and patterns were tested in order to find something suitable for use as a scale. The ideal scale was something that was stiff, so it could be held flush against the sample, and thin, so that

the image focus would not require adjustment. The scale would also need to be high contrast and have sufficient random feature density to be appropriate for DIC.

The DIC image of selected scale design is shown in Figure 12b. The scale consisted of a high-contrast pattern, in this case graphite on a yellow sheet of paper, attached to a thin sheet of steel. The yellow paper produced better images than white paper due to the intensity of the lightning. Transparent matte tape was applied to the surface of the scale to reduce glare. A photo of the scale is shown in Figure 13.

Figure 13 Scale used in the microtruss scale images.

The scale was held flush against the sample. Since the scale was not loaded, any apparent change in the scale was due to movement of the scale (and the microtruss) towards or away from the camera. Figure 14 shows the average strain calculated for the scale. The average apparent strain values were then used to scale the strain maps of the microtruss.

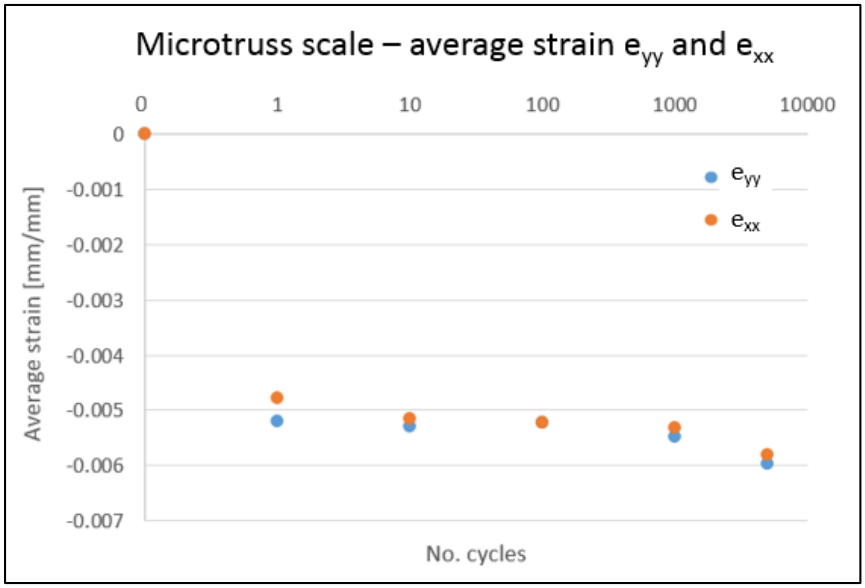

Figure 14 Average apparent strain in the microtruss scale due to movement away from the camera.

To confirm the scaling, ImageJ (an image processing program) was used to measure the change in length of the microtruss over the first cycle; while the sample was unloaded, at minimum load and at maximum load. The calculated strain values did not agree with the average scaled strain values calculated by Vic 2D using the DIC images. This meant that, again, the strain maps from the DIC could only be used to qualitatively describe the strain in the sample. However, as shown in Figure 15, the DIC results at least show that the average strain in the microtruss is increasing, as would be expected, meaning that successive microtruss images and DIC results can be qualitatively compared.

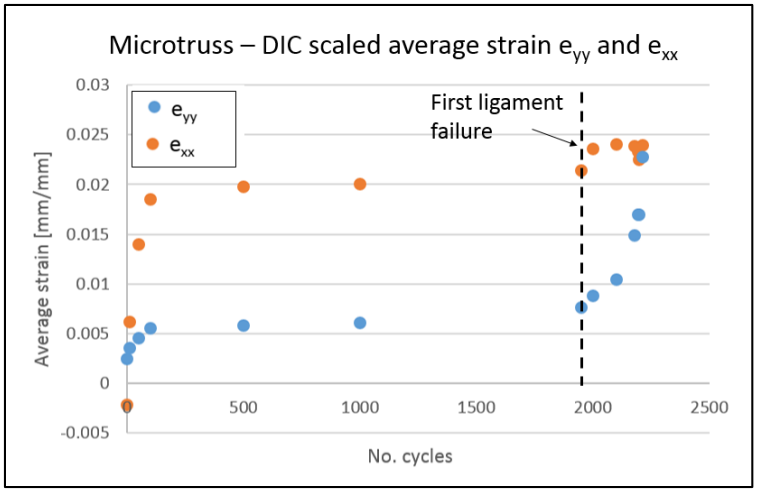

Figure 15 Average strain accumulated in a microtruss sample calculated via DIC. The data has been scaled using the associated scale data. The strain initially increases, then plateaus. The increase in the latter part of the plot starts after the first ligament failure.

3.3.5 DIC Summary

Images of the void and microtruss samples were acquired with the intent to conduct DIC to determine the average and local strain accumulation. For the void samples, processing of these images in Vic 2D immediately showed that the results were incorrect, as the samples appeared to be compressing rather than expanding. This was likely due to the movement of the sample towards or away from the camera. In an attempt to correct for this movement, an image of an undeformed scale was recorded for each of the DIC images of the microtruss. After scaling, the microtruss DIC results showed the correct trend, with strain accumulation in tension. However, the average strain from the DIC measurements did not agree with the gross measurements of microtruss elongation completed in ImageJ. So again, the results from DIC could not be used quantitatively. However, since the trend in the strain was correct, successive microtruss DIC results can be qualitatively compared.

CHAPTER 4. MATERIAL CHARACTERIZATION

4.1 Material Production and Processing

The material used in the samples is EOS (Electro Optical Systems) Nickel-based superalloy Inconel 718 (IN718), a high-strength, fatigue, corrosion and heat resistant material, with powder developed specifically for fabrication via DMLS. The EOS IN718 meets the composition specifications of AMS 5662 [19] which describes composition, treatments, and minimum properties for IN718 in the form of bars and forgings. The datasheet for the EOS Nickel alloy IN718 [20] is provided in appendix A. The composition by weight is summarized in Table 1.

Table 1 EOS Nickel alloy IN718 Composition [20]

EOS IN718 composition limits (wt. %)		
	Min	Max
Ni	50	55
Cr	17	21
Nb	4.75	5.5
Mo	2.8	3.3
Ti	0.65	1.15
Al	0.2	0.8
Co	≤ 1	
Cu	≤ 0.3	
C	≤ 0.08	

Si	≤ 0.35
Mn	≤ 0.35
P	≤ 0.015
S	≤ 0.015
B	≤ 0.006
Fe	(balance)

The samples were produced by GPI Prototyping and Manufacturing Services[1] using an EOSINT M 290 Direct Metal Laser Melting (DMLM) machine. The M 290 has a maximum build volume of 250 mm x 250 mm x 325 mm and uses a 400W Yb-fiber laser.

The build process exposes the samples to large temperature gradients, leaving significant residual stress in the samples. As standard procedure, GPI stress relieves all additively manufactured parts, in order to reduce part warpage when removing the components from the build plate. The samples were stress relieved at 1065° C (± 4°C) for 1.5 hours (-5/+15 minutes) with a 2 – 4 Bar Argon quench.

The samples were heat treated in accordance with AMS 5662 [19]. The treatment consisted of solution annealing followed by ageing/precipitation hardening, in order to achieve the desired morphology and distribution of the γ'' precipitate structure in the IN718 material. GPI carried out this heat treatment with the following parameters:

- Solution annealing: 980°C for 1 hour with an air (/argon) cool

[1] 940 North Shore Drive, Lake Bluff, IL 60044, tel: (847) 615-8900, web: http://gpiprototype.com/

- Ageing treatment: 720°C for 8 hours, furnace cool to 620° in 2 hours, hold at 620°C for 8 hours then an air (/argon) cool

Two additional processes could have been carried out on the material; Hot Isostatic Pressing (HIP) and homogenization. HIP has been shown to minimize porosity in materials produced via DMLS with the expected improvement in crack initiation life [15]. This process was not carried out due to concerns that the HIP would close the voids intentionally placed in the void samples or that the high temperatures would provide sufficient energy to sinter the powder that remained in the voids into a solid mass. Though they did not contain intentional voids, the microtruss samples were not HIP'ed to maintain consistency with the void samples.

Homogenization of IN718 coarsens the grains and forms a more isotropic microstructure. Adding homogenization to the standard solution heat treatment and aging has been shown to increase the ductility of the material at the cost of a slight reduction in ultimate and yield strength [16]. Like HIP, homogenization was not carried out on the material due to concerns that the high temperature would sinter and partially melt the power remaining in the voids. Though the process would have been suitable for the microtruss samples, the samples were not homogenized to maintain consistency with the void samples.

4.2 Material Properties

A pristine EOS Nickel Alloy IN718 sample, i.e. one without voids, was tested in a monotonic tension test to characterize the material produced and heat treated by GPI. Figure 16 shows the stress-strain curve from the tension test as well as a comparison curve for similarly treated IN718 bar from MIL-HDBK-5J [21]. From this curve, values

for the elastic modulus (E), proportional limit, yield stress (σ_y) and failure stress (σ_f) were determined, these are summarized in Table 2.

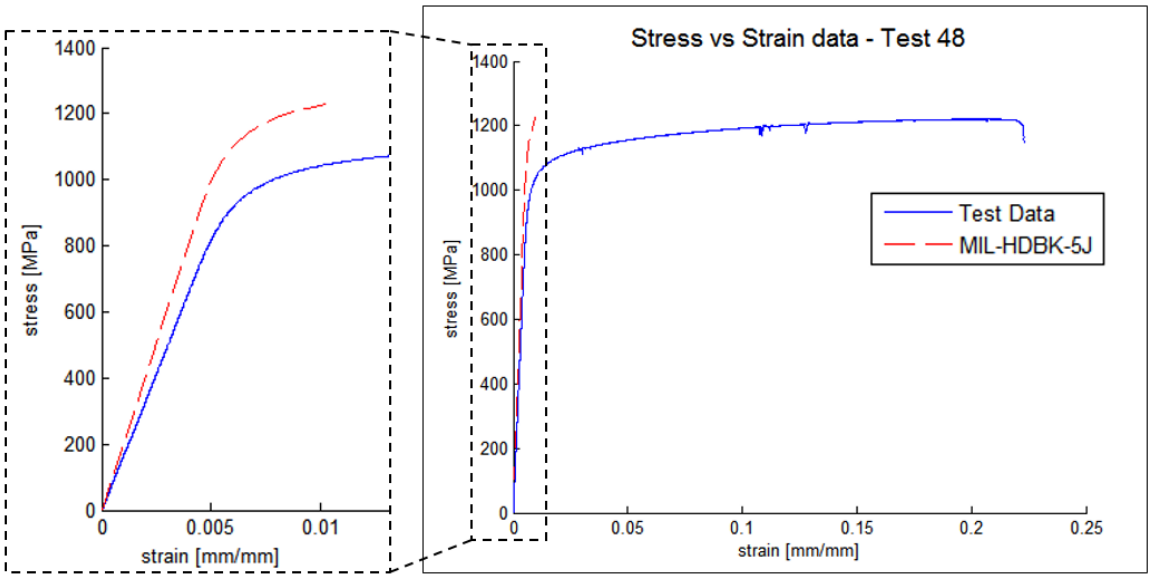

Figure 16 Stress-strain curve from the monotonic tension test compared to the properties for similarly treated IN718 bar at room temperature presented in MIL-HDBK-5J figure 6.3.5.1.6(b) [21].

The curve is linear to approximately 700 MPa. A linear regression was fitted to the linear portion of the curve using Matlab's polyfit function, the elastic modulus, E, is determined from the slope of this line. The elastic modulus was determined to be 166.45 GPa, this is within the limits given by the manufacturers data sheet (170 ± 20 GPa) for the samples' build direction and heat treatment [20].

Figure 17 shows the plots and points used to determine the proportional limit and 0.2% yield stress. The proportional limit was determined to be at 734.60 MPa and the 0.2% yield stress at 1005.77 MPa. The yield stress is below the manufacturer's reported minimum of 1034 MPa and outside of the typical range of 1150 ± 100 MPa.

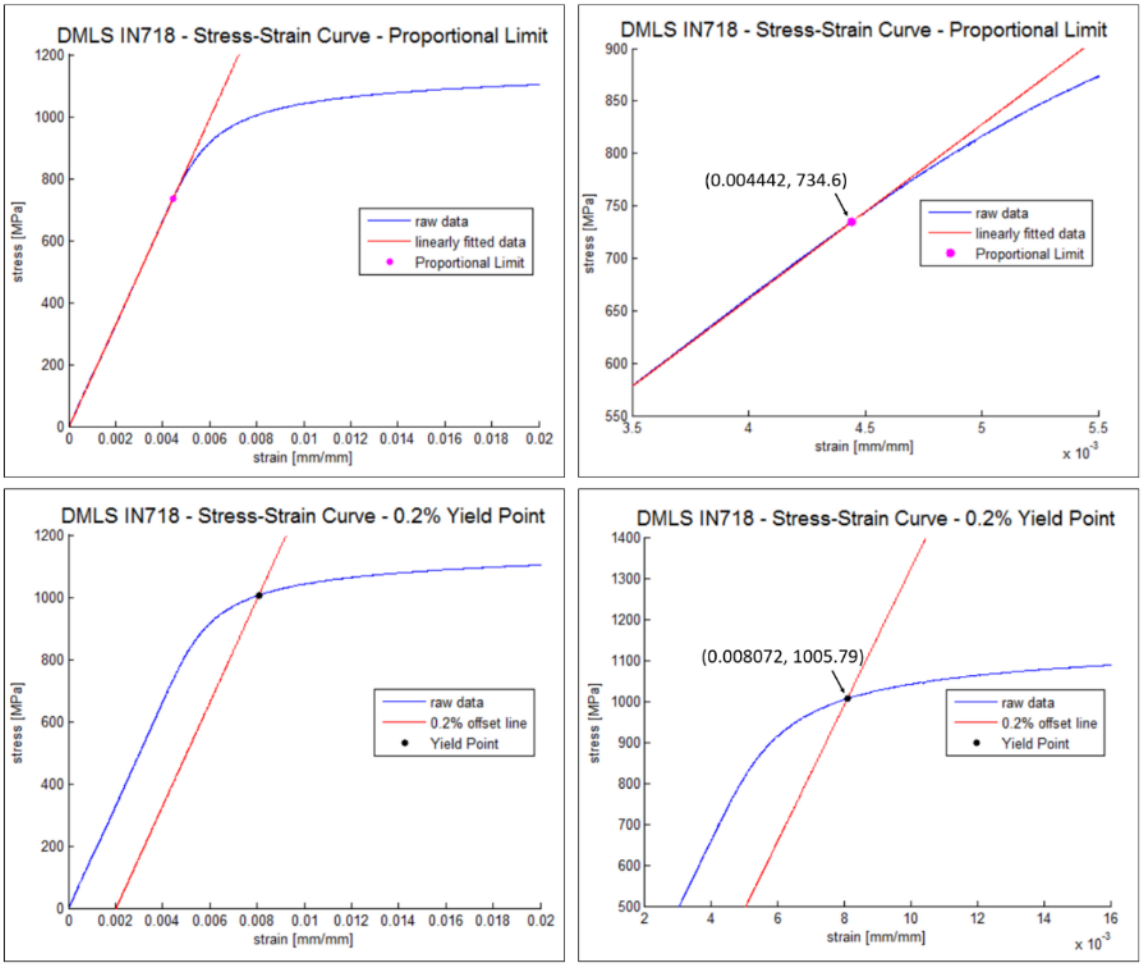

Figure 17 Stress-strain curves showing the proportional limit and 0.2% yield point.

Table 2 Summary of material properties
compared with values from MIL-HDBK-5J, table 6.3.5.0(c)
for IN718 Bar in the L-direction thickness 0.250”-1.000” [21]

Material Property	**Sample Values**	**MIL-HDBK-5J Values**
Elastic Modulus – E	166.45 GPa	202.71 GPa
Proportional limit	734.60 MPa 0.44% strain	- -
Yield Stress – σ_y	1005.77 MPa 0.81% strain	1034.21 MPa -
Failure Stress – σ_f	1196.92 MPa 22.27% strain	1275.53 MPa 12%

4.3 Fatigue properties (from literature)

Fournier and Pineau [22] conducted fully reversed low cycle fatigue tests (R=-1) at room temperature on forged IN718 samples heat treated and aged in accordance with AMS 5662 [19]. They separated the strain amplitude into elastic and plastic strain and, on a log-log plot, determined the relationship between the strain and cycles to failure.

Since the samples in this thesis will be tested under load (stress) control, the results will be plotted on a stress-life curve. Stress controlled test data can be plotted on a log-log plot and modelled with a simple power law known as Basquin’s rule:

$$\frac{\Delta\sigma}{2} = \sigma_f'(2N_f)^b \tag{6}$$

Where $\frac{\Delta\sigma}{2}$ is the stress amplitude, $\sigma_f{}'$ is the fatigue strength (or Basquin's) coefficient, $2N_f$ is the cycles to failure (N_f being the reversals to failure) and b is the fatigue strength (or Basquin's) exponent.

When taking the strain-life approach, the total strain amplitude can be divided into elastic and plastic strain components, with the elastic component given by Basquin's rule and the plastic component given by the Coffin-Manson expression [5].

Since the elastic strain component is directly related to Basquin's rule, Fournier and Pineau's [22] relationship between elastic strain amplitude and cycles to failure can be used to determine the fatigue strength coefficient and exponent. Their results give:

$$\sigma_f{}' = 1600.9\ MPa \text{ and } b = -0.08$$

for forged IN718 (heat treated and aged in accordance with AMS 5662) under fully reversed, stress-controlled, fatigue loading at room temperature. The stress-life curve based on this data is shown by the blue dashed line in Figure 18.

The tests conducted by Fournier and Pineau [22] used fully reversed loading conditions (R=-1). The change in the stress ratio can be accounted for using an equivalent stress $\frac{\Delta\sigma^{eq}}{2}$ in Basquin's rule, that is:

$$\frac{\Delta\sigma^{eq}}{2} = \sigma_f{}'\left(2N_f\right)^b \quad (7)$$

$\frac{\Delta\sigma^{eq}}{2}$ can be calculated using a range of mean stress models [5]. Park *et al.* [23] conducted fatigue testing of IN718 at elevated temperatures and at a range of stress ratios and assessed three mean stress models: the Goodman equation [24], Smith–Watson–Topper

parameter [25] and Walker parameter [26]. Park *et al.* [23] found the Walker parameter, with γ = 0.85 gave the best correlation.

$$\frac{\Delta\sigma^{eq}}{2} = \frac{\Delta\sigma}{2}\left(\frac{2}{1-R}\right)^{1-\gamma} \quad (8)$$

Where $\frac{\Delta\sigma^{eq}}{2}$ is the equivalent stress amplitude, R is the stress ratio (R= 0.1 for the present work), $\frac{\Delta\sigma}{2}$ is the applied stress amplitude at R = 0.1, and γ is the Walker parameter (γ = 0.85 [23]). Figure 18 shows a comparison between the stress-life curve based on Fournier and Pineau [22] at R = -1 and the same curve adjusted via the Walker parameter [26] for a stress ratio of R = 0.1 based on data from Park *et al.* (γ = 0.85 [23]). The application of the Walker parameter adjusts the stress-life curve to 88.7% of the R = -1 Fournier and Pineau results.

The application of the Walker parameter [26] to the Fournier and Pineau [22] stress-life curve, based on the data from Park *et al.* [23] , corrects the curve from an R = -1 to an R = 0.1 curve. This adjustment is applied throughout this thesis.

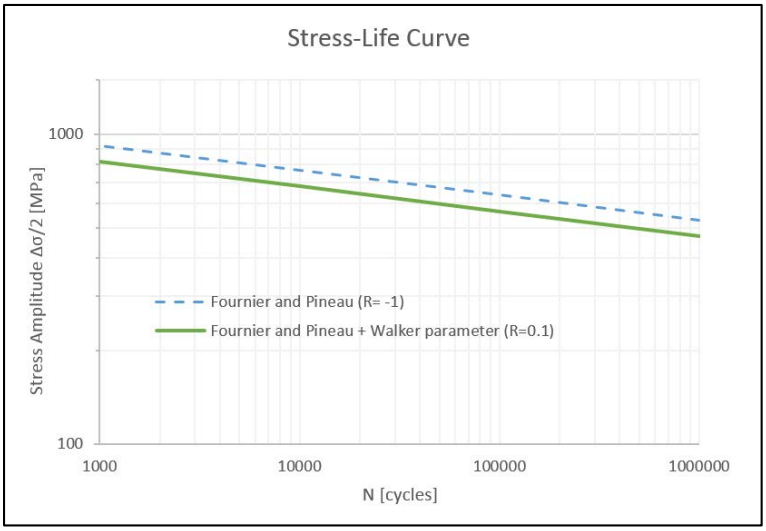

Figure 18 Stress-life curve comparing results from Fournier and Pineau [22] where tests were conducted at R = -1 (at room temperature – blue dashed line) and the same curve adjusted via the Walker parameter [26] for R = 0.1 with $\gamma = 0.85$ [23] (green solid line).

CHAPTER 5. VOID SAMPLES

The first part of this thesis focuses on the behavior of three-dimensional voids, singly and in pairs, under fatigue loading. Though theoretical, elastic solutions have been available for some time [27], the difficulty in sample manufacture has discouraged experimental testing of these 3D defects. Now, however, additive manufacturing allows voids to be reliably and economically placed into the center of test specimens. As added incentive for this research, depending on process and powder parameters, DMLS parts can be susceptible to unintentional void or pore formation [16] though post-processing can minimize or potentially eliminate these defects [15]. Therefore research into the behavior of voids under fatigue loading is worthwhile from both a fundamental material behavior perspective and to better understand the potential behavior of additively manufactured materials.

5.1 Specimen Design and Manufacturing

5.1.1 CAD models and nomenclature

Four void configurations were tested, as shown in Figure 19. Pristine specimens were also manufactured for characterization testing. Throughout this thesis the configurations will be referred to symbolically and descriptively. The cross section of the gauge section is nominally 2 mm x 4 mm.

-  Single void – small: A single 0.5 mm diameter void in the center of the gauge section
-  Single void – large: A single 1.0 mm diameter void in the center of the gauge section.
-  Double void – narrow (spacing): Two 0.5 mm diameter voids in the center of the gauge section separated horizontally by 0.5 mm (edge-to-edge distance).
-  Double void – wide (spacing): Two 0.5 mm diameter voids in the center of the gauge section separated horizontally by 1.0 mm (edge-to-edge distance).

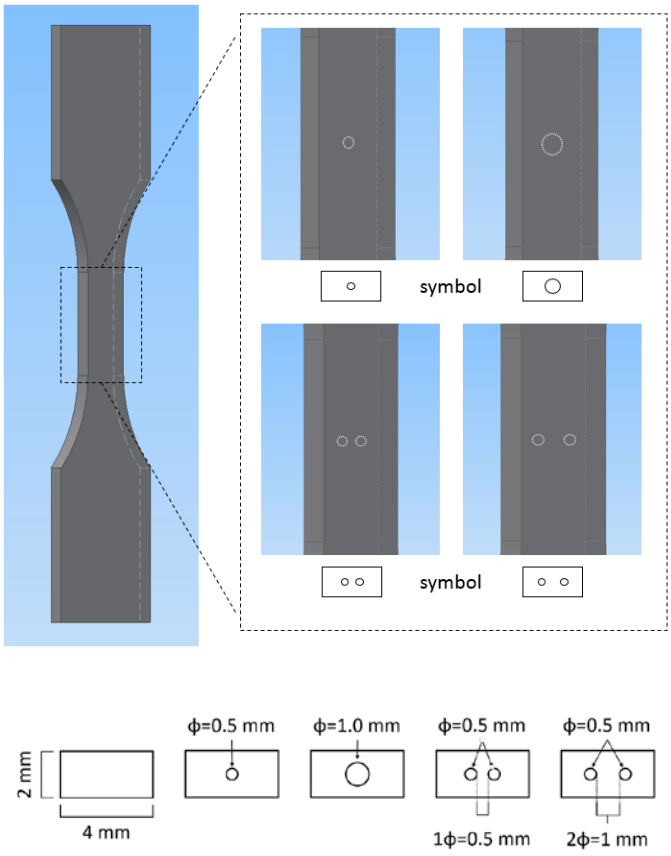

Figure 19 Void specimen configurations, nomenclature and nominal specimen dimensions.

5.1.2 Design and Manufacturing

The void specimens were designed with reference to ASTM E8/E8M − 15a *Standard Test Methods for Tension Testing of Metallic Materials* [28] adjusted to minimize volume, and therefore cost. Figure 20 shows the dimensions of the specimens used to test the void configurations and how these dimensions related to the ASTM standard. The void(s) were placed in the center of the gauge section.

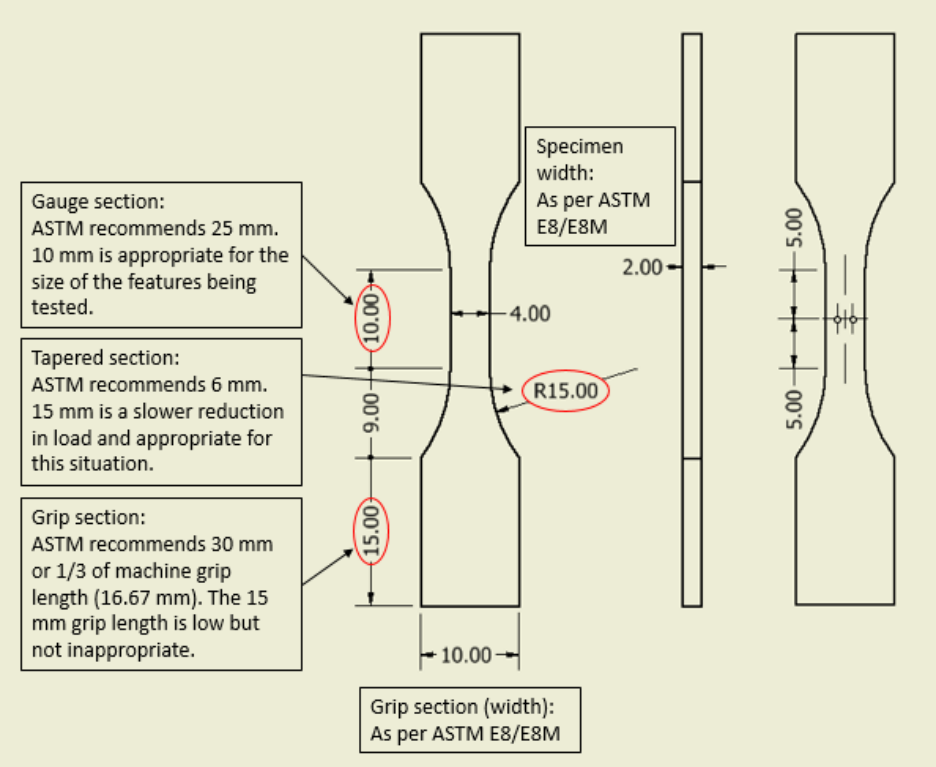

Figure 20 Test specimen for void configurations including a comparison between the designed specimen and ASTM standards. Note: all measurements are in mm.

The specimens were built vertically (in the build direction indicated in Figure 21). This is a typical build direction for tensile testing as it has the poorest mechanical properties [29, 30]. The manufacturer's specifications reflect this and report that, in the as-built

state, tensile testing along this build direction will result in lower yield strength, higher breaking strain and a lower modulus of elasticity [20]. This is likely due to an elongation of the grains in the build direction as noted in [31]. Note that the microtrusses, discussed later in this thesis, are not built in the vertical direction for manufacturing reasons.

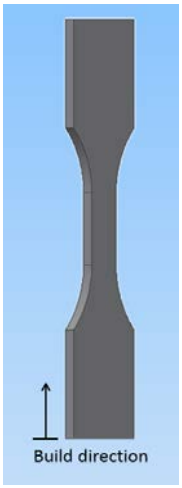

Figure 21 Void specimen build direction.

5.1.3 As-delivered specimens

The specimens were delivered in the as-built condition, polishing of the surface occurred post-delivery to allow the DIC stamp to be applied to the surface and effectively imaged.

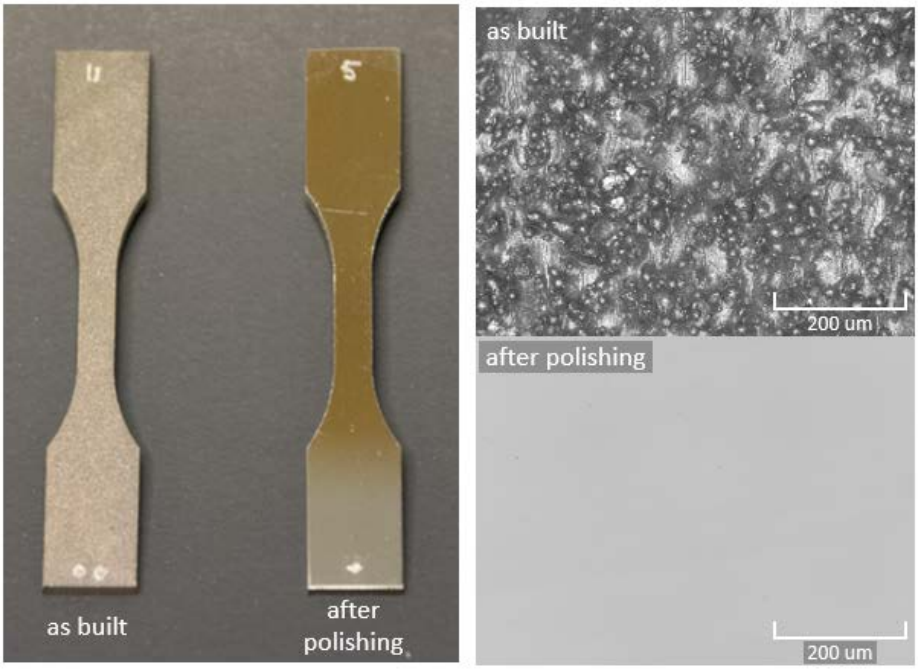

Figure 22 Void specimens: as-built/delivered and after polishing.

Two of the delivered specimens had visible warpage. The warpage was due to large internal stresses during manufacturing and are indicative of the DMLS process. The samples were returned to the manufacturer for rework via mechanical deformation, and, though the warpage was reduced, it was not entirely eliminated. The warped samples were noted during testing, but did not appear to significantly affect the results.

Figure 23 shows another build issue. On several of the specimens the surface appeared to have an uneven build in the grip section. It would appear as if the specimen shifted slightly during the build resulting in a small offset between one build layer and the next. This generally occurred in the grip section and did not appear to affect the results.

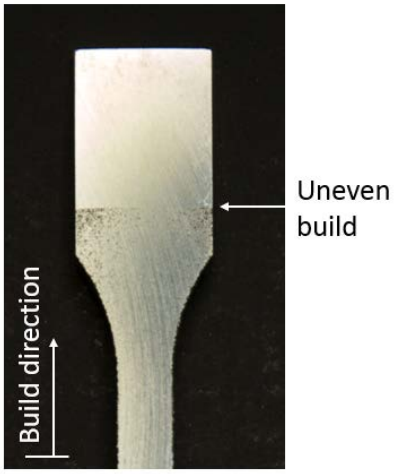

Figure 23 Void specimen showing an uneven build line in the model. It would appear that the model shifted slightly during the build process resulting in an offset between one build layer and the next.

The samples were mixed during heat treatment, and since they all outwardly appear to be the same, non-destructive testing was required to determine their void configurations. The reported void configurations were checked post-testing and found that the double void – wide and double void – narrow specimens had been mixed. Fortunately, the net cross-sections were the same for both configurations, so correct test loads were applied. Once the discrepancy was discovered, the correct K_t values were associated with the corresponding specimens and the analysis carried out accordingly. Though inconvenient, the error had no effect on the testing or results.

5.1.4 Post-delivery processing

Prior to testing, the faces of the specimens were polished with progressively higher grit polishing pads (from 600 grit up to p2500 grit) to remove the surface roughness. The ‘front’ of the sample was then further polished with 0.05 micron alumina then colloidal silica to remove scratches and prepare the surface for the DIC stamp. For the tensile test,

and the first three fatigue tests, the sides of the gauge section were left unpolished. However, this resulted in fatigue cracking initiating from the sides of the gauge section rather than at the void(s). The sides of the remaining samples were polished to p1200 grit in an effort to prevent cracks from initiating from this location. The average dimensions of the as-delivered gauge section and the polished gauge sections are summarized in Table 3.

Table 3 Comparison of as-delivered and polished gauge section dimensions.

Condition	Average gauge section width	Average gauge section thickness	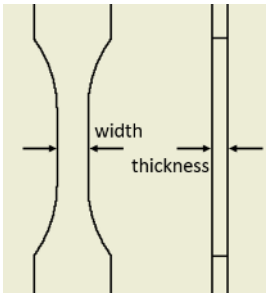
As-delivered	4.132 mm	2.064 mm	
After polishing	3.859 mm	1.836 mm	

5.1.5 Void Sample Microstructure

Post-test, a void sample was polished and etched to reveal the grain structure. The sample was etched using a Modified Kalling's Reagent. Etching time varied significantly (between 10 s and 90 s) depending on how recently the particular surface had been polished.

The procedure was conducted at the locations indicated in Figure 24. Figure 24a shows the grain structure across the build direction; Figure 24b and c show the grain structure parallel to the build direction. The grains on all of the surfaces appear regularly shaped with no elongation in any particular direction. The grains appear larger across the build

direction, though this size difference is not supported by any sort of elongation of the grains parallel to the build direction. The discrepancy is likely due to a failure of the etching process across the build direction. Though this part of the sample (shown in Figure 24a was exposed to the etchant for significantly longer than the other two sides, the etching effect is still very faint. Further work is required to determine if the microstructural differences seen in Figure 24 are reflective of the microstructure or if they are an artifact of the etching process.

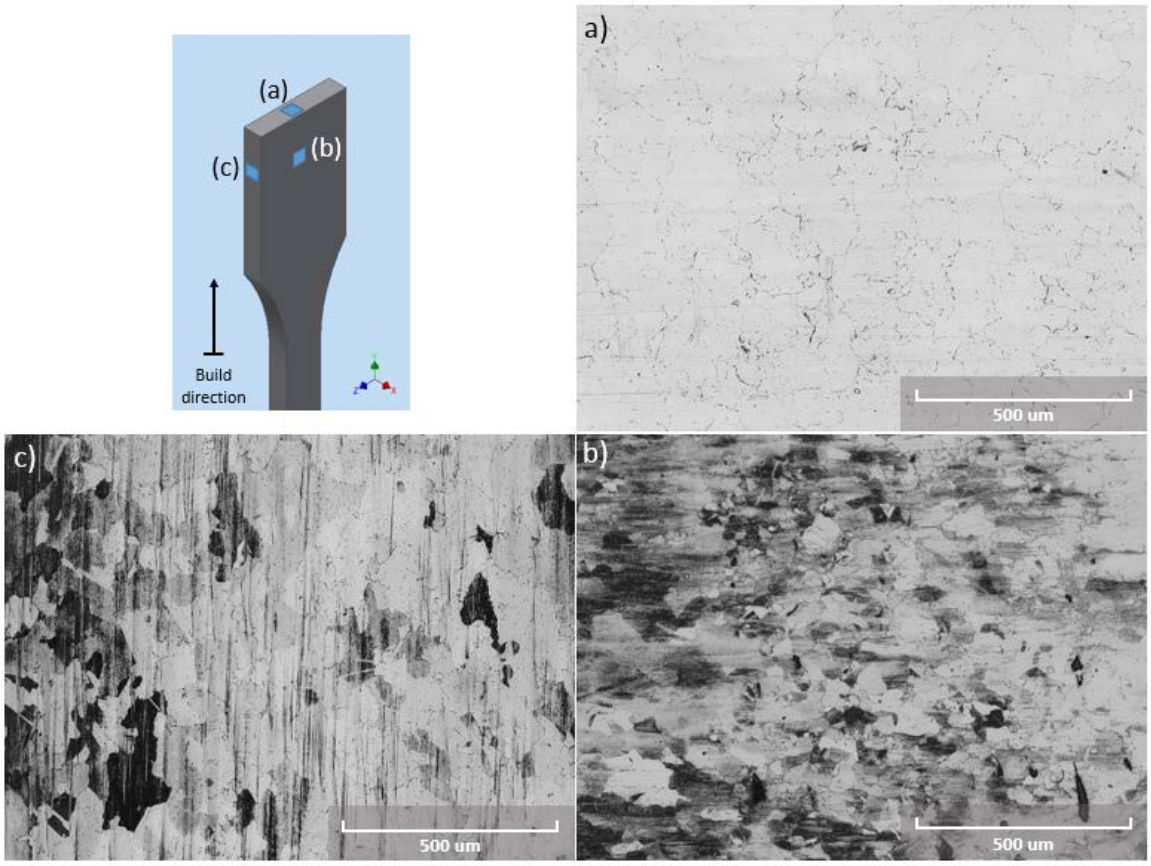

Figure 24 Void sample microstructure.
Note the faint etching of the surface in a, despite being exposed to the etchant longer than b and c. The strong resistance of this surface to the etching process may explain why the grains appear larger in this direction.

An electron back-scatter diffraction (EBSD) image was taken of the surface of one of the void samples to visualize and quantify the grain structure in the area. The result is shown in Figure 25a. The area proportion of each grain size is shown in Figure 25b. A large proportion of the area is taken up by grains with diameters on the order of 65 μm. This result is comparable to the results from the etching shown in Figure 24b.

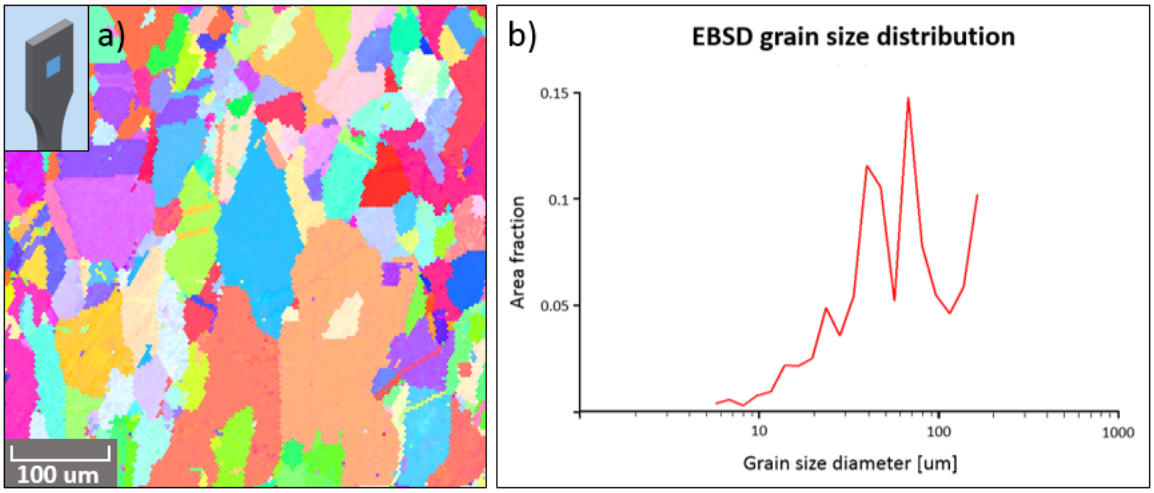

Figure 25 Void sample EBSD results.
a) Grain map of the surface of a void sample, b) Grain size distribution.

5.2 Finite Element Analysis

Finite element (FE) analysis of the different void configurations was conducted to determine the elastic stress concentration factor. The analysis was conducted based on the design dimensions. The results from the FE analysis agreed with the elastic solutions obtained for similar configurations.

5.2.1 Elastic solutions

Pilkey [27] gives the elastic solution for the stress distribution around a cavity in an infinite body in tension based on solutions by Neuber [32]. For a spherical cavity in a

material with a Poisson ratio, υ, of 0.3 (υ of IN 718 = 0.29), chart 4.71 gives a stress concentration, $K_t = 2.05$.

This agrees with the result from chart 4.72, based on work by Sadowsky and Sternberg [33], that looks at filled cavities of elliptical voids with circular cross sections in an infinite body. From this chart, a spherical cavity filled with a material with a modulus of elasticity equal to zero (that is, an empty void) also has a stress concentration of $K_t = 2.05$. From these results, the elastic solution for the stress distribution around a spherical cavity in an infinite body in tension gives $K_t = 2.05$; therefore, we expect that the stress concentrations around the single voids will be approximately 2.05.

5.2.2 FEA Models

Finite element analysis of the void configurations was carried out in ABAQUS (version 6.12-3). Finite element models are computationally expensive; therefore there is significant advantage in reducing the model as much as possible. First, only the gauge section is modelled. Since the specimen is designed to introduce a uniform load into the gauge it is sufficient to model only the gauge section with uniform pressure loading. Second, ABAQUS allows the user to exploit symmetries in the model. Exploiting all of the available symmetries allows the entire void region to be modelled with a $1/8^{th}$ model as shown in Figure 26.

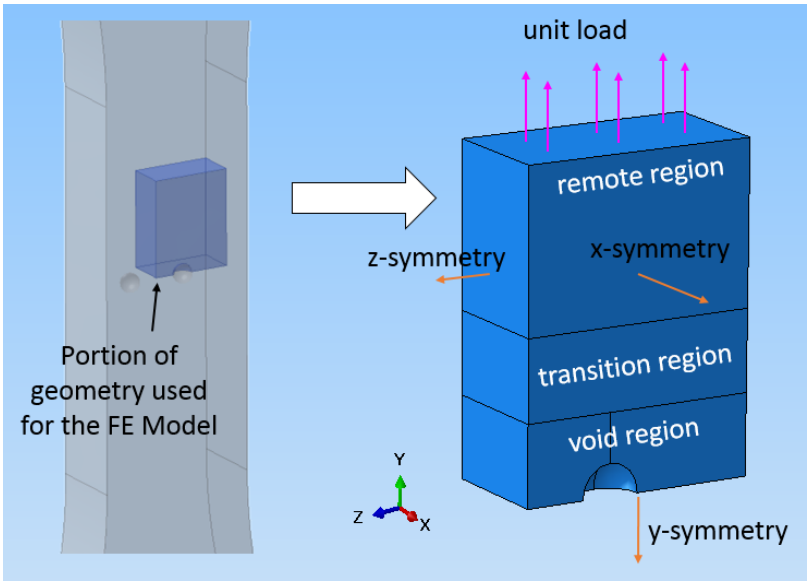

Figure 26 1/8th Finite element model compared to the full model.

Reducing the number of elements and nodes in the model can also reduce the computational cost of the model; this is primarily controlled by the seed size (larger seed = fewer elements). The aim of the model is to examine the stress concentration around the void; therefore the seed size in the void region is continuously reduced as part of the convergence analysis (minimum seed size in the void region for all of the models was 0.0075). Further away from the void, the element size is less critical; thus, to reduce the number of elements, the seed size in the remote region is kept constant at 0.08 mm. The transition region is used to provide a smooth gradient from the small seed size in the void region to the larger seed size in the remote region. This effectively produces very small elements in the void region and larger elements in the remote region, which is more computationally efficient than using uniformly small elements.

The models were meshed with 8-node linear brick elements. A convergence analysis was conducted with the void region seed size decreasing from 0.08 to 0.0075. The average

number of nodes increased from 25.5 thousand (with 22.6 thousand elements) to 4.36 million (with 4.28 million elements). The FE analysis output for the model in Figure 26 is presented Figure 27 and is representative of the output for the other void samples.

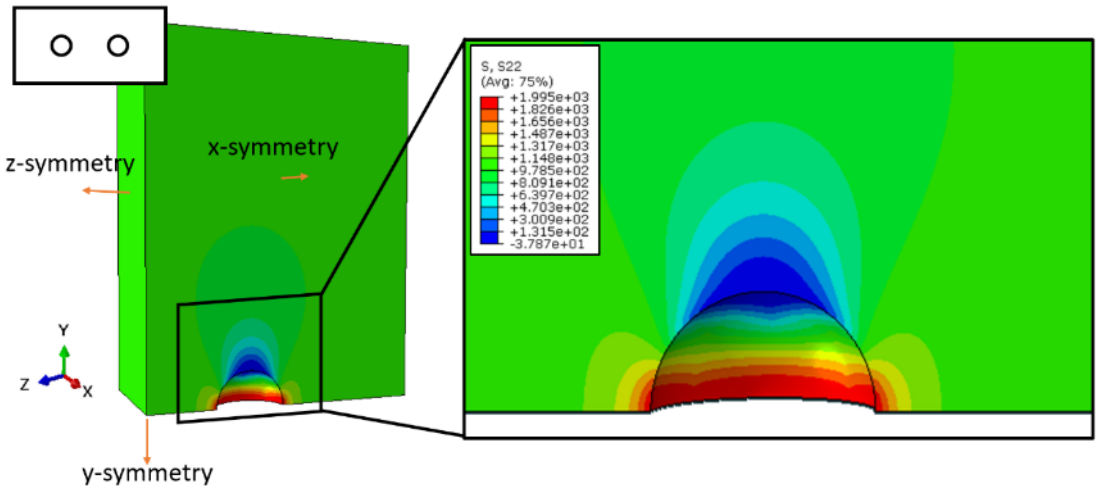

Figure 27 Finite element results for the double void – wide sample shown in Figure 26 with 1/8th symmetry.

5.2.3 Summary of stress concentrations

The FE analysis was carried out for each of the void configurations. The cross-sectional area of each specimen was measured prior to testing and used to determine the K_t (net), where:

$$K_t(net) = K_t(gross) \times \frac{reduced\ cross-section}{gross\ cross-section} \quad (9)$$

The gross and net stress concentration results for the void samples are summarized in Table 4.

Table 4 Summary of stress concentrations.
K_t (gross) was determined from FE analysis, K_t (net) was then calculated using the post-polished cross-section of each sample removing the nominal void cross-sectional area.

Configuration	K_t (gross)	K_t (net)	
Single void - small	2.05	1.990	1.997
Single void - large	2.17	1.925	1.943
Double void - narrow	2.04	1.920	1.918
Double void - wide	2.03	1.917	1.918

5.3 Fatigue test and results

Fatigue testing was conducted under load control with guidance provided by ASTM E466 [9].

5.3.1 Fatigue test parameters

The fatigue test parameters are summarized in Table 5.

Table 5 Void specimen fatigue test parameters.

Parameter	**Value**
Frequency	0.667 Hz
Stress ratio, R	0.1
Wave shape	Sinusoidal

The stress ratio of R = 0.1 was chosen to align with the stress ratio used for the microtruss testing[2]. The test frequency was determined after evaluating a range of frequencies using the average Mean Square Error (MSE) between the command load and the measured load to quantify how accurately the MTS could load the specimen at a given frequency. Figure 28 shows the results of the evaluation. The error reduces as the test frequency is reduced. At approximately 0.7 Hz, the slope of this reduction changes, and reducing the frequency has less of an effect on the accuracy of the load control. At this point, the error in the load control is low enough for testing, therefore a test frequency of 0.667 Hz was chosen.

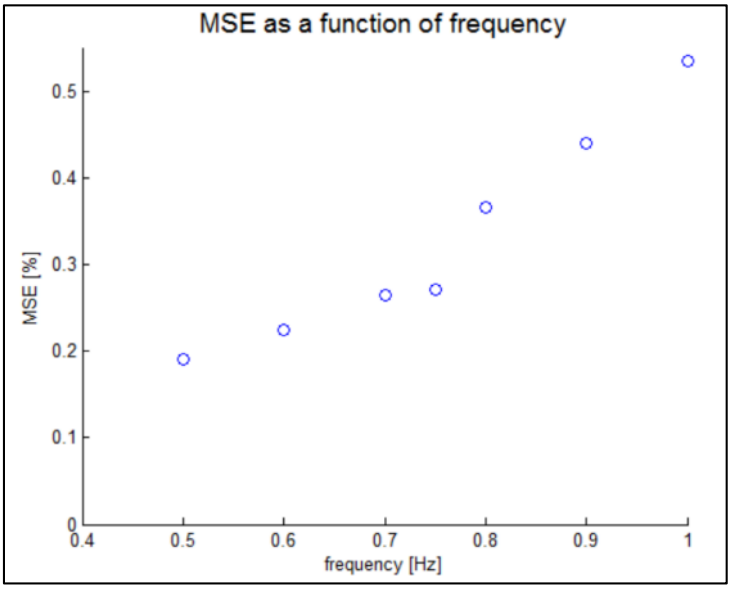

Figure 28 Test frequency evaluation.
This plot shows the average Mean Square Error (MSE) between the command load and the measured load over a range of test frequencies.

[2] R = 0.1 was chosen to ensure that the microtruss was not compressed during testing as this may have led to buckling of the ligaments.

5.3.2 Stress range

The aim was to apply a maximum stress of 90% of σ_{yield} with a stress ratio of R = 0.1; for the pristine specimen this was equal to a gross (and net) stress of:

- Maximum stress σ_{max} = 905.2 MPa
- Stress amplitude $\Delta\sigma/2$ = 407.3 MPa

The original intent was to apply the maximum stress of 0.9 σ_{yield} at the most highly stressed point in the void specimen. This would require that both the reduction in cross-section and stress concentration be taken into account. Therefore, for a single void – large specimen, the maximum stress and stress amplitude are as shown in Table 6.

Table 6 Maximum stress and stress amplitude for a single void – large specimen when taking into account net area reduction and stress concentration to determine the fatigue loads.

	Stress at point of highest stress concentration	Gross (remote) stress
σ_{max}	905.2 MPa	417.1 MPa
$\Delta\sigma/2$	407.3 MPa	187.7 MPa

Testing of the single void – large specimen at this load saw the fatigue life increase to the runout life of 400,000 cycles. For the remaining tests, the stress calculation was adjusted to account only for the decrease in net cross-section loss due to the voids. Therefore, the gross stresses were set so that at the void cross-section, the net stresses were:

- Maximum stress σ_{max} = 905.2 MPa
- Stress amplitude $\Delta\sigma/2$ = 407.3 MPa

Once the gross stress was determined, the force required was calculated based on the dimensions of the test specimen. The force values were then loaded into the test program and used to control the fatigue testing.

5.3.3 Digital Image Correlation intervals

Images of the specimen surface were taken at logarithmically regular intervals during testing. That is, at the maximum loading of cycle 1, 10, 100, 1000 and 10000. Images were taken more often if the compliance of the specimen began to change (indicating imminent failure) or if the image captured an interesting feature. Correlation of the images was conducted in Vic-2D with a subset size of 25 pixels and a step size of 1 pixel.

5.3.4 Fatigue test failures and results

In all, nine samples were tested in fatigue. The location of their failures is shown in Figure 29. The dashed line indicates the location of the voids within the sample (except for sample 2 which does not contain voids) of the nine samples:

- Four failed at the voids due to cracks that initiated from the void (samples 4, 6, 8 and 9 – outlined in green)
- One sample was tested at a significantly lower load and was a run-out (sample 7 – outlined with a green dash). This was later tested at a higher load and failed at the voids due to cracks that initiated from the void.
- Four failed due to cracks initiating from surface defects on the sides of the specimens (samples 2 (no voids), 5, 10 and 11 – outlined in red).

The location and likely cause of failure was determined via optical fracture surface analysis and later confirmed via SEM imaging of some of the fracture surfaces.

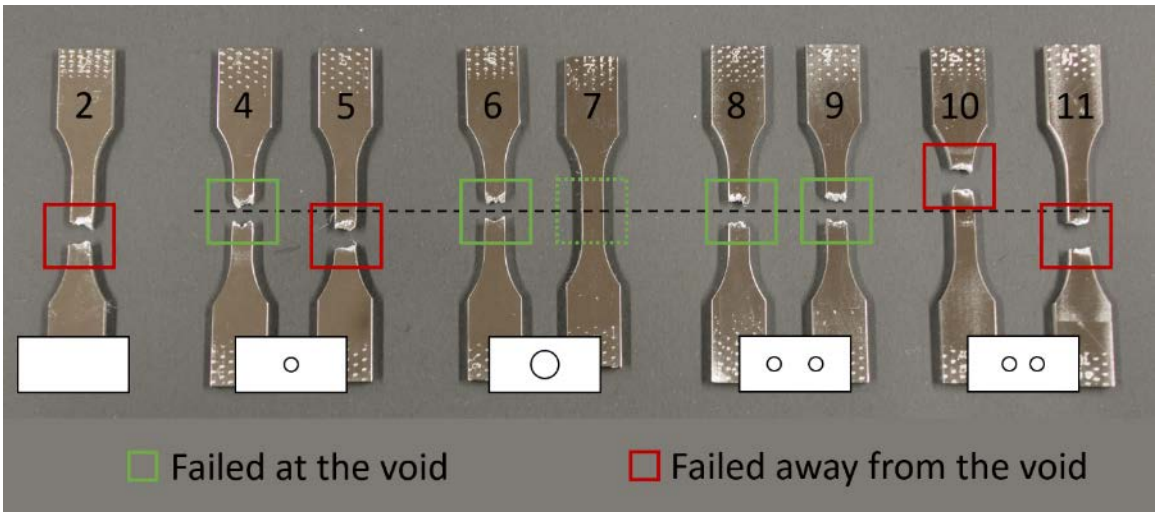

Figure 29 Location of fatigue failures in the pristine and void specimens. The dashed line indicates the location of the voids within the specimen. Samples 1 and 3 were pristine samples used for material characterization.

Testing was initially conducted with the extensometer measuring the strain in the sample and without polishing the sides of the sample as the stress concentration, due to the surface roughness was not expected to exceed the stress concentration of the voids. After the first three samples failed at locations other than the void surfaces, the sides were polished to reduce the likelihood that cracks would initiate from these locations. Then, after one of each void configuration had been tested, the extensometer was removed to ensure that cracking would not initiate at the point where the extensometer was in contact with the specimen. Fracture surface analysis of the failures found that the extensometer did not initiate cracking.

Figure 30 shows the results for all the void specimens (including the pristine specimen but excluding the run-out). There does not appear to be a significant difference between

the samples that failed at the voids and the samples that failed away from the void. The red dashed line is based on the samples that failed away from the void.

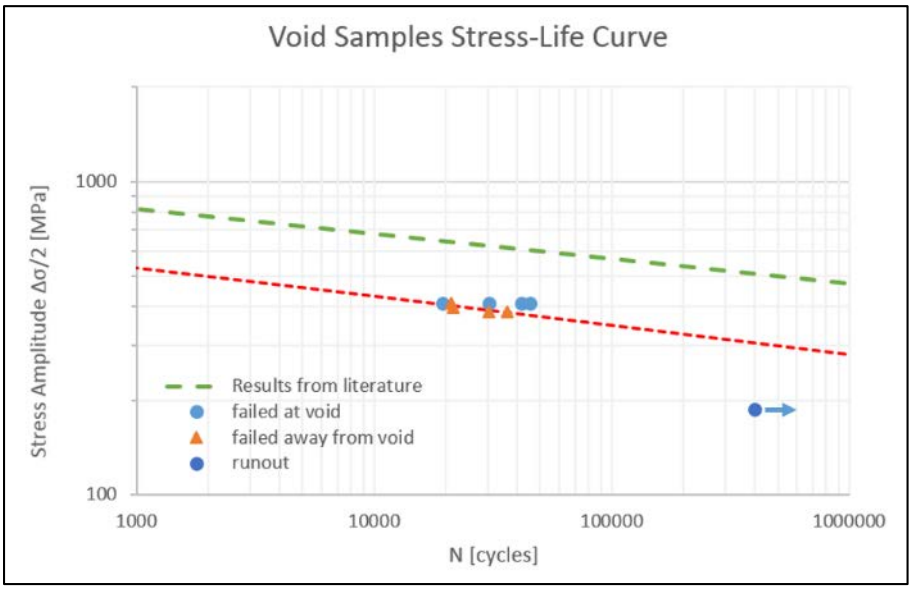

Figure 30 Stress amplitude vs life curve for the void samples.
Stress-life curve from Fournier and Pineau [22] (tests conducted at room temperature and adjusted to R=0.1 – green dashed line) compared with the void samples. The red-dashed line is the power-law fitted line for the samples that failed way from the void (R = 0.1).

Table 7 Fatigue test results for samples that failed at the void.
Note that the q values presented are not directly comparable as they are each determined at different values of N (no. cycles). * Values based on stress-life curve from Fournier and Pineau [22] (tests conducted at room temperature and adjusted to R=0.1).

Sample	σ_{max} @ failure surface [MPa]	N [no. cycles]	$\Delta\sigma/2$ [MPa]	Smooth fatigue strength* [MPa]	Kf	Kt	q
4 	905.2	30401	407.34	621.91	1.527	1.990	0.532
6 	905.2	19359	407.34	644.77	1.583	1.925	0.630
8 	905.2	41859	407.34	606.20	1.488	1.920	0.531
9 	905.2	45283	407.34	602.39	1.479	1.918	0.522

Table 8 Fatigue test results for samples that failed away from the void surface.
* In these samples, the crack initiated at defects that were inherent in the material. The stress concentration due to these particular defects is unknown.

Sample	σ_{max} @ failure surface [MPa]	N [no. cycles]	$\Delta\sigma/2$ [MPa]	Smooth fatigue strength [MPa]	Kf	Kt
2	905.2	21070	407.34	640.42	1.572	Unknown*
5	881.8	21465	396.80	639.47	1.612	
10	854.8	36448	384.66	612.95	1.593	
11	855.5	30434	384.95	621.85	1.615	

5.4 Outcomes and analysis

5.4.1 Fracture Surface Analysis

Figure 31 shows a Scanning Electron Microscope (SEM) image of a typical single void fracture surface. The SEM image shows the cracks initiating from the circumference of the void and growing radially, the majority of the cracking occurs in region around the void. Analysis of some of the other single void fracture surfaces shows evidence of cracks initiating from the edges of the specimen, though this is not evident in fracture surface shown in Figure 31.

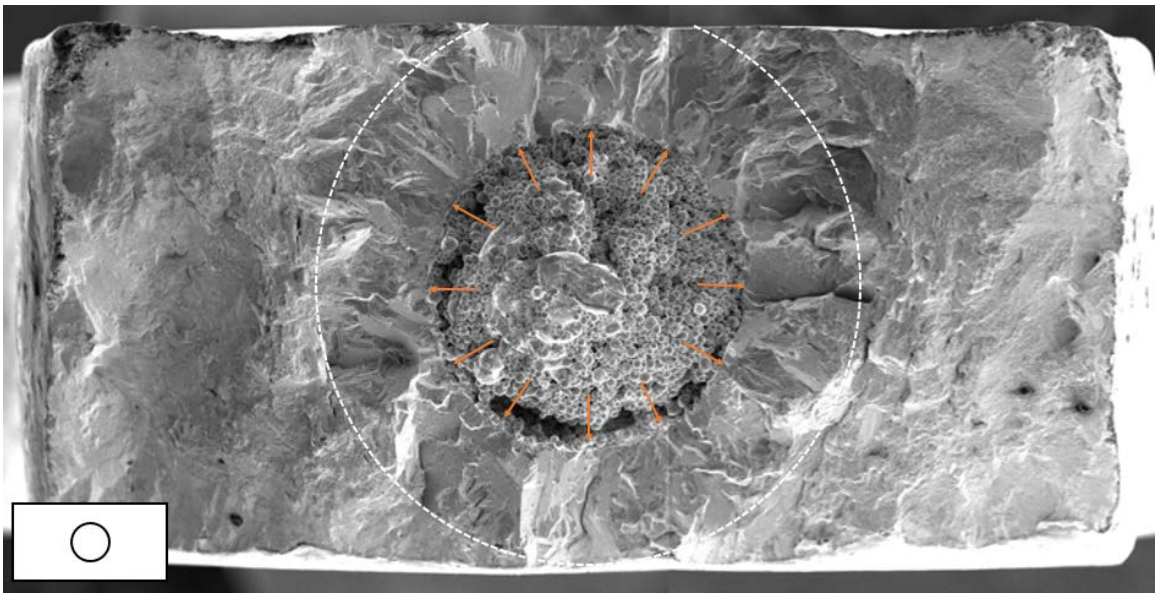

Figure 31 SEM image of a typical single void fracture surface.
The cracking initiates from multiple locations on the edge of the void and grows radially.

Figure 32 shows a sketch of the hypothesized crack growth in a double void sample. The interaction between the voids should increase the stress concentration at the void surface closest to the other void. This increases the likelihood that cracking initiates at this surface. Once the crack has initiated, the cracks continue to grow towards each other until

they coalesce, once they do, the two voids and the crack act as a single elliptical shaped crack.

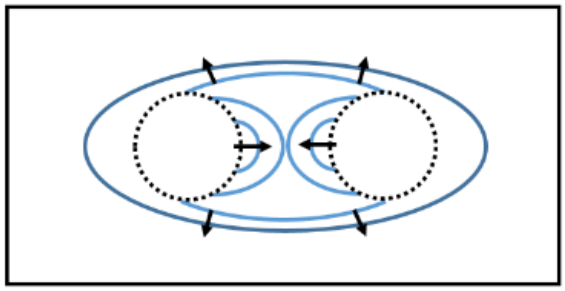

Figure 32 Expected crack growth for double void specimens.

A fracture surface analysis of a failed double void sample was carried out to confirm the crack growth behavior. The results are shown in Figure 33.

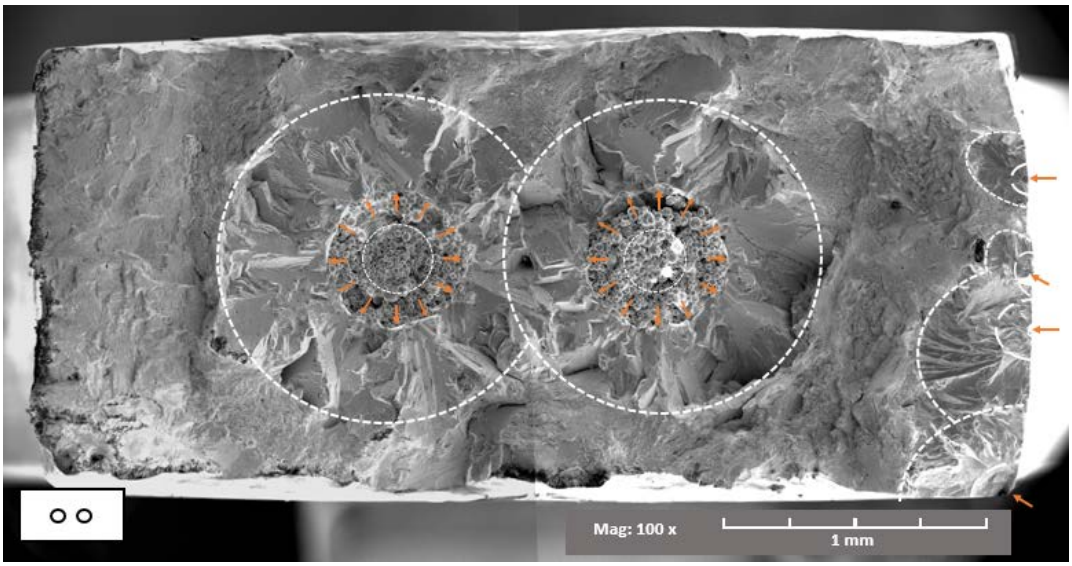

Figure 33 SEM image of a typical double void fracture surface.
Crack initiation sites are indicated by the orange arrows. For the cracks initiating from the right side of the specimen, early crack growth is indicated by the large dashes; final crack fronts are indicated by the smaller dashed lines.

The fracture surface shows fatigue cracks radiating from each of the voids. The cracks initiate at multiple sites around the circumference of the void and grow outwards. The

cracks continue to grow independently until they coalesce at the center. However, unlike the hypothesized crack growth shown in Figure 32, the cracks predominantly grow radially and coalescence occurs incidentally as part of the radial crack growth. This supports the FE analysis of the double void – wide specimen shown in Figure 34 (which is the same configuration shown in Figure 26 and Figure 27). Plotting the stress concentration around the circumference of the void shows that there is little variation between the stress concentration on the side closest to the other void (left side of the plot) and the side furthest from the other void (right side of the plot).

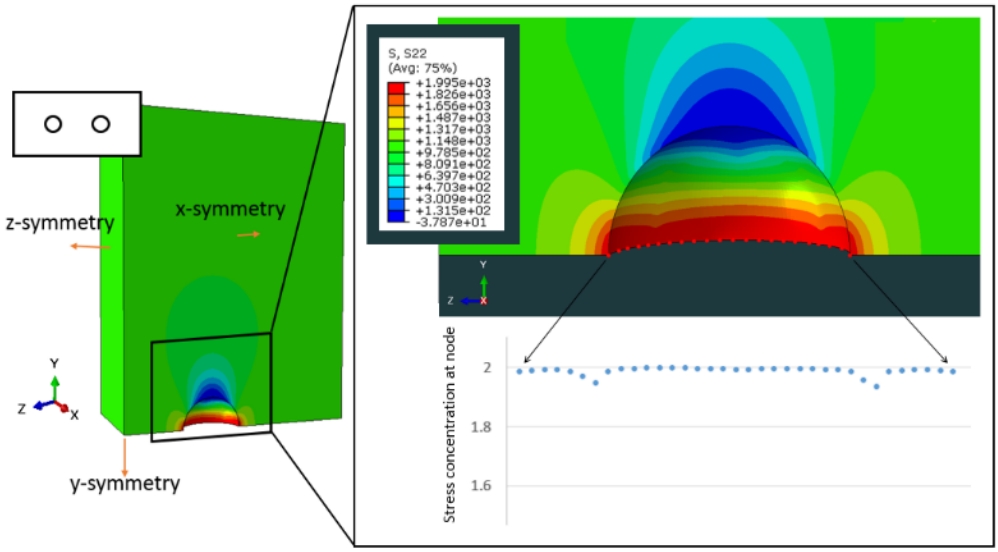

Figure 34 Finite element analysis results for the double void – wide specimen shown in Figure 26 and Figure 27 showing the stress concentration around the circumference of the void. Note that the stress concentration at the side closest to the other void (left side of the plot) is no greater than the stress concentration on the side away from the void (right side of the plot).

The fracture surface also shows several cracks initiating and growing from the corner and side of the specimen. The growth and coalescence of these cracks is indicated in Figure 33. These cracks suggest that the stress concentration due to the surface defects were of a

similar magnitude to the stress concentration due to the voids. Figure 35 shows a close-up view of two of these defects.

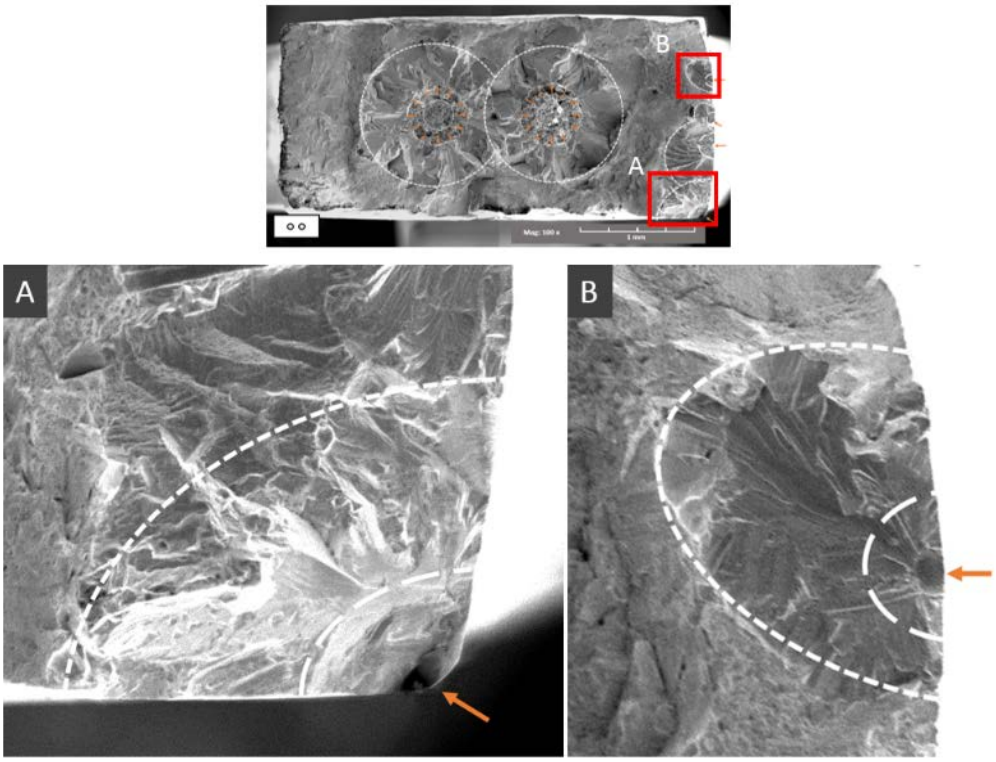

Figure 35 Surface defects/stress concentrators
that initiated the cracking from the side seen in Figure 33.

Figure 36 shows the fracture surface of a sample that failed away from the voids. Cracking has initiated on the right-hand edge of the surface and grown in and downwards. Some cracking has also initiated at the center of the top edge of the surface. What is interesting about this surface is the naturally occurring voids and pores highlighted in the lower portion the figure. The largest is approximately 20 μm across, however the fracture surface does not indicate that cracking has initiated at any of these voids or pores. These naturally occurring voids and pores can also be seen on fracture surfaces where failure occurred at the voids with a similar lack of crack initiation. This

suggests that the small voids and pores within the sample, which would likely have been removed if the samples had under gone HIP post-processing [15], did not have a significant effect on the fatigue life of the samples.

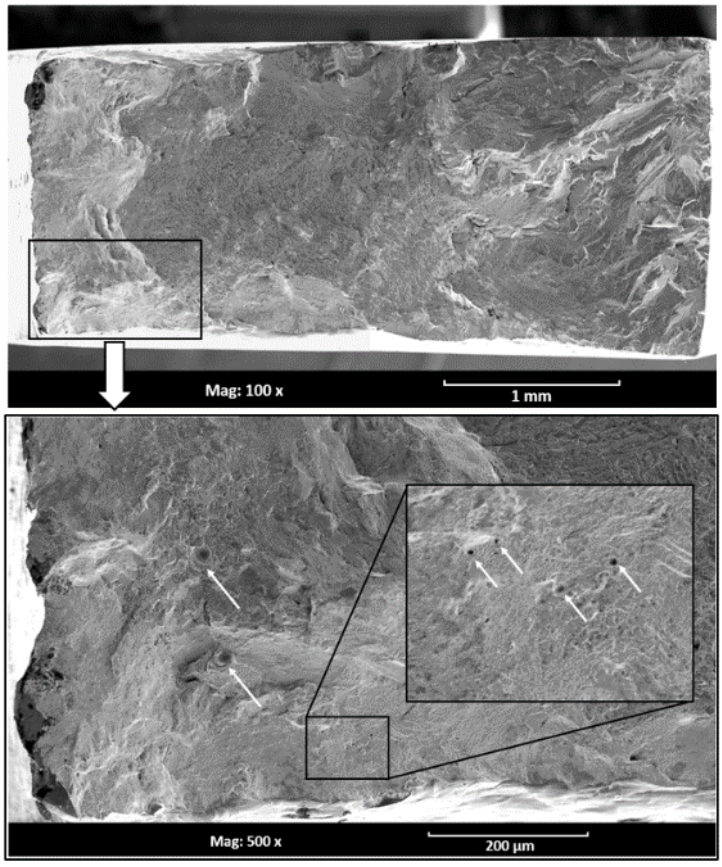

Figure 36 Sample that failed away from the void surface highlighting naturally occurring voids in the sample. Note that cracking does not appear to have initiated at any of these voids (the cracking has initiated at the right-hand edge of the sample).

5.4.2 Void structure

The DMLS process does not allow for the powder to be removed from the void during manufacturing. The earlier FE and elastic analyses assumed that any powder remaining in the voids would be loose and have no effect on the behavior of the void. In other words, the loose powder in the void would have an elastic modulus approximately equal to 0. In

order to test this assumption the voids were examined post-failure. Figure 37 shows the SEM images of the voids in the top and bottom failure surface. If the powder seen in the voids were loose, the images would show empty hemispheres. Since this powder has not come loose, it must be partially sintered in the void. That is, there has been sufficient heating applied for the powder particles to agglomerate and attach to the sides of the void.

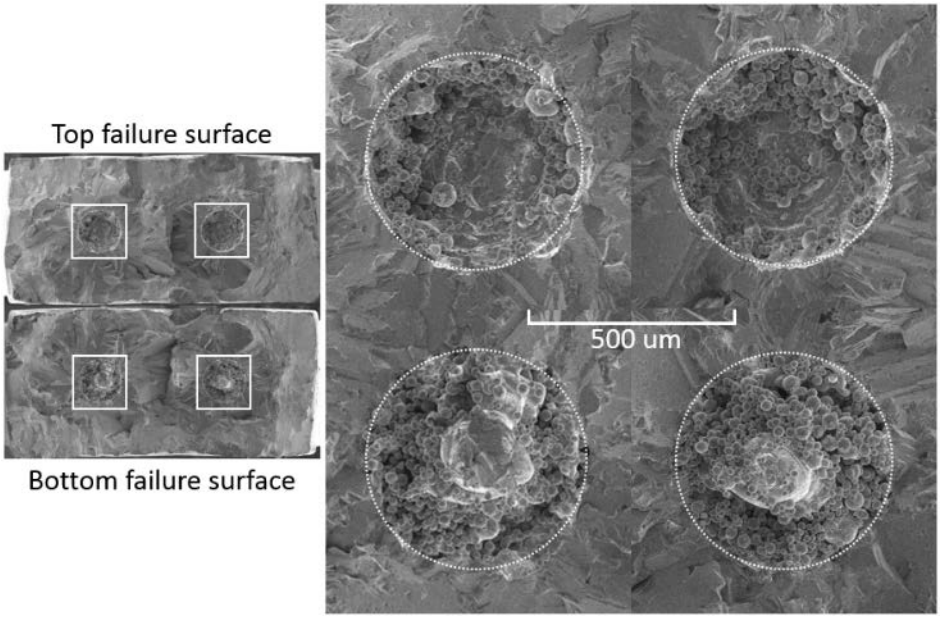

Figure 37 SEM images of the voids in a double void – narrow sample comparing the top surface to the bottom surface. Note that the bottom voids are not empty; partially sintered powder remains.

The voids shown in Figure 37 are not unique, partially sintered powder was found in all of the samples that broke at the void surface. In effect, this means that elastic modulus of the voids (E') was greater than 0, though there is no way for this value to be quantitatively evaluated from the data collected. Since the powder is only partially sintered, it is traction free on half of the surface area; therefore it is not expected to carry

a large load. It is more likely that the partially sintered powder would geometrically restrict the plastic deformation/elongation of the void.

Pilkey [27], chart 4.72, gives elastic stress concentration factors for filled voids at certain ratios of E'/E (where E is the elastic modulus of the bulk material). An E'/E = 0 gives the stress concentration factor solution for an empty void presented in Section 5.2.1; an E' > 0 decreases the stress concentration factor. Assuming E'= 0 gives a conservative estimate of the stress concentration factor; therefore, the K_t of the partially filled voids will be less than the estimated K_t = 2.05 (Section 5.2.1). However, the overestimation of K_t results in an underestimation of the notch sensitivity factor, that is, the q value determined based on an E' = 0, underrepresents the true notch sensitivity of the material.

The most significant effect of the partially sintered powder is the effect that this is has on the surface quality of the voids. Figure 38 shows the fracture surface around the void and highlights several crack initiation sites. High magnification images of these sites show that the region around the partially sintered powder particle can be a sharp stress concentration resulting in crack initiation in the area.

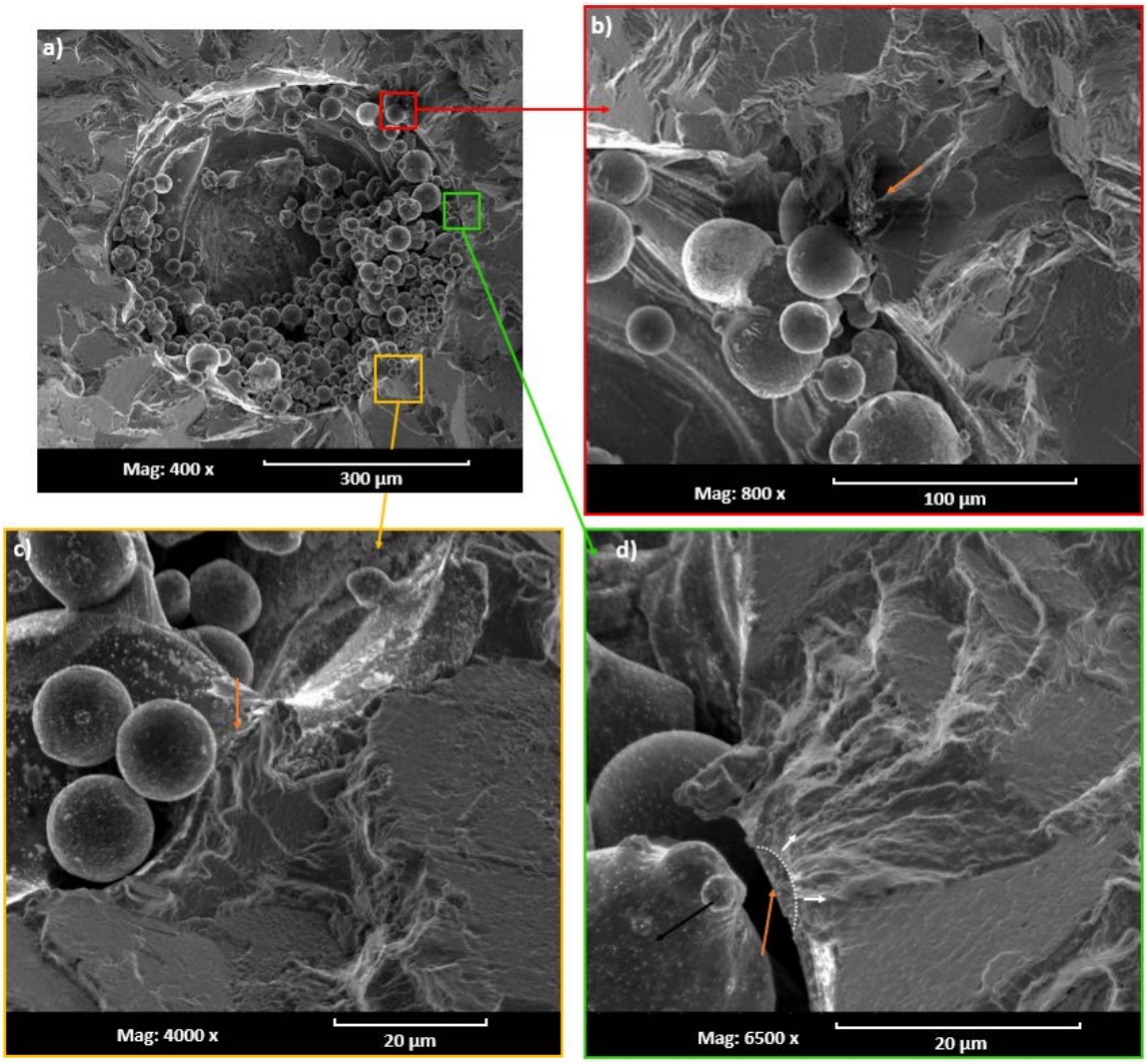

Figure 38 SEM images of the region around the void.
b), c) and d) show crack initiation sites around the edge of the void. Note the partial sintering of the powder at these locations. In particular, d) shows a location where a partially sintered powder particle has detached from the edge of the void leaving a crack initiation site.

5.4.3 Failure Analysis – Single Void – Large sample

Figure 39 shows the stress-life curve for the void samples and highlights the failure of the single void – large sample. This sample failed at the lowest number of cycles.

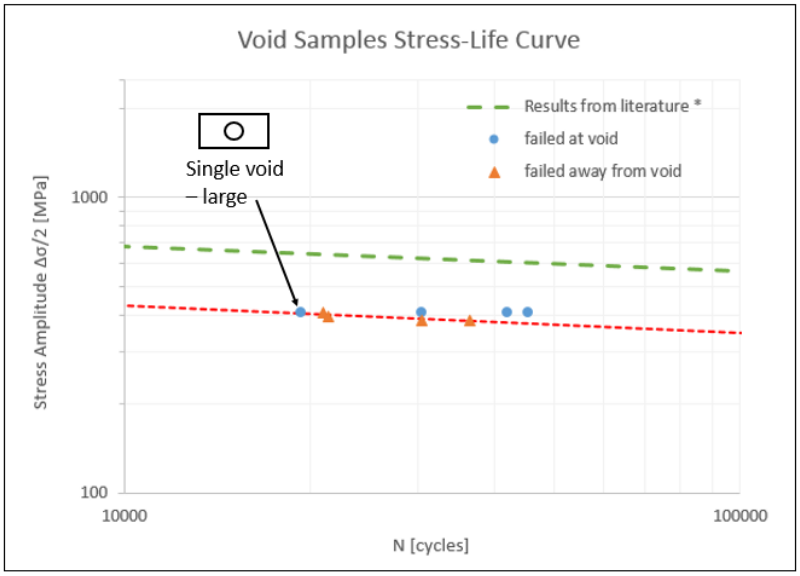

Figure 39 Stress amplitude vs life curve
highlighting the failure of the single void – large sample. * Stress-life curve from Fournier and Pineau [22] (tests conducted at room temperature and adjusted to R=0.1).

Finite Element Analysis determined that the single void – large configuration had the largest gross stress concentration ($K_{t\text{-}gross}$ = 2.17), however, accounting for the net cross-section loss reduces the stress concentration to $K_{t\text{-}net}$ = 1.93, on par with the net stress concentration in the double void sample configurations that failed much later.

Figure 40 compares the fracture surfaces of the single void – small and single void – large samples and shows the significant difference in size and geometry between the samples.

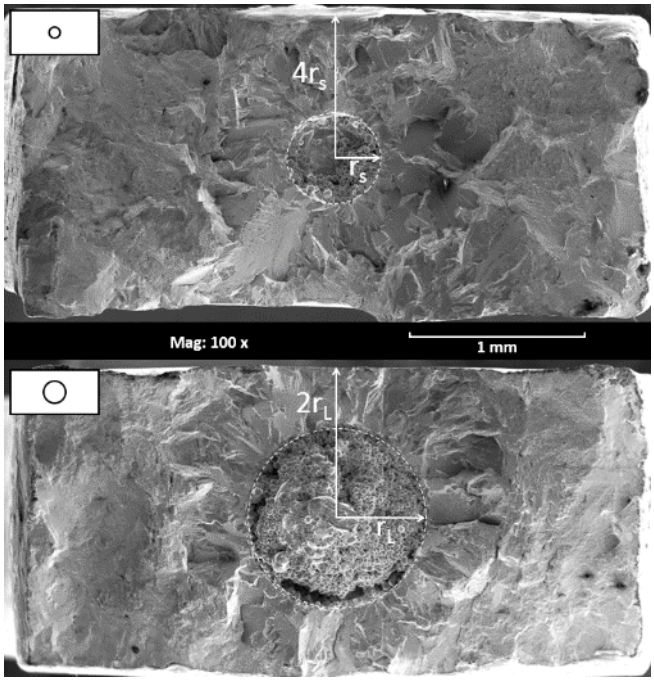

Figure 40 Fracture surface comparison
between the single void – small and single void – large samples.
The large void is a significantly larger initial crack.

For the large void - the distance between the center of the void and the surface of the sample is $2r_L$, where r_L is the radius of the large void, as annotated in the figure. This distance is great enough that the free surface should have practically no effect on the stress intensity factor of the void [34]. It is worth noting that as the crack grows around the void, the distance between the center of the crack and the edge, as a function of the crack radius decreases (due to the increase in the crack radius), which increases the stress intensity factor, K.

The voids are a flaw within the sample that, given the applied loads, will quickly initiate radial cracking. Once this cracking has initiated, the void and radial crack can be considered to behave like a 'penny-shaped' crack in the sample. The cycles to failure, N_f, can be estimated by the integration of the Paris Law:

$$N_f = \int_{a_0}^{a_f} \frac{da}{C(\Delta K)^m} \quad (10)$$

Where a_0 is the initial crack size, a_f is the final crack size (in this case, the crack length at fracture), C and m are constants determined from the linear portion of the da/dn – ΔK curve and ΔK is the cyclic stress intensity factor. Apart from the radius of the void, the samples are identical, therefore, a_f, the final crack size, and C and m from the da/dn – ΔK curve are the same for both samples. Additionally, since the geometry of the voids are the same, ΔK, the cyclic stress intensity factor, is the same for both samples[3]. The only difference is the initial flaw size; the single void – large sample has a larger initial flaw size than the single void – small sample reducing the number of cycles to failure.

The single void – large sample failed at a lower number of cycles than the other samples. This early failure is unlikely to be due to the local stress concentration factor or a function of the large void's proximity to a free surface, instead, it is likely due to the larger void acting as a larger initial crack size.

5.4.4 Failure Analysis – near simultaneous failure (double void – narrow sample)

Figure 41 shows one of the double void – narrow specimens that failed away from the void surface. Interestingly, the classical necking in the region of the voids indicates local instability based on the accumulation of significant localized plastic strain; signifying imminent failure in the void region.

---

[3] Recall that, for the geometry of the single void – large sample, the proximity of the surface has little effect on the stress intensity factor of the large void [31].

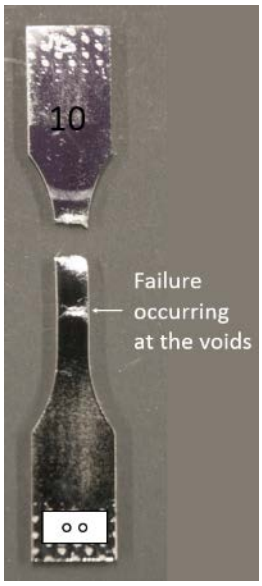

Figure 41 Double void – narrow sample that failed at the top of the gauge section. Note that the sample has begun to fail at the necked section.

The observation that the failures were occurring nearly simultaneously suggests that the stress concentration was similar at both locations; if either value had been significantly larger than the other, we would expect the location with the larger stress concentration value to fail much earlier (given similar local microstructures). Note that the failure location has an additional 5% cross-sectional area compared to the void region, therefore the K_t at the failure location is likely to be slightly higher than the K_t due to the voids. The difference in cross-sectional area is small and does not change the conclusion that the stress concentrations are likely similar at both locations. Higher magnification images of some of the crack initiation sites are shown in Figure 43.

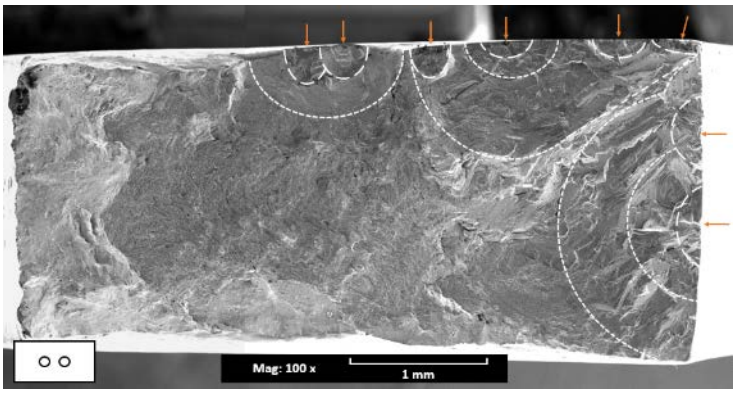

Figure 42 Fracture surface of the double void-narrow specimen shown in Figure 41.

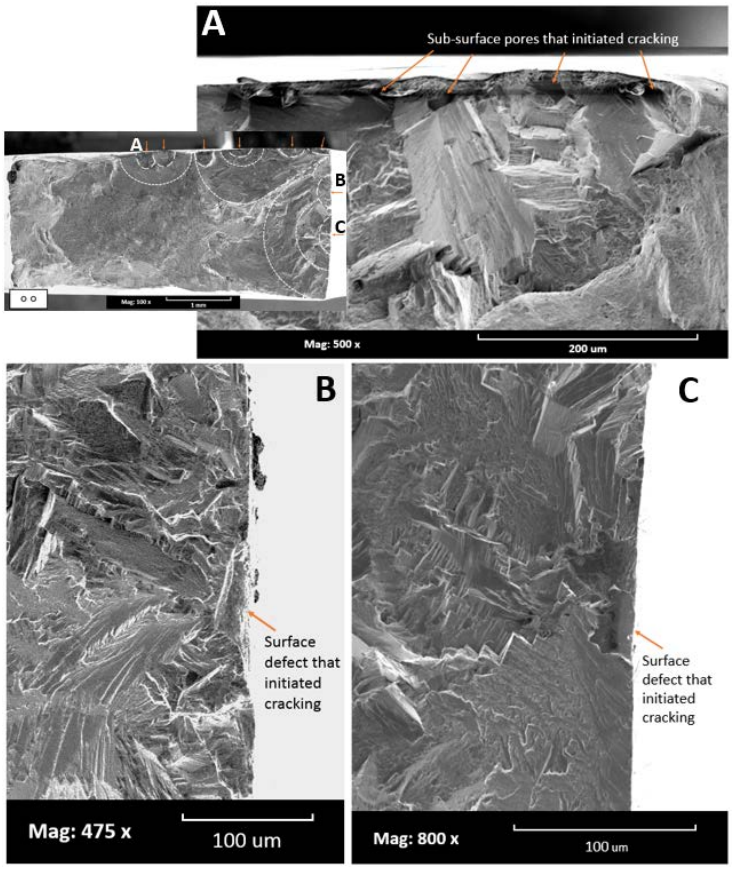

Figure 43 Surface defects that initiated cracking in the sample shown in Figure 42.

5.4.5 Failure Analysis – overall

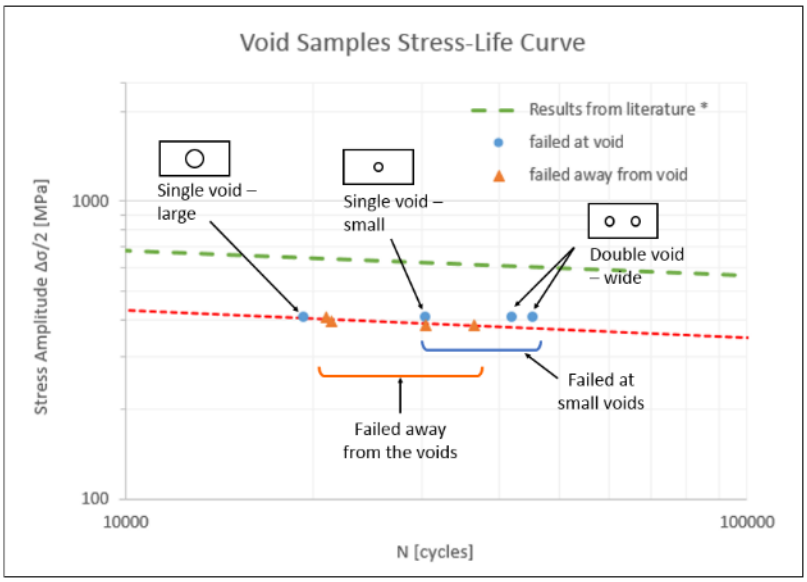

Figure 44 Stress-life curve for the void samples comparing the failure of the small void samples (both single and double) with the failures away from the void. * Stress-life curve from Fournier and Pineau [22] (tests conducted at room temperature and adjusted to R=0.1).

Figure 44 shows the stress life plot for the void samples and compares the small void samples with the samples that failed away from the void. That at least half of the void samples failed at locations other than the voids strongly suggests that there are inherent flaws in the additively manufactured samples that have similar stress concentrations to the intentional voids. Interestingly, the samples that failed away from the voids did not fail orders of magnitude earlier than those that failed at the voids. This relatively small spread in the fatigue life suggests that the magnitude of the stress concentrations due to inherent flaws in the samples were similar to the magnitude of the stress concentrations due to the intentional voids.

From this limited dataset it would also appear that if the sample failed at a stress concentration away from the voids, it was likely to fail earlier than if the greatest stress concentration was at the voids. However, given the limited dataset and the relatively small spread in the number of cycles to failure, more tests would need to be run before any conclusions could be drawn; the spread likely lies within the range expected from scatter within the material.

CHAPTER 6. MICROTRUSS SAMPLES

The second part of this thesis focused on the characterization and testing of the microtruss specimen shown in Figure 45. The advantage of this type of cellular structure lies in its high stiffness to weight ratio and ability to absorb energy. Additive manufacturing is particularly suited to the production of this type of structure [3]. This type of structure may be exposed to fatigue loading, therefore it is important to understand how the structure will fail under these loading conditions.

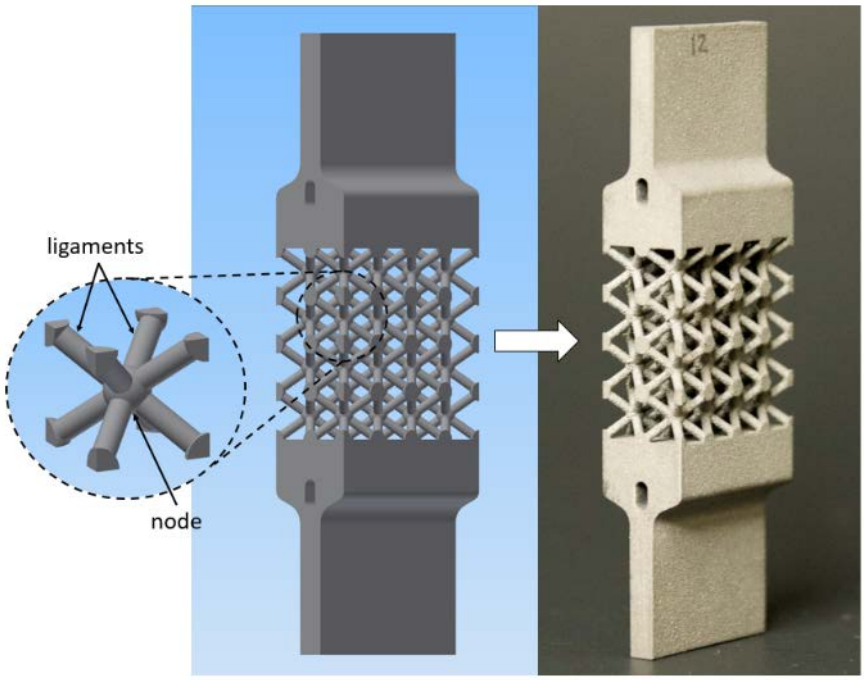

Figure 45 Microtruss specimen

6.1 Specimen Design and Manufacturing

6.1.1 Design – Microtruss unit cell

For ease of design and analysis, microtrusses are generally built from a unit cell. In this thesis, the unit cell was a body-centered cubic structure, as shown in Figure 45. In this type of structure each cell consists of a cube with a node at the center. Ligaments connect this center node to nodes at each corner of the cube. To make this a unit cell, each of these corner nodes is represented as one eighth of a node.

The design of microtruss unit cell went through several iterations prior to manufacture. The initial design was based on that used by Brenne *et al* [14] (shown in Figure 46a). This design was body-centered cubic with square cross-sectioned ligaments. Though still body-centered cubic, the original microtruss design for this thesis, shown in Figure 46b, had cylindrical ligaments. This structure could not be produced by the manufacturer as the ligament diameter was too small. The manufacturer also raised concerns about the intersection between the ligaments. As a result, ligament diameter was increased to 0.5 mm and the design updated to include spherical nodes (φ = 0.866mm) at each joint (Figure 46c).

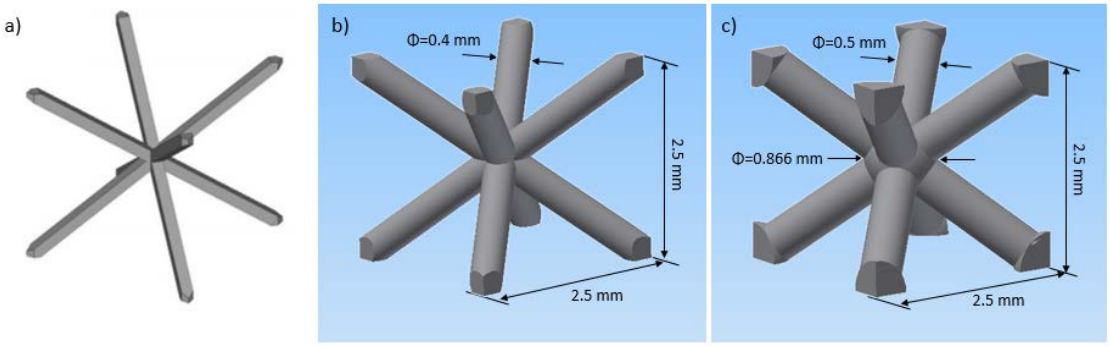

Figure 46 Microtruss unit cell designs.
a) Microtruss unit cell design from [14]. b) Initial microtruss unit cell design based on [14] with cylindrical ligaments; this could not be produced by the manufacturer. c) Initial redesign – note the spheres added at the nodes and the increase in ligament diameter.

However, as shown in Figure 47a, the microtruss design could not be built as the ligaments were too thin to be properly printed. Instead, the manufacturer proposed the design shown in Figure 47c, with significantly thicker ligaments and spherical nodes.

Part of the advantage of the microtruss structure is the relative density which can be calculated as the ratio between the material volume and the filled volume. For example, the microtruss design shown in Figure 46c has a material volume ratio of 18.1%, meaning that only 18.1% of the cube is metal, with the remaining 81.9% being air. This helps to give the microtruss its high stiffness-to-weight ratio. The increase in the diameter of the ligaments and spheres doubled the material volume ratio of the truss which was undesirable. Instead, the entire design was scaled from a 2.5 mm cube to a 5 mm cube. This increases the size of the microtruss without significantly changing the relative density. The final unit cell design is shown in Figure 47d.

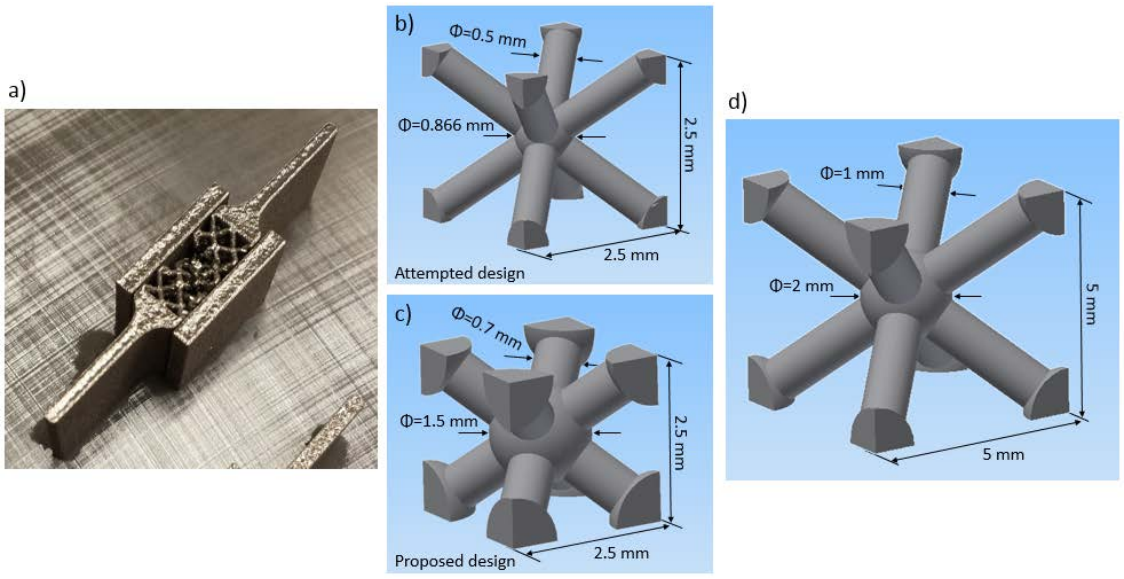

Figure 47 Microtruss unit cell redesign.
a) Failed production of the microtruss design shown in Figure 46c and also shown again here in b). c) Manufacturers proposed design. d) Final microtruss unit cell design. Note that the cell size is $(5\ mm)^3$ up from $(2.5\ mm)^3$ though the relative density remains similar to b).

6.1.2 Design – Grip section

Tensile fatigue testing of the microtrusses required that they be connected to some sort of grip section. This presented an interesting challenge as the grips needed to be thin to fit inside the MTS grips and then expand to accommodate the truss section. The grip section ideally transfers a uniform load into each node of the microtruss. A secondary consideration was the amount of material used to build the grip section as the additional material came at an additional cost.

The grip section went through several design iterations as shown in Figure 48. The aim of the design was to minimize the size, and therefore weight of the grip section by minimizing the distance between the top of the grip section and the point at which load variation across the section reduces to 6%, therefore reducing the cross-sectional area of

the grip and consequently, the volume. The cross-section of the designs were built in Autodesk Inventor, a CAD program, then tested in Autodesk Simulation Mechanical. Though primarily used for component level analysis, Simulation Mechanical provided sufficient finite element analysis capability for this task. Additionally, it's compatibility with Autodesk Inventor made transitioning between design and analysis straightforward. This allowed a range of designs to be developed and tested in short period of time. Figure 49 shows a model of the final grip design with the microtruss.

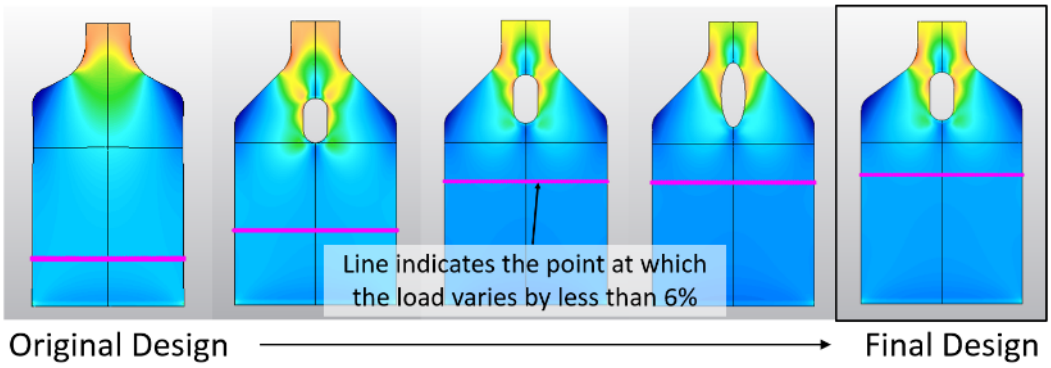

Figure 48 Microtruss grip designs
indicating the point at which the load varies by less the 6% across the specimen.

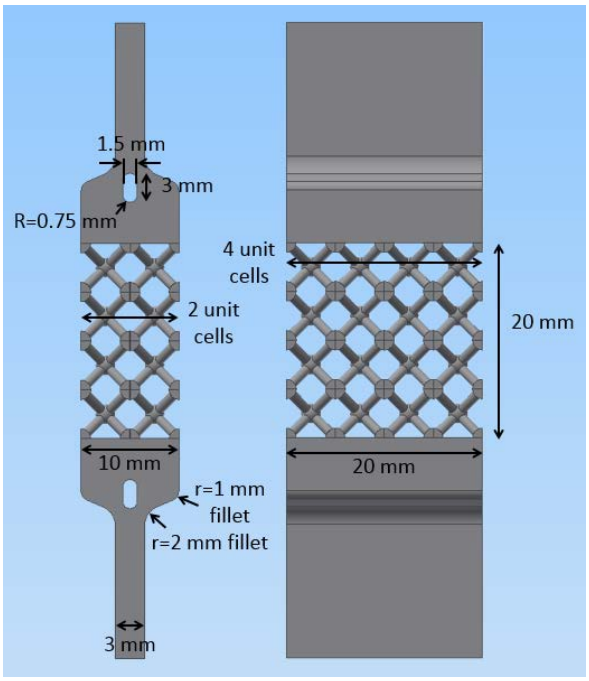

Figure 49 Final microtruss design with measurements.

6.1.3 Manufacturing and post-processing

The microtrusses were built in the direction indicated in Figure 50. The surface was then shot blasted to remove poorly attached powder particles. Note that the intent of the shot blasting is only to remove poorly attached powder particles; not to induce residual stresses. A comparison between the as-built and shot-blasted surfaces is shown in Figure 51. The contour plot clearly shows the difference in variability between the as-built and shot blasted surface. Some of the microtruss ligaments and ligament/node connections are rougher than the external surface shown, as the geometry limits the ability to apply the shot-blasting to some internal parts of the microtruss. The microtruss was then stress relieved, solution heat treated and age hardened as described in section 4.1. Given the limitations of the geometry, no further post-delivery processing was conducted.

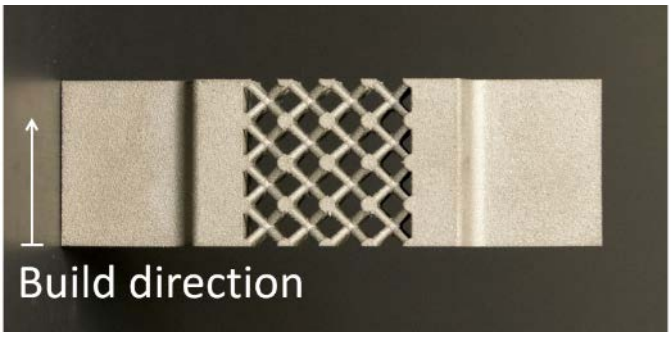

Figure 50 Microtruss build direction.

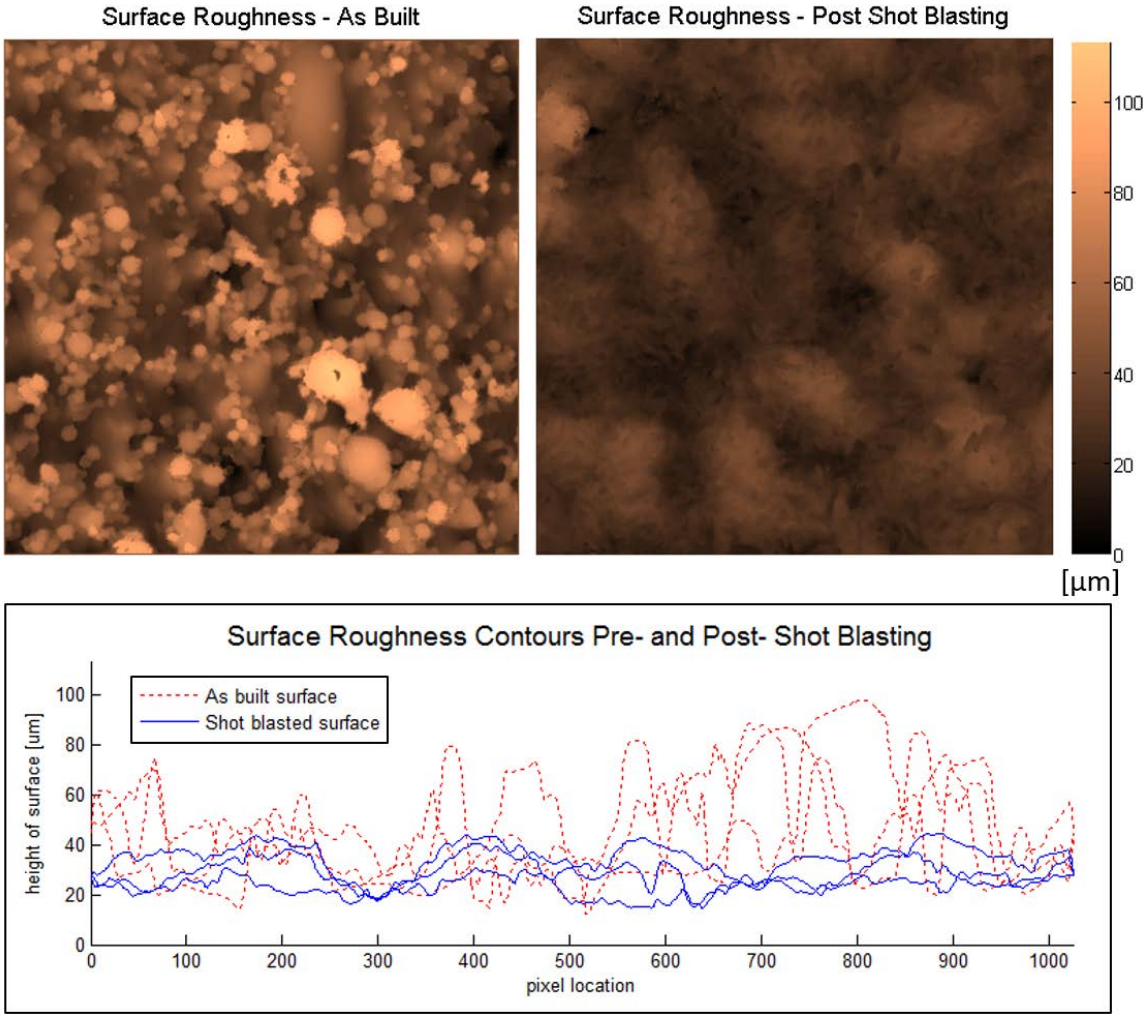

Figure 51 Comparison between the as-built and shot-blasted surfaces.

This as-delivered surface condition is likely to be representative of microtrusses produced in industry, as the geometry severely limits any mechanical surface treatment of internal ligaments or nodes. Therefore, the quality of the as-built surface finish has a significant effect on the surface condition of a microtruss.

6.1.4 As-delivered condition

Of the four microtruss specimens tested, all four had the manufacturing defect shown in Figure 52. Figure 52a and Figure 52b show the defect on the as-delivered specimen. A sectioned view of the microtruss, Figure 52c, shows the nodes that were affected by this defect. Section A in Figure 52 shows the separation surface. This surface is distinctly different from the node-ligament fracture surfaces, and is similar to the as-built surface shown in Figure 51. This indicates that the defective nodes are split in half and that load cannot be transferred through the node. During testing, these nodes separated in all four specimens. Examples of this separation are shown in Figure 53.

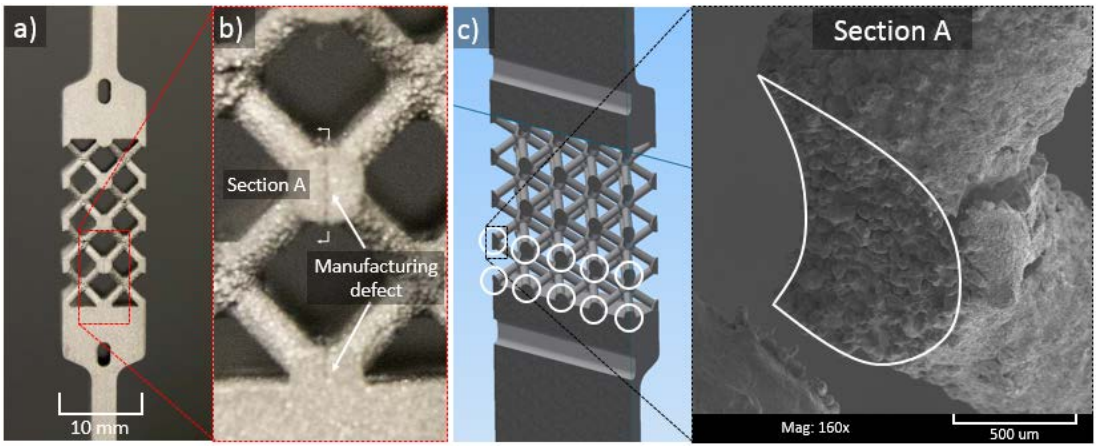

Figure 52 Manufacturing defect in microtruss specimens.

Figure 53 Defective nodes showing separation (post-break) in microtruss specimens.

6.1.5 Microtruss Microstructure

Post-test, a microtruss specimen was ground, polished and etched to reveal grain structure. The grinding removed approximately 0.5 mm from the surface of the microtruss; this was deep enough to allow the etching to reveal the microstructure in a layer where the ligaments joined the node. The microtruss was etched using a Modified Kalling's Reagent. Etching time varied significantly (between 10 s and 90 s) depending on how recently the surface had been polished. The procedure was conducted on two surfaces, one which was parallel to the build direction (Figure 54) and once across the build direction (Figure 55).

Figure 54 depicts the grain structure parallel to the build direction for the node, which has a similar grain structure as the grip. The grains are of similar size and are elongated in the

build direction. This is typical of parts manufactured via DMLS, particularly where the powder and underlying layers are completely melted [31].

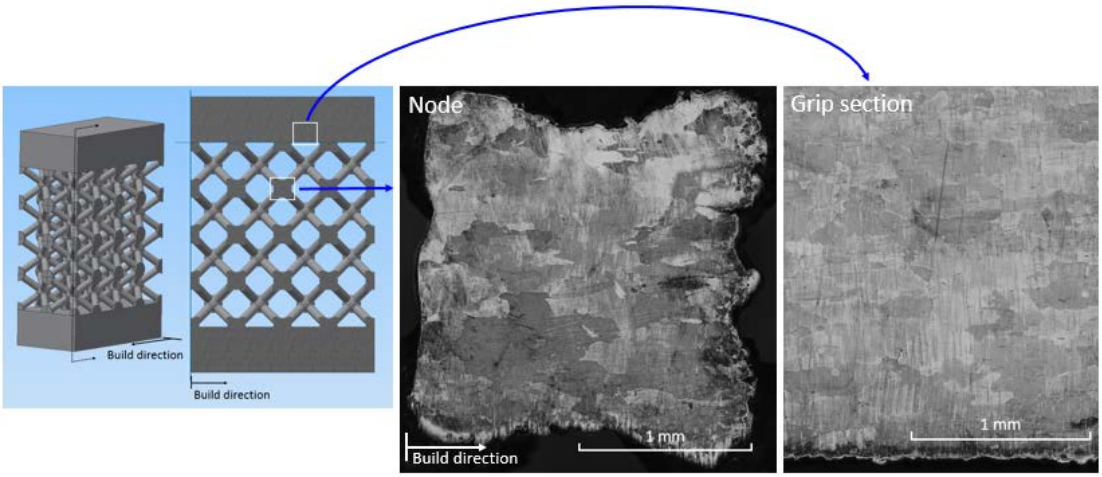

Figure 54 Microtruss microstructure along the build direction at a node and in the grip section. The grains are of consistent size and are elongated in the build direction.

Figure 55 shows the microstructure across the build direction. Here the grains are of a similar size to the grains parallel to the build direction (shown in Figure 54) but are not elongated in any particular direction.

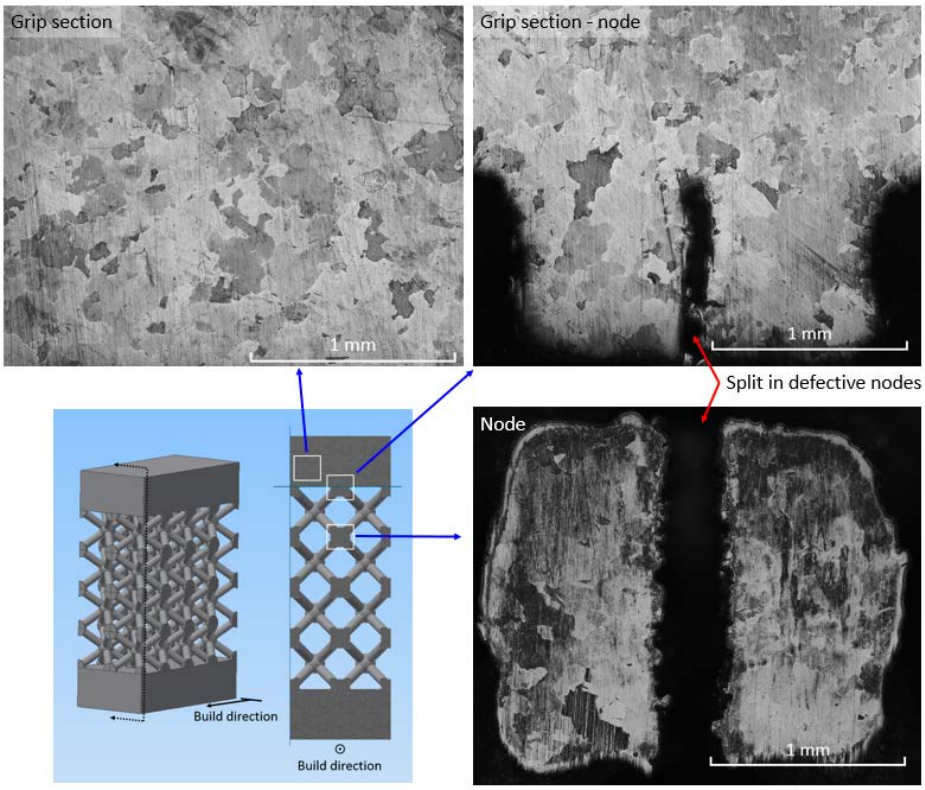

Figure 55 Microtruss microstructure across the build direction in the grip section, at the grip section-defective node transition and at a defective node. Note that the grain sizes and aspect ratios are consistent across all of these locations.

An electron back-scatter diffraction (EBSD) image was taken of part of the node-ligament interface to better visualize and quantify the grain structure in the area. The result is shown in Figure 56. The area proportion of each grain size is shown in Figure 57. A large proportion of the area is taken up by grains of the order of 200 μm in diameter; there are also a number of grains with diameters on the order of 50 μm. The EBSD image in Figure 56 shows that these smaller grains are in regions adjacent to the edge of the sample and where the node transitions into a ligament. The reduction in grain size is likely due to a change in the heat-transfer gradient as a result of the sudden change in cross-sectional area, i.e. the increase in the cooling rate resulted in the formation of smaller grains.

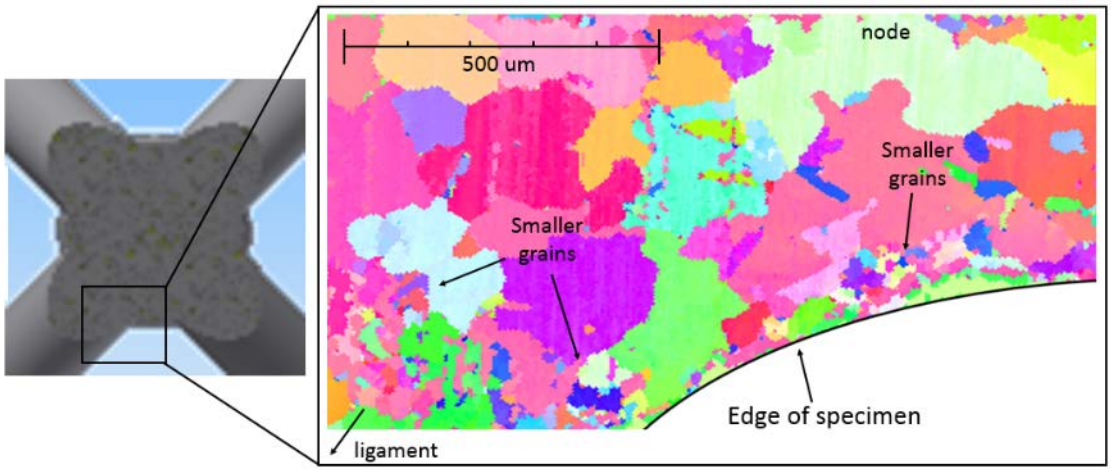

Figure 56 EBSD image of node-ligament interface showing the different grains in the region. Note the regions of smaller grains at the edge of the node and where the node transitions into the ligament.

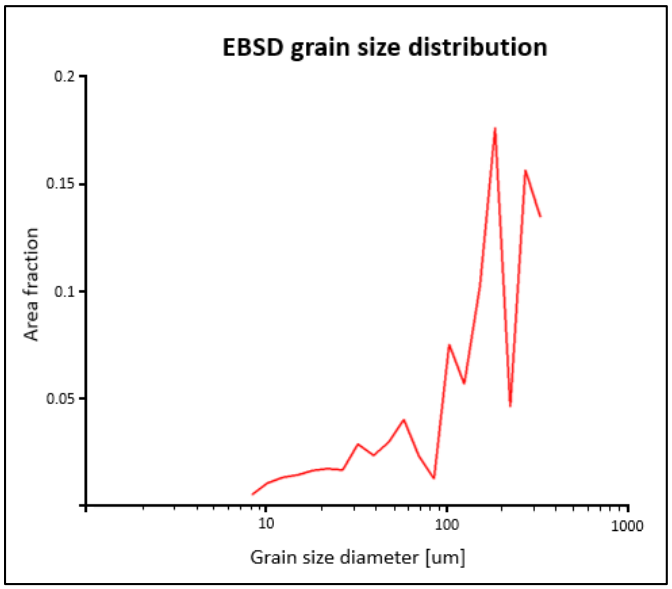

Figure 57 Microtruss EBSD grain size distribution.

6.2 Estimate of stress concentration

The stress concentration in the microtruss was estimated using two methods. The first method is a 2D cantilever beam approximation, which looks at a cross section of the microtruss unit cell and calculates loads at the ligament-node interface assuming that the ligament acts like an angled cylindrical cantilever beam. The analysis is extended to also look at the stresses in the nodes at the edges where only a quarter of the node exists. The second method is a finite element (FE) analysis conducted in ABAQUS on a single ligament with $1/8^{th}$ of a node at each end.

6.2.1 2D cantilever beam model – Ligament-node interface

This 2D analysis approximates the ligament as an angled cantilever beam fixed to the node as shown in Figure 58. The cross section of the microtruss unit cell used to calculate the stress at the ligament-node interface is shown in Figure 59.

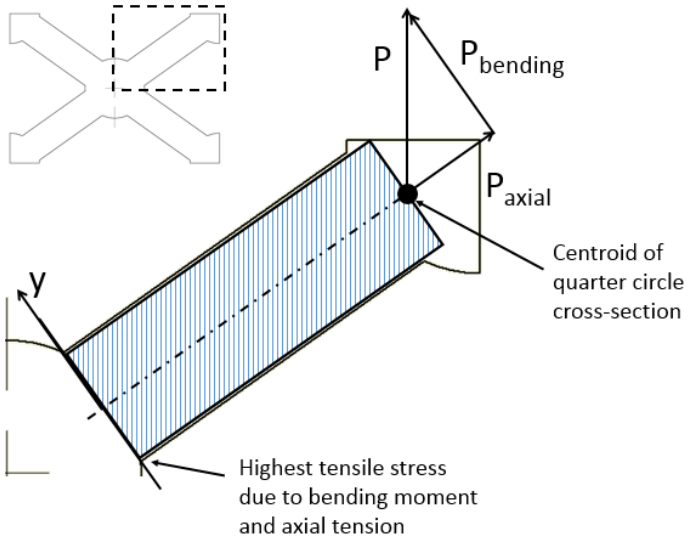

Figure 58 Angled cantilever beam approximation of a ligament.

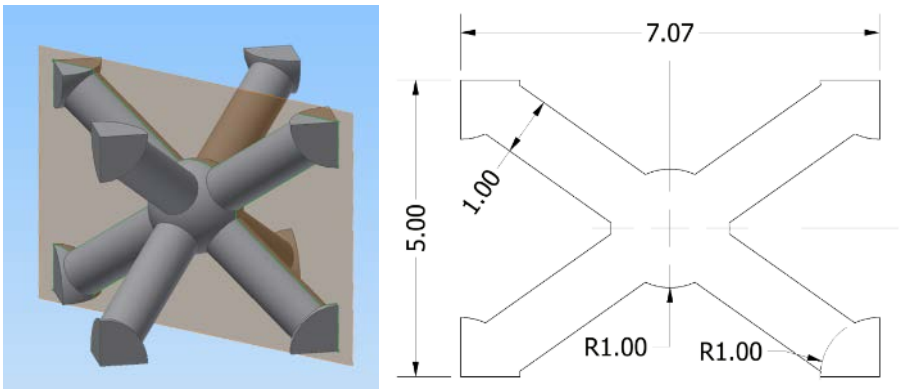

Figure 59 Microtruss unit cell showing the cross-section
used for the cantilever beam analysis, as well as relevant measurements.
Note: all measurements are in millimeters.

Figure 60 shows the loads applied to this microtruss element cross section and examines the loads in the central node. As shown in the free-body diagram in Figure 60b, the load in the central node is equal to the sum of the loads in each of the corner nodes; however, the bending moments cancel out. Therefore, there is no significant concentration of stress in the node itself and the highest stress concentration will be at the ligament-node interface indicated in Figure 58.

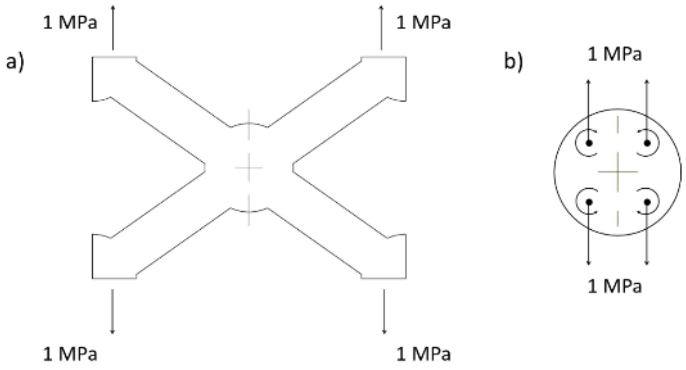

Figure 60 Free body diagrams of microtruss element cross section.
a) 1 MPa load applied to the microtruss element cross-section. b) Free body analysis of the central node of this element. Here the loads at the corner loads have been translated to a load and a moment in the central node. The moments are equal and opposite and cancel each other out.

The cantilever beam approximation of the ligament shown in Figure 58 was used to calculate the highest tensile stress due to an applied load of 1 MPa. Pertinent results are shown in Table 9. The cantilever beam approximation gives a stress concentration factor of approximately 18.4.

Table 9 Calculation results for the beam approximation of the ligament-node interface.

Applied load	1000000	Pa	1.00	MPa
Force	0.7854	N		
P_{axial}	0.4534	N		
$P_{bending}$	0.6413	N		
Axial tensile stress	5.774E+05	Pa	0.5774	MPa
Bending stress				
Moment arm	2.730E-03	m	2.7299	mm
Bending Moment	1.751E-03	N m		
y	-5.000E-04	m	-0.5	mm
I	4.909E-14	m^4		
Bending stress	1.783E+07	Pa	17.8	MPa
Total Stress at base of ligament (Bending stress + axial tension)	1.841E+07	Pa	18.4	MPa
Stress concentration	18.4			

6.2.2 2D beam model – Quarter node region

The second region of interest is the nodes at the edges of the specimen that are a quarter of a sphere. Most of the quarter nodes broke through the center of the node, rather than at the ligament-node interface (see Figure 67). This is because, unlike the spherical nodes, the bending moments from the ligaments are not balanced out. Additionally, the node's cross-section is less than the cross section of the ligament-node interface, therefore, the highest stress is through the center of the node. This causes the node to break through the center. The analysis that follows approximates the quarter node as a 2D (quarter sphere) beam.

Similar to the analysis of the central node, Figure 61 shows the free body analysis of the node. Again, the applied loads are translated into a load and a moment in the quarter node beam. The moments are equal and opposite. The results of pertinent calculation steps are shown in Table 10. The beam approximation gives a stress concentration factor of approximately 13.

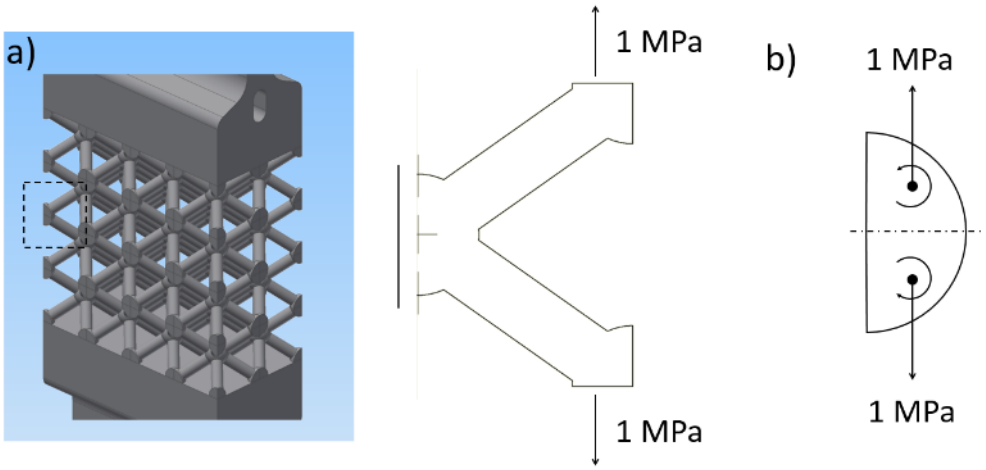

Figure 61 2D beam model of quarter node.

Table 10 Calculation results for the beam approximation of the quarter-node.

Ligament length	2.330E-03	m	2.330	mm
Applied load	1.000E+06	Pa	1.000	MPa
Force	0.7854	N		
$P_{tension}$	0.7854			
Tensile Stress	1.000E+06	Pa	1.000	MPa
Moment arm	2.730E-03	m	2.730	mm
M - Bending moment	2.144E-03	Nm		
y - distance from centroid of node to edge	-3.998E-04	m	-0.400	mm
Angle	9.000E+01	deg		
I	7.135E-14	m^4		
Bending Stress	1.201E+07	Pa	12.014	MPa
Total Stress through center of the quarter node	1.301E+07	Pa	13.014	MPa
Stress concentration	13.0			

6.2.3 ABAQUS Finite element analysis

Finite element analysis was conducted on a single ligament, with $1/8^{th}$ of a node at each end, to estimate the stress concentration where the ligament joined the node. The modelled element is shown in Figure 62.

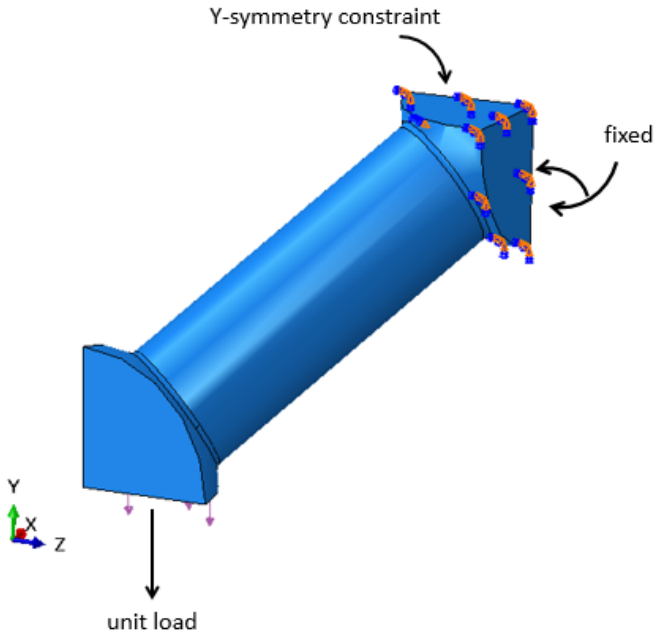

Figure 62 ABAQUS model of single ligament.

Fillets were added to the ligament-node interfaces to accurately represent the as-built structure. The fillet radius was based on the manufacturers published part accuracy of 40 μm – 60 μm for small parts. Given that the ligament-node interface would be built over successive layers, the fillet radius is likely to be on the order of 100 μm. Note, however, that the fillet radius is based on an approximation, further work is required to quantify the radius and then rerun the analysis.

Figure 63 shows the FE results for a single ligament model with a 100 μm fillet radius. The model was meshed using 10-node quadratic tetrahedral elements. The global seed size was set at 0.01 resulting in 11.6 million nodes and 8.3 million elements. The stress concentration at the ligament-node interface was calculated to be 28.37. Models with smaller fillet radii were also analysed and, as expected, show that reducing the fillet radius significantly increases the stress concentration at the ligament-node interface.

FE static stress concentration results for the single ligament model with 100 μm fillet: $K_t = 28.37$

Given the significant effect that the fillet radius has on decreasing the stress at the ligament-node interface (the most highly stress portion of the microtruss), and the very small effect is has on the volume ratio of the microtruss, it may be worth considering including fillets into the microtruss design in the future.

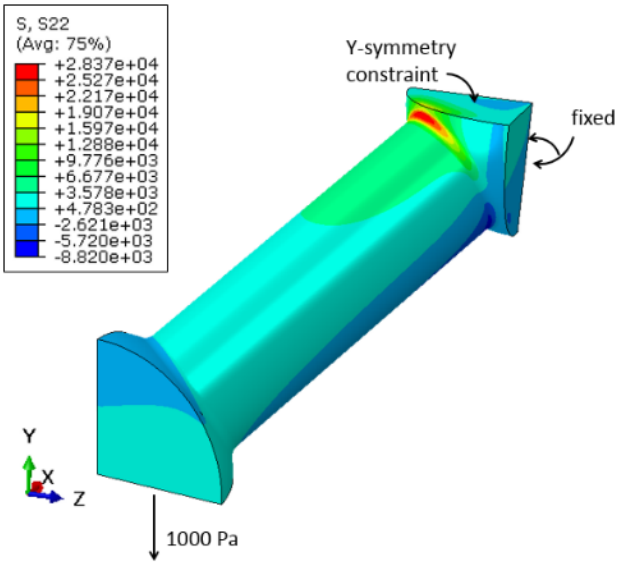

Figure 63 ABAQUS results using 0.1 mm fillet radius

6.3 Tensile test results

The first microtruss specimen was tested in tension in order to determine the effective elastic modulus (E), yield stress (σ_{yield}) and ultimate tensile strength (σ_{UTS}).

6.3.1 Stress data

MTS force data was converted to stress based on the minimum cross-sectional area of the truss region. The location of the minimum cross-sectional area was determined by

measuring the cross-section of the CAD model at various heights using Autodesk Inventor. The results are shown in Figure 64, the cross-sectional area is symmetrical about the center of the central node. The plot shows that the minimum cross-section is at the center of the nodes.

Microtruss minimium cross-sectional area: 25.13 mm^2

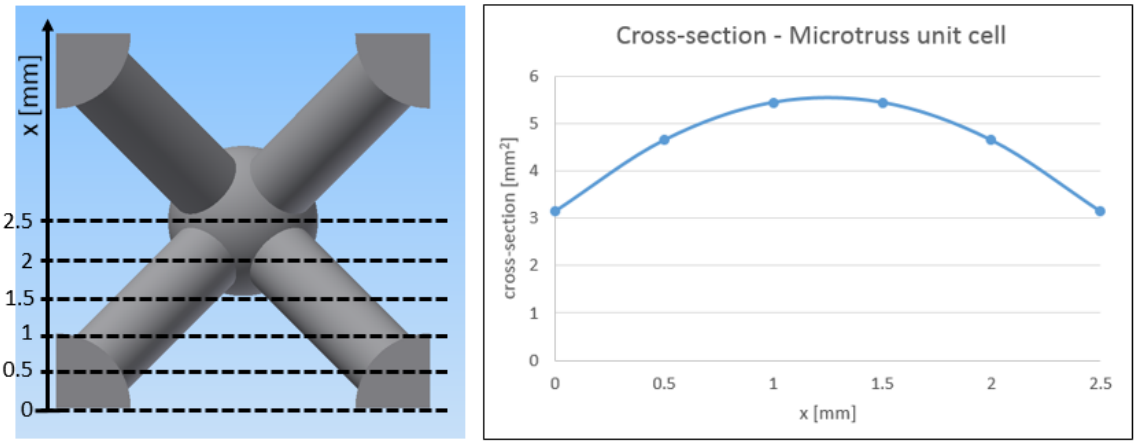

Figure 64 Cross-sectional area of a unit cell.
The plot shows the minimum cross-sectional area is at the center of the nodes.

6.3.2 Strain data

The microtruss specimens were not fitted with extensometers, instead, strain data was determined using the MTS crosshead displacement data and the following process.

For the first cycle, the microtrusses undergoing fatigue testing were imaged successively while unloaded, at minimum load, and at maximum load. From these images, ImageJ was used to determine the strain in the microtruss at each load. The strain was then compared to the crosshead displacement at each point. The linear fit in Figure 65 was used to convert the crosshead displacement into strain.

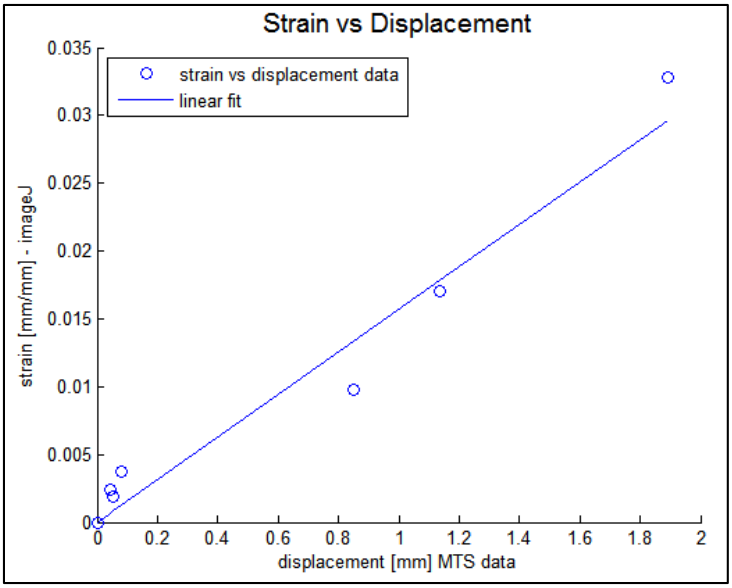

Figure 65 Strain determined in ImageJ compared to MTS crosshead displacement data.

6.3.3 Stress-strain curve and results

The tensile stress-strain plot for the microtruss is shown in Figure 66. The linear portion of the curve was used to determine the effective elastic modulus. The tensile test results are summarized in Table 11, these are very low compared to the previously obtained tensile results. The differences in the tensile properties are to be expected as the microtruss ligaments have more in common with truss elements (transferring only axial loads) than bulk material. The geometry of the microtruss also results in a cross-sectional area that varies throughout the truss with a corresponding variation in stress.

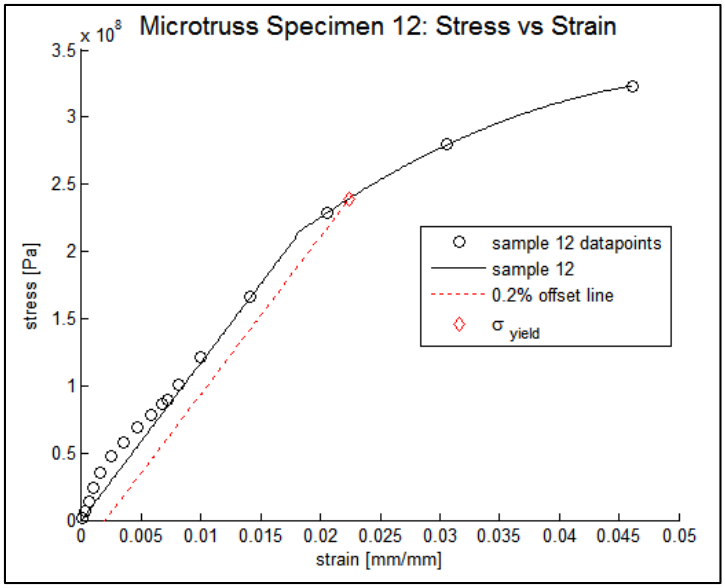

Figure 66 Microtruss stress-strain curve showing 0.2% offset and corresponding σ_{yield} point.

Table 11 Microtruss properties from tensile testing compared to material properties.

Material property	**Microtruss values**	**Dogbone tensile values**
Elastic Modulus - E	11.74 GPa	166.45 GPa
Yield Stress - σ_{yield}	238.5 MPa	1005.77 MPa
Ultimate tensile strength – σ_{UTS}	323.2 MPa	1220.80 MPa

6.4 Fatigue test and results

Fatigue testing was conducted under load control with guidance provided by ASTM E466 [9].

6.4.1 Fatigue test parameters

The fatigue test parameters are summarized in Table 12 and Table 13. A stress ratio of R = 0.1 was chosen to ensure that the microtruss was not compressed during testing as this would likely lead to ligament buckling.

Table 12 Microtruss fatigue test parameters.

Parameter	Value
Frequency	0.5 Hz
Stress ratio, R	0.1
Wave shape	Sinusoidal

Table 13 Microtruss fatigue test stress and load parameters.

Stress and load parameters				
Specimen 13	σ_{max} = 238.7 MPa	$\sigma_{max} \approx$ 1.0 σ_{yield}	F_{max} = 6.00 kN	$\Delta\sigma/2$ = 107.4 MPa
Specimen 14	σ_{max} = 198.9 MPa	$\sigma_{max} \approx$ 0.83 σ_{yield}	F_{max} = 5.00 kN	$\Delta\sigma/2$ = 89.52 MPa
Specimen 15	σ_{max} = 159.2 MPa	$\sigma_{max} \approx$ 0.67 σ_{yield}	F_{max} = 4.00 kN	$\Delta\sigma/2$ = 71.62 MPa

6.4.2 Microtruss failure mode

Final failure of the microtruss begins when one of the ligaments fails in fatigue. This typically occurred at a ligament-node interface. Figure 67 shows a failed microtruss and highlights the failure locations. Though failure generally occurred at ligament-node interfaces, failure at the edges of the microtruss occurred through the quarter nodes (rather than at the ligament-node interface), both of these failures are shown in Figure 67

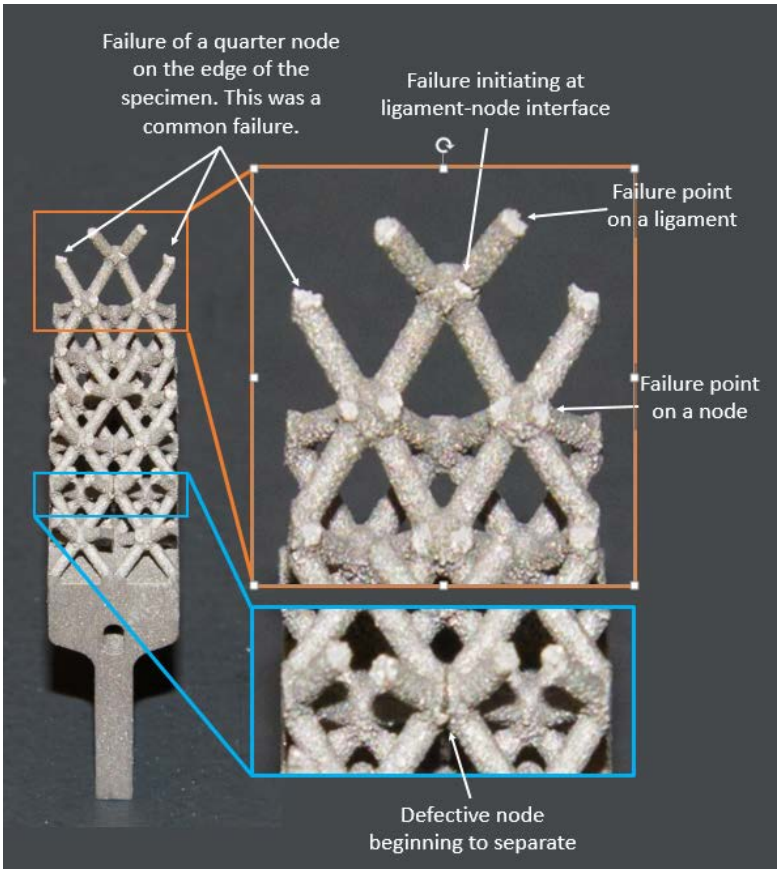

Figure 67 Failed microtruss showing failure at ligament-node interfaces and through the quarter nodes at the edge of the specimens.

Figure 68 shows a typical failure sequence using results of digital image correlation and photos taken for digital image correlation. Correlation of the images was conducted in Vic-2D with a subset size of 31 pixels and a step size of 1 pixel.

Figure 68a shows the specimen before any of the ligaments fail. Here the stress is low and evenly distributed throughout the microtruss. After 1952 cycles, the first ligament fails, shedding load and increasing the stress in the local region indicated in Figure 68b. This accelerated damage accumulation in the area until, at 2179 cycles, the defective node, indicated in Figure 68c fails, significantly increasing stresses in the surrounding region. Further cycling results in a third ligament failing at 2214 cycles, as shown in Figure 68d. Here, the failure of this ligament significantly weakened the structure and the structure failed catastrophically just after the image was taken.

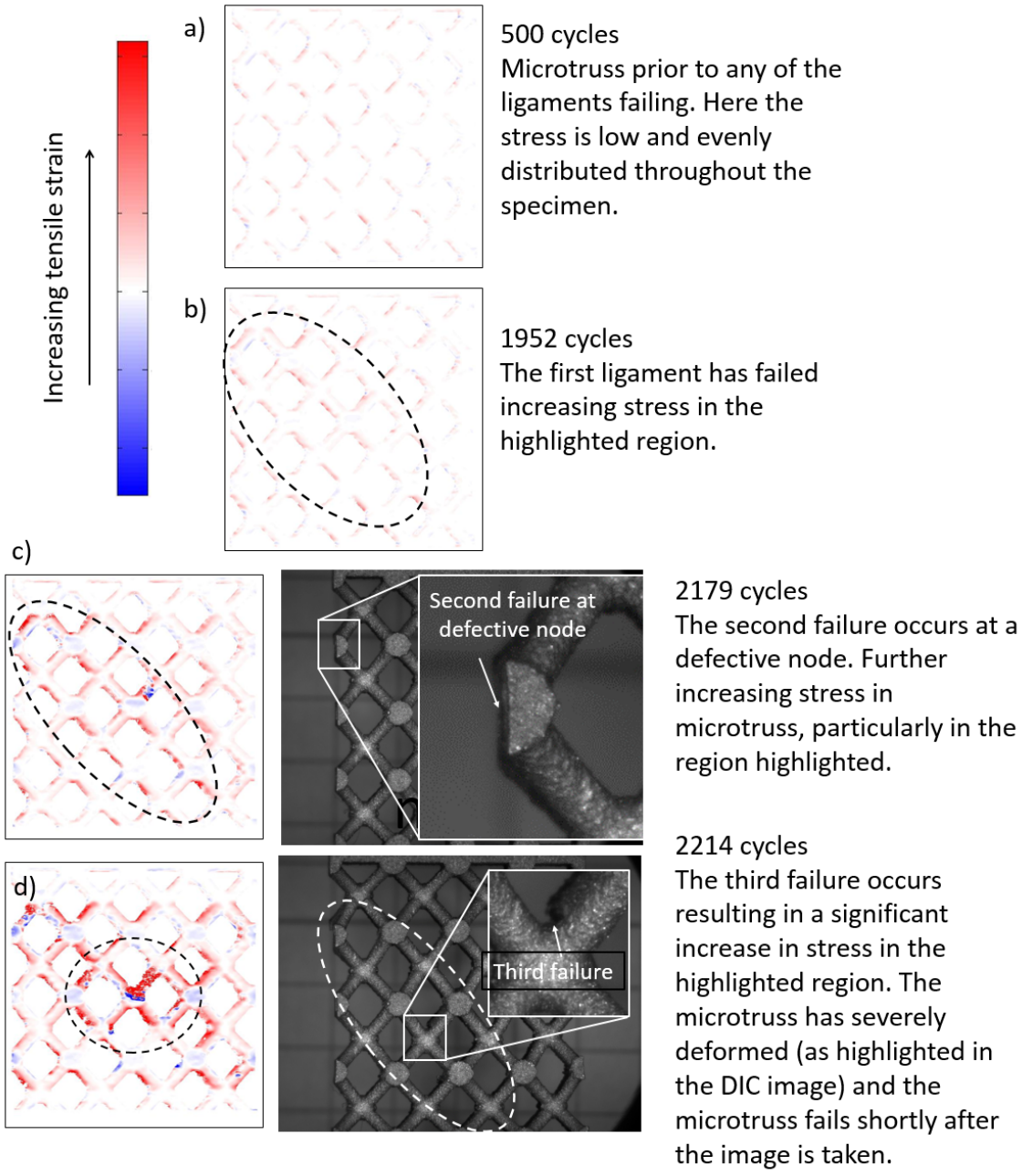

Figure 68 Microtruss failure sequence.

This failure sequence highlights that the integrity of the microtruss structure is strongly linked to the strength of the first ligament to fail, commonly referred to as the weakest link. Failure of this link leads to an increase in local stresses, rapidly initiating subsequent

failures. A similar failure progression was observed by Li *et al.* [17] in compressive fatigue loading.

6.4.3 Fatigue failure results

Failure of the microtruss specimens is presented in Figure 69 along with the smooth specimen data [22] (adjusted to R=0.1) and the data from the void specimens. Here, the stress amplitude is based on the stress at the minimum cross section of the microtruss.

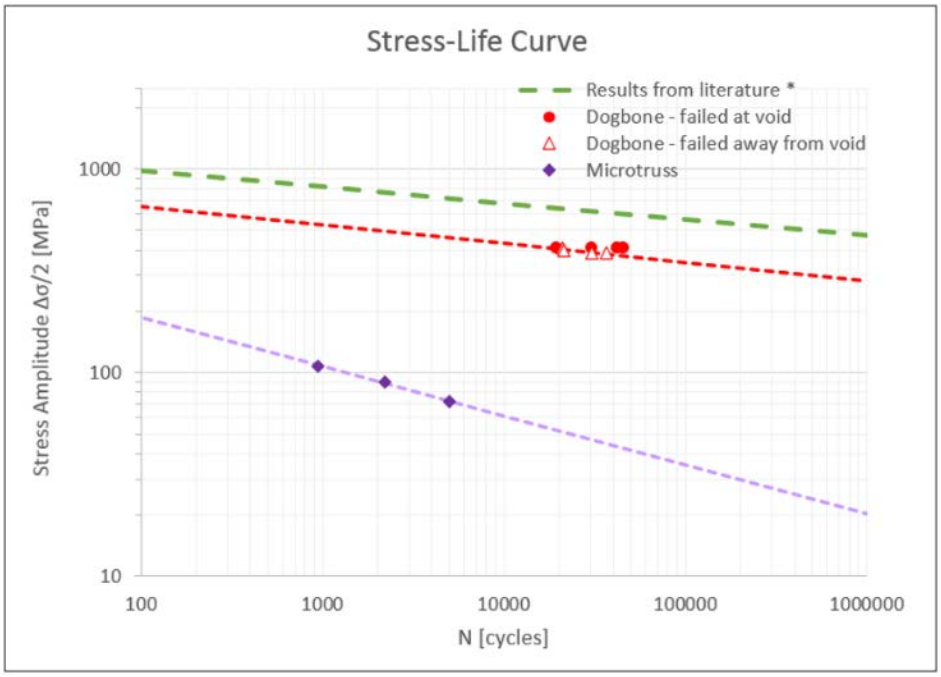

Figure 69 Microtruss stress amplitude vs life data with power law fit (R = 0.1).
* Stress-life curve from Fournier and Pineau [22] (tests conducted at room temperature and adjusted to R=0.1).

Table 14 shows the fatigue strength of the microtrusses and compares the results with the smooth fatigue strength from Fournier and Pineau [22] (tests conducted at room temperature and adjusted via the Walker parameter to R=0.1). K_f is calculated for the

data, then compared to the K_t value from Section 6.2.2, to determine q, the notch sensitivity factor.

Table 14 Microtruss specimen fatigue results showing K_f, K_t and q.
* Smooth fatigue strength is based on results from Fournier and Pineau [22] (tests conducted at room temperature and adjusted to R=0.1).

Specimen	$\sigma_{max}/\sigma_{yield}$	N [no. cycles]	$\Delta\sigma/2$ [MPa]	Smooth fatigue strength* [MPa]	K_f	K_t	q
Specimen 13	1.0	940	107.4	821.31	7.645	18.4	0.38
Specimen 14	0.83	2214	89.52	766.90	8.566	18.4	0.43
Specimen 15	0.67	5039	71.62	718.07	10.026	18.4	0.52

The void sample results suggest that the samples had inherent defects that were of similar magnitudes to the voids that were intentionally placed in the samples. Therefore, instead of comparing the microtruss results to the adjusted Fournier and Pineau [22] values, it makes more sense to compare them to the results from the samples that failed away from the void (these do not require adjustment for mean stress as the testing was conducted at R = 0.1). Table 15 compares the 'smooth' fatigue strength determined from the samples that failed away from the voids with the actual fatigue strength of the microtrusses, then calculates the K_f and compares this to the calculated K_t from the beam approximations in section 6.2.1. The notch sensitivity factor, q is then calculated from these values. Compared to Table 14, the primary change is in the smooth fatigue strength, which changes K_f and q. Comparing the microtruss failures with values based on the samples

that failed away from the voids gives a lower K_f and a corresponding decrease in notch sensitivity. This recognizes the effect that the inherent defects in the material have on the fatigue life. These values are used throughout the remainder of this thesis.

Table 15 Microtruss specimen fatigue results showing K_f, K_t and q.
(* values based power law fit of samples that failed away from the void)

Specimen	$\sigma_{max}/\sigma_{yield}$	N [no. cycles]	$\Delta\sigma/2$ [MPa]	Smooth fatigue strength* [MPa]	K_f	K_t	q
Specimen 13	1.0	940	107.4	533.33	4.964	18.4	0.23
Specimen 14	0.83	2214	89.52	492.91	5.506	18.4	0.26
Specimen 15	0.67	5039	71.62	456.99	6.381	18.4	0.31

The q for the microtrusses is significantly lower than that for the void specimens (an average of 0.45 – based on Table 14, or 0.27 – based on Table 15 for the microtrusses compared with an average of 0.55 for the void specimens) suggesting that the microtrusses are less notch sensitive than the void specimens. This is likely because the ligaments undergo significantly more strain and yielding than the void specimens. This higher strain blunts the crack initiation sites and crack tips more effectively, reducing the notch-sensitivity of the microtruss.

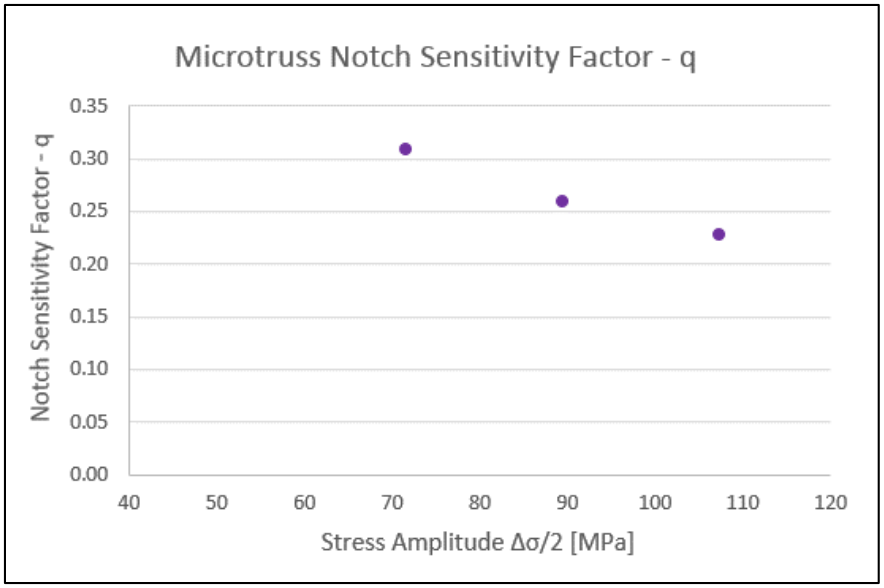

Figure 70 Microtruss notch sensitivity factor
as a function of stress amplitude (Stress ratio, R = 0.1).

Figure 70 shows the change in the notch sensitivity factor as a function of stress amplitude. The data suggests that the microtruss notch sensitivity increases as the stress amplitude decreases. That is, the microtruss is more notch sensitive at lower loads. This is likely because, at higher loads, the sharp, high K_t notches are blunted in the first few cycles, significantly reducing their effect on the microtruss. Whereas the lower loads fail to effectively blunt these sharp cracks, allowing them to remain and initiate cracking. Further testing is required to confirm these results; since the q values are determined at different N (cycles to failure), they are not directly comparable.

6.5 Outcomes and analysis

6.5.1 Assessment of manufacturing defect

In Section 6.1.4, Figure 52 and Figure 53 (reproduced below) showed the manufacturing defect that appeared in all of the microtruss specimens. In general, this did not appear to effect the failure of the microtruss. The separation of the defective nodes effectively changed the nodes from spherical to hemispherical along the defect line; the loading conditions would be similar to that presented in Section 6.2.2 for the quarter nodes which means that the highest stress concentration would still be at the ligament-node interfaces rather than through the center of the defective, hemispherical nodes. The only location where the defect may have had an effect is seen in the left-hand photo of Figure 53 (highlighted in the reproduction below) which shows that the node has failed through the center as if it was a quarter node rather than a hemispherical node (which would normally fail at the ligament-node interface). In one instance, this was one of the first failure locations.

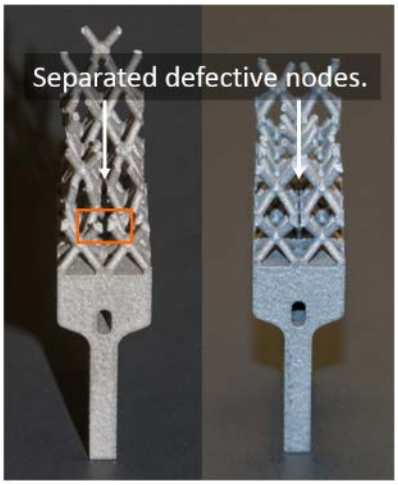

Figure 53 Defective nodes showing separation (post-break)
in microtruss specimens.

6.5.2 Failure surface analysis

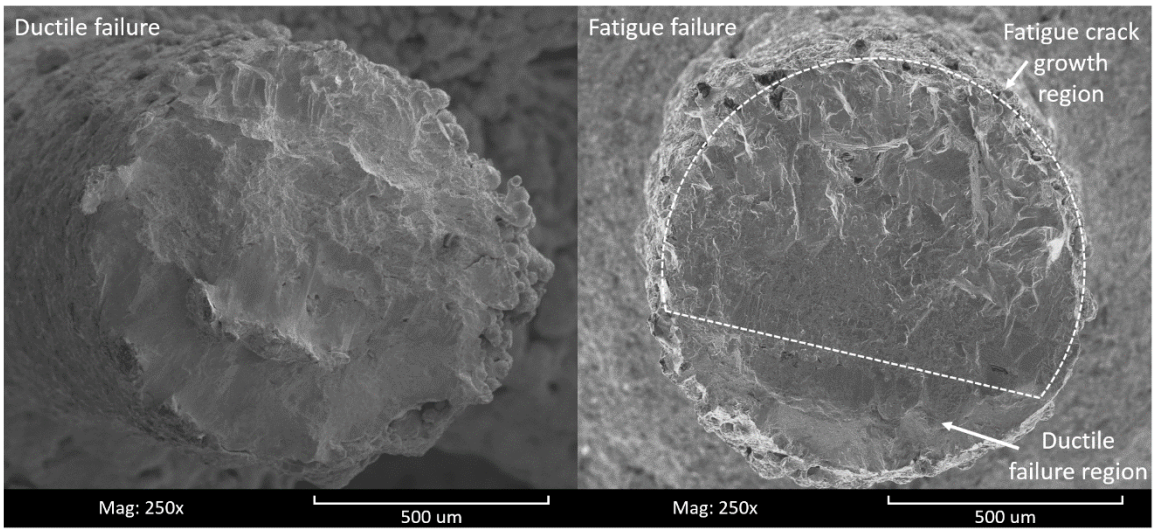

Figure 71 SEM images of ligament fracture surfaces showing two failure mechanisms. The ligament on the left experienced catastrophic ductile failure after much of the rest of the microtruss had failed. The ligament on the right failed in fatigue and was one of the first ligaments to fail.

Figure 71 shows the SEM images of two ligaments' fracture surfaces. The ligament on the left failed catastrophically after most of the microtruss had failed. There is no evidence of any fatigue crack growth on the ligament fracture surface. The ligament on the right was one of the first ligaments to fail. The fracture surface shows a large region of crack growth initiating from several sites along the surface of the ligament growing inwards. The images in Figure 71 confirm that not all of all of the ligaments failed in fatigue. Future work should focus on identifying which ligaments began to fail in fatigue and what characteristics predisposed the ligament to fatigue crack initiation.

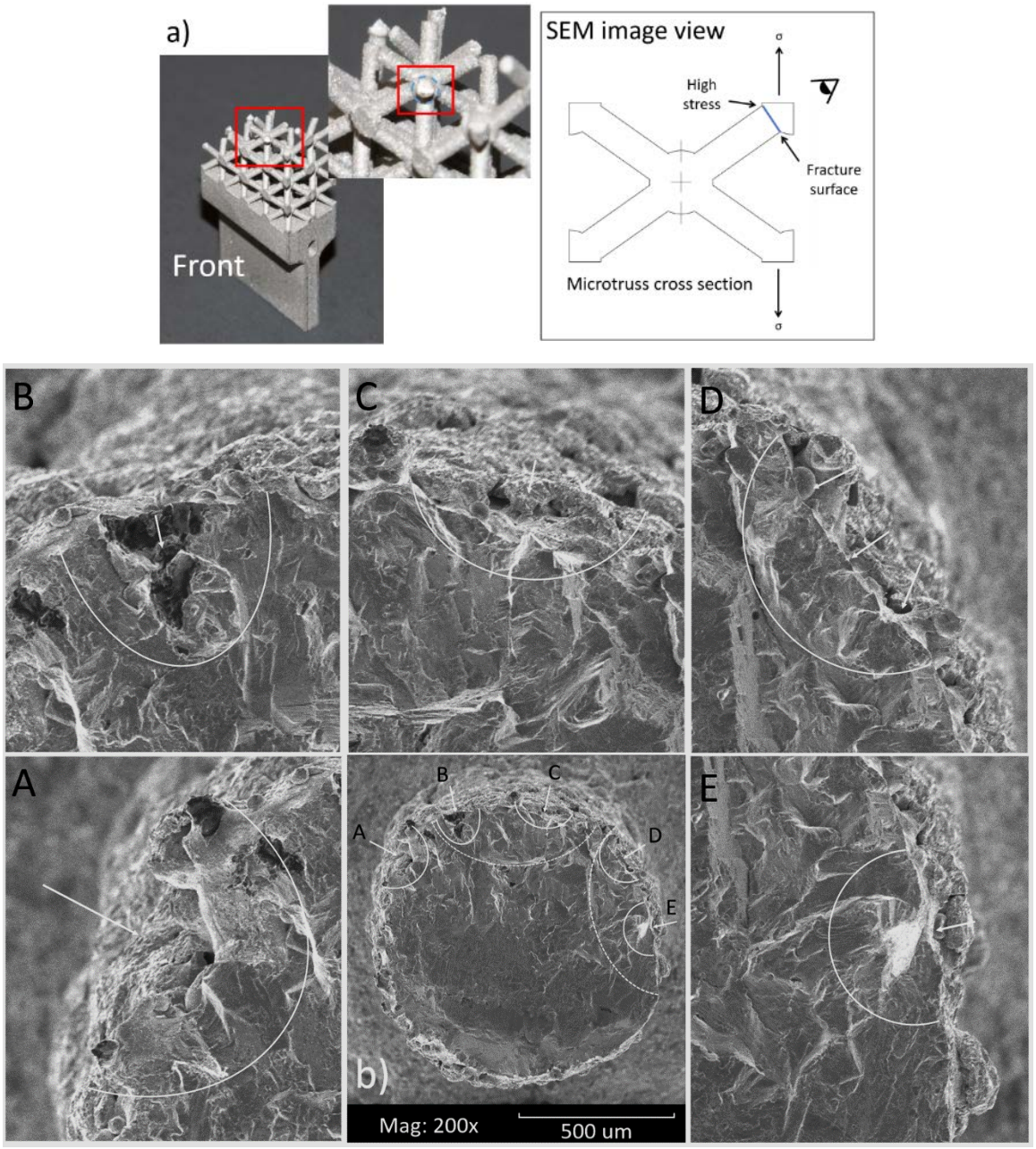

Figure 72 Typical ligament-node failure surface.
a) Location of the SEM images in relation to the remainder of the microtruss and the loading. b) SEM image of the failure surface showing the multiple initiation sites and their initial growth. Dashed white lines indicate the crack growth after initial cracks have merged. Images A-E to shows the individual crack initiation sites. All of the cracks initiated at deep surface defects.

Figure 72 shows SEM images of a typical ligament-node fatigue failure surface. The location of the ligament and the loading conditions are shown in Figure 72a. The surface analysis (Figure 72b) shows several crack initiation sites, typical in low cycle fatigue [35]. All of the cracks have initiated at the top surface of the ligament, consistent with the location of highest tensile stress. The cracking has initiated at relatively deep surface defects and grown downwards into the ligament. As mentioned in section 6.1.3, the internal ligaments and nodes have a much rougher surface finish than the external areas; leading to more of these deep surface defects and a greater susceptibility to crack initiation. Since the geometry of the sample restricts access to the defects, they are, in essence, a characteristic of a particular DMLS process and machine type.

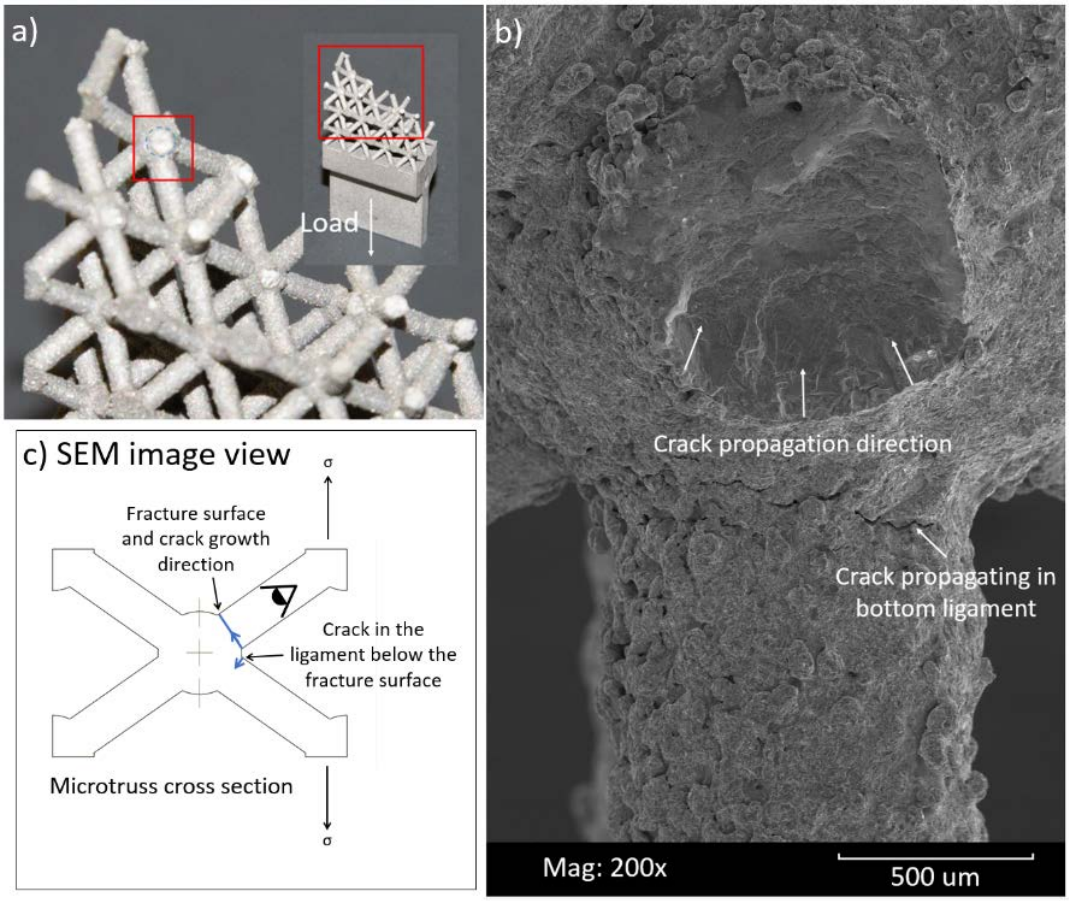

Figure 73 SEM image of a failure surface on a node showing the crack propagation direction. a) The location of the node in relation to the rest of the microtruss. b) The SEM image showing the fracture surface and a crack propagating in another ligament attached to this node. Note that the cracks are growing in opposite directions as expected given their relation to the loading direction (shown in the illustration). c) The SEM image in relation to the loading and calculations carried out on Figure 61 – the 2D beam model of a quarter node.

Figure 73 shows the node side of a ligament-node failure. The ligament failed in fatigue loading. Cracking initiated along the bottom of the ligament and propagated upwards as indicated on the image. A similar crack is seen in the ligament below the fracture surface. The crack initiation locations and growth direction confirm the location of the highest stress concentration suggested in the analysis of the ligament-node interface conducted in section 6.2.1.

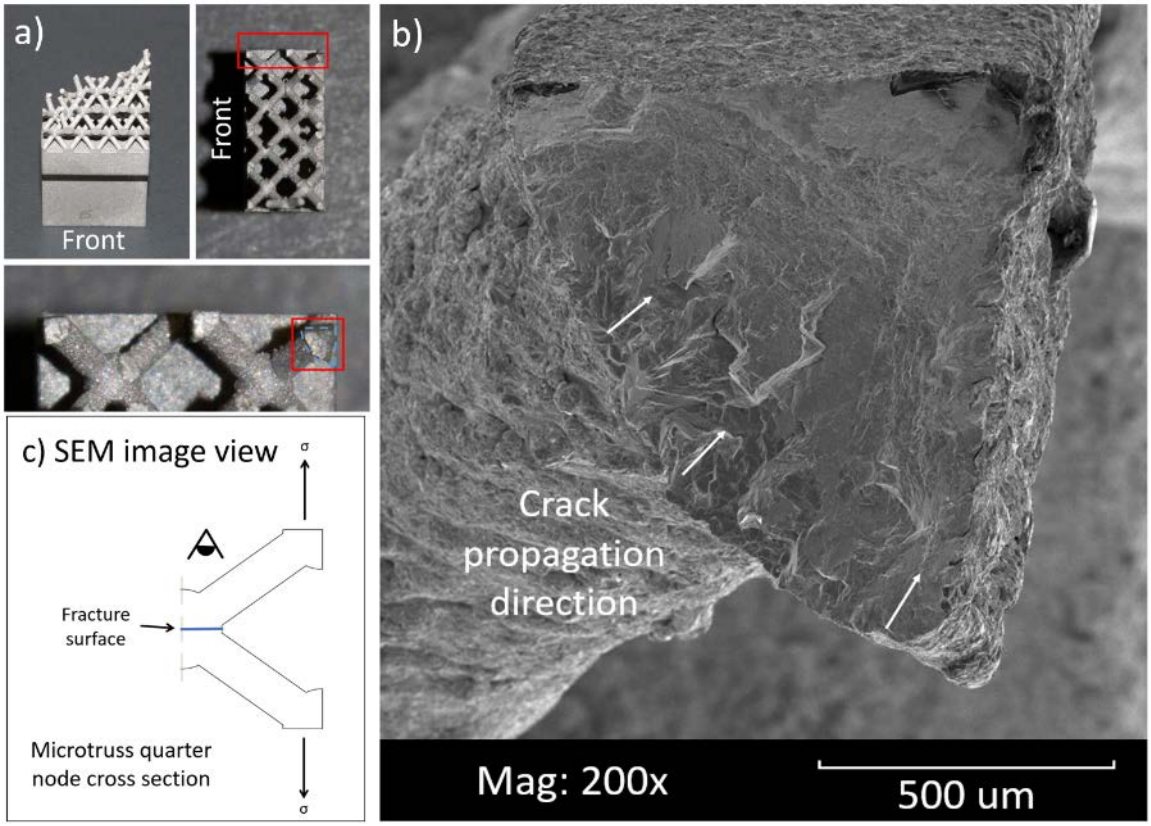

Figure 74 SEM image of a quarter node failure surface.
a) The location of the node in relation to the rest of the microtruss. b) The SEM image showing the fracture surface. Here the crack initiates at the curved surface of the node and grows towards the corner. c) The SEM image in relation to the loading and calculations carried out on Figure 60 – the cantilever beam approximation of a ligament.

Figure 74 shows the fracture surface across a quarter node. The fatigue failure occurred through the center of the quarter node and cracking has initiated on the curved side of the quarter node and grown outwards as indicated in Figure 74b. The initiation of the cracking at the curved node surface and its growth towards the corner support confirms the location of highest stress suggested by the simple 2D beam analysis of the quarter node in section 6.2.2.

6.5.3 Failure order analysis

Analysis of the DIC images just prior to failure did not highlight any particular region of ligaments that were more prone to failure (a location-based preference for failure of this sort would likely indicate common manufacturing defects or problems with loading conditions). The review did find that in all of the failures, the first ligament to fail was internal. The ligament-node interfaces at the surface of the specimen were never the first to fail, and rarely failed until just cycles before catastrophic failure.

This is likely because the outer ligaments have the benefit of being shot-blasted. In this process, loose powder and material is removed and the surface finish significantly improved, as shown in Figure 51. This reduces the likelihood that the deep pitting, shown in Figure 72b to be likely crack initiation sites, exists at the highest stressed locations at the ligament-node interfaces. Therefore, the likelihood of crack initiation at these surface finished interfaces is reduced. Figure 75 shows the surface finish on nodes from three different locations in the microtruss. The most consistent surface finish is seen on the external side of an external node (A), i.e. a node that is exposed to the outside of the microtruss. The second best finish is seen on the internal side of an external node (B) and the roughest surface finish is seen on an internal node. The roughness of these inner nodes increases the likelihood of deep pitting and subsequent crack initiation at these nodes; this is likely the reason for their early failure.

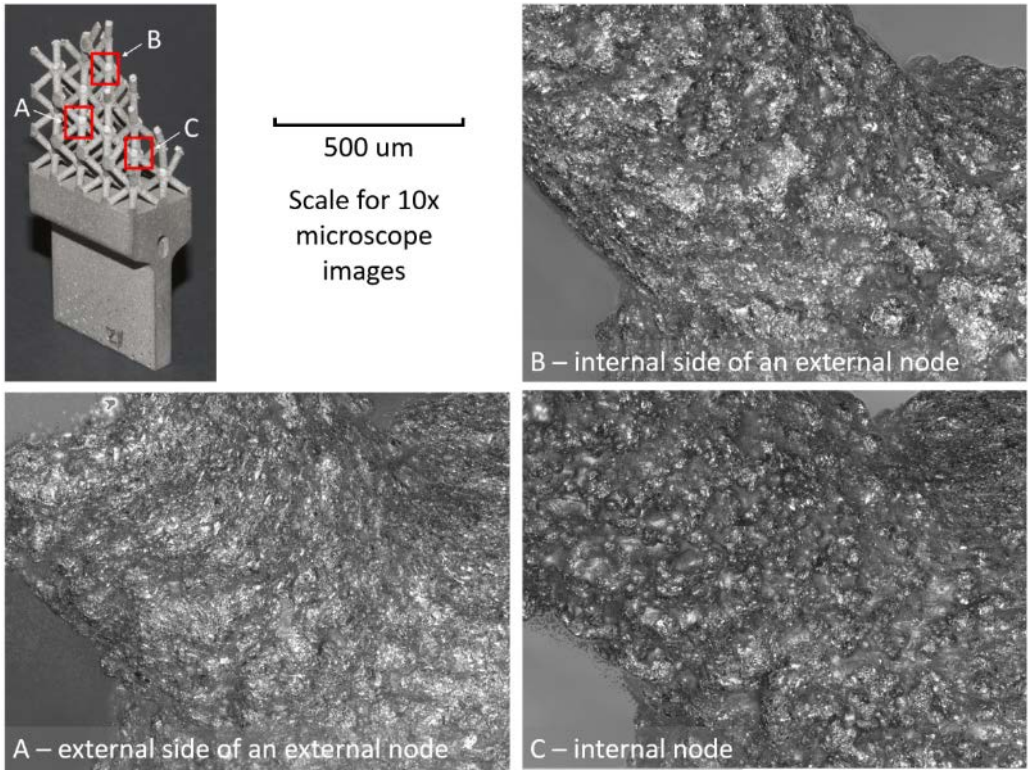

Figure 75 Surface finish of nodes from different locations within the microtruss. The most consistent surface is on the external side of the external node, as expected. The roughest surface is on the internal node.

CHAPTER 7. SUMMARY AND CONCLUSIONS

7.1 Void Samples

Four void configurations were tested under fatigue loading. Two configurations contained a single void, one small (0.5 mm) and one large (1.0 mm), and two configurations contained double small voids separated by one and two void diameters respectively (0.5 mm and 1.0 mm, respectively). The separation is measured from the edge of one void to the closest edge of the other void. The void configurations were additively manufactured into the center of the gauge section of dogbone specimens. The samples were then stress-relieved, solution heat-treated and age hardened according to the process detailed in Section 4.1. Prior to testing, the face of the samples were polished to remove surface defects that could initiate cracking and to allow the application of a DIC stamp. After some of the samples failed away from the void region due to cracks initiating from the unpolished sides, the sides of the samples were also polished. After polishing the gauge sections were approximately 1.84 mm thick and 3.86 mm wide.

Two of the samples were visibly warped due to the large internal stresses built up during the manufacturing process. The manufacturer attempted to mechanically rework the specimens, which reduced, but did not eliminate the warpage. This did not appear to affect the results.

Etching of the samples revealed a microstructure that did not appear elongated in any particular direction. The grains across the build direction appeared larger than the grains parallel to the build direction, however, since there is no elongation in the grains parallel to the build direction it is likely that the discrepancy is a result of issues with the etching process. Average grain size, determined using an EBSD scan of the face of the sample, was approximately 65 μm.

Finite element analysis was conducted to determine the static stress concentration of the various void configurations. All available symmetries were exploited allowing the entire void region to be modelled using $1/8^{th}$ models, effectively reducing the number of nodes and elements by a factor of eight. The stress concentrations determined for the four void configurations are summarized below:

- Single void – small: $K_{t\text{-}gross} = 2.05$, $K_{t\text{-}net} \approx 2.00$
- Single void – large: $K_{t\text{-}gross} = 2.17$, $K_{t\text{-}net} \approx 1.93$
- Double void – narrow: $K_{t\text{-}gross} = 2.04$, $K_{t\text{-}net} \approx 1.92$
- Double void – wide: $K_{t\text{-}gross} = 2.03$, $K_{t\text{-}net} \approx 1.92$

The majority of the tests were carried out to a maximum load equivalent to 90% of σ_{yield} at the void surface, taking into account the cross-sectional area loss due to the voids. The stress ratio was R=0.1. Nominal stress amplitude was 407.3 MPa; test frequency was 0.667 Hz.

Of the nine samples tested, 4 failed at the voids due to cracks that initiated from the voids and 4 failed away from the voids due to cracks that initiated from surface defects. One specimen was tested at significantly lower load and was a run-out sample. This sample was later fatigued at higher loads and failed at the void surface. The results of the fatigue testing are presented in Figure 29, Table 7 and Table 8.

One sample failed near simultaneously at two locations. Final failure of the sample occurred away from the void region, however, necking in the void region signified imminent failure. This near simultaneous failure indicated that the stress concentration was similar at both locations; if either had a significantly higher stress concentration then the sample would have failed at that location before signs of failure became visible at the other location. Even when failure did occur at the voids, fracture surface analysis showed that, though the majority of the fatigue cracking was in the region of the voids, cracking had also initiated from the sides of the sample. Though at least half of the samples failed at locations other than the void, the spread in the cycles to failure was relatively small. This suggests that there are inherent defects in the material that have stress concentration values that are similar in magnitude to those of the intentional voids.

The single void – large sample failed at the lowest number of cycles. This is likely due to the configuration having the largest initial flaw size. Fracture surface analysis of a double void sample shows that they fatigue crack growth was similar to the single void samples; cracks initiated from the voids and grew radially. Crack coalescence occurred incidentally as a results of radial crack growth. In double void samples, there was no evidence of the cracks growing preferentially towards the other void.

The DMLS process does not allow for the removal of the powder inside the voids. Examination of the voids after failure revealed that the powder in the voids was partially sintered into an agglomerate and to the sides of the void. Since the powder is only partially sintered it is not expected to carry or transfer significant loads. If it did have an effect, the partially sintered powder likely decreased the void’s effective stress

concentration. The agglomerated powder may have an effect on the shape of the void as it deforms and on the condition of the surface inside the void. Fracture surface analysis shows that some of the locations where the powder was partially sintered to the surface of the void acted as stress concentrations where cracks eventually initiated.

7.2 Microtruss Samples

The microtruss samples consisted of 32 body-centered cubic unit cells in a 4-cell wide, 4-cell high, 2-cell deep arrangement. The unit cells were 5 mm cubes, with 2 mm diameter nodes and 1 mm diameter cylindrical ligaments. The microtruss was attached to a custom grip section, designed to reduce the material volume required to uniformly transfer the load from the MTS Wedge-action Advantage grips to the microtruss. The microtrusses were stress-relieved, solution heat-treated and age hardened according to the process detailed in Section 4.1. They were then shot blasted to remove loose powder from the surface. The surface finish was significantly improved where shot blasting could be applied.

All of the microtrusses had a manufacturing defect where a number of the nodes through the center of the microtruss were split in half parallel to the load direction. These nodes pulled apart during testing, though analysis of the failed microtrusses did not suggest that the defects had any significant effect on the results. Etching of the microtrusses revealed a microstructure that was consistent across the build direction; average grain size was approximately 200 μm and the grains were regularly shaped. Parallel to the build direction, the grains were similarly sized but elongated along the build direction. The

grain size appeared to decrease in the ligament sections and near the edge of the sample, though further testing and imaging is required to confirm this observation.

The maximum stress concentration in the microtruss was calculated by approximating the node as fixed support and the ligament as an angled cantilever beam. The stress concentration was determined to be $K_t = 18.4$. A similar method was used to evaluate the stress concentration in the quarter nodes (at the corners of the microtruss) and determine their mode of failure. The stress concentration was less than that for other ligament-node interfaces though the analysis correctly predicted that the quarter nodes would fail through the node, rather than at the node-ligament interface. The analysis was supported by finite element models, built in Autodesk Inventor and modelled in ABAQUS. Only a single ligament (and attached node portions) were modelled. Fillets were added at the ligament-node interface to better approximate the as-built microtruss; as expected, the radius of these fillets had a significant effect on the stress concentration. For a fillet radius of 0.1 mm, the FE analysis determined the K_t of the microtruss to be 28.37. The K_t from the cantilever beam approximation was used for all the calculations.

Four microtrusses were tested. The first in tension and the remaining three under fatigue loading. The tension test allowed the microtrusses' material properties to be determined. The elastic modulus was 11.74 GPa, the yield stress was 238.5 MPa and the ultimate tensile stress was 323.2 MPa. These are all significantly lower than the property values for the void specimens; this is to be expected given the high stress concentrations and geometry of the microtruss.

The microtrusses generally failed one ligament at the time. The failure of the first ligament increases local stresses and accelerates the failure of subsequent ligaments. A similar failure progression was observed by Li *et al.* [17] in compressive fatigue loading.

The microtruss notch sensitivity factor appears to decrease as the applied stress amplitude decreases. This is likely due to the extent of crack tip blunting that occurs at high stresses which reduces the effective stress concentration in the area around a crack initiation site.

Fracture surface analysis was conducted on the microtrusses using SEM images. The ligament and node fracture surfaces supported the loading assumptions used in the 2D cantilever beam approximation. The analysis highlighted that cracks would initiate from the edge of a ligament, generally from a deep surface defect on the side of the ligament that is loaded in tension, again, similar results were seen by Li *et al.* [17].

Reviewing the ligament failure order for the three fatigue test samples determined that the first ligament failure was always inside the microtruss. Imaging of a range of nodes, located throughout the microtruss, showed that the surface finish of the node deteriorated towards the center of the microtruss. This is likely due to the inability of the shot blasting to penetrate the microtruss geometry. This deterioration in surface finish explains why the first ligament failure was never at the surface; the poor surface finishes of the internal nodes were more favorable sites for crack initiation.

The microtrusses were tested at a range of stress amplitudes, at a stress range of R = 0.1. The stress amplitude vs life data is shown in Figure 69 and summarized in Table 15. Interestingly, the notch sensitivity of the microtruss decreases as the stress amplitude increased, this is likely due to a reduction in crack tip blunting at lower loads.

From the microtruss testing, we conclude that the surface finish of the ligament-node connections plays an important role in the crack initiation and, as a result, fatigue life of the microtruss. Since the geometry of the microtruss restricts the application of mechanical surface finishing processes, the surface finish of the nodes is very much dependent on original DMLS process parameters and machine capabilities.

CHAPTER 8. RECOMMENDATIONS AND FUTURE WORK

Digital image correlation work on the void samples yielded incorrect results, showing the accumulation of compression, rather than tension in the void samples. Though the DIC worked slightly better for the microtruss samples, accurate strain measurements were still elusive. Further investigation into the setup and acquisition of images for DIC is required if the acquired images are to be used quantitatively or if DIC is to be carried out in future tests.

The unpolished sides of the gauge section were stress concentrations that initiated fatigue cracking. Future work should look at quantifying the stress concentration and effect on crack initiation of these as-built surfaces as they cannot be polished if DMLS is used to build complex geometries with internal surfaces or inaccessible surfaces (like the microtruss).

Further testing is also required to quantify the inherent stress concentrations in the samples that caused failure to occur away from the voids. The stress concentrations appear to be of similar magnitude to the voids, therefore it would be interesting to include features with higher stress concentrations in order to try and determine the maximum value of the inherent stress concentrations. Further testing of samples without voids would also help to quantify the inherent defects associated with these DMLS samples.

Finite element analysis of the microtruss ligament demonstrated the strong influence that the fillet radius had on the stress concentration. Further work is required to quantify the fillet radius and then reanalyze the FE model. Future microtruss models should consider including a fillet radius to reduce the stress concentration at this point.

Fracture surface analysis was capable of determining how each microtruss ligament failed. Future work should focus on the ligaments that failed in fatigue and the order in which they failed. EBSD analysis of these ligaments should help to determine if particular microstructural features increased the likelihood of ligament failure, for example, did the ligaments that failed first contain a particular number, or size, of grains, or a particular surface condition.

Further testing is required to confirm the microtruss fatigue test results and conclude that the increase in notch sensitivity at lower loads continues to increase (potentially reaching the notch sensitivity of the void samples). Further analysis of the ligament fracture surfaces and their underlying grain structure would allow a more quantitative approach in determining the likelihood of a particular ligament being the first to fail.

REFERENCES

REFERENCES

1. Gibson, I., D.W. Rosen, and B. Stucker, *Additive Manufacturing Technologies: Rapid Prototyping to Direct Digital Manufacturing*. 1st ed. 2009: Springer Publishing Company, Incorporated.
2. Gibson, L.J. and M.F. Ashby, *Cellular Solids: Structure and Properties*. 2nd ed. 1999: Cambridge University Press.
3. Yang, L., et al., *Additive Manufacturing of Metal Cellular Structures: Design and Fabrication.* Jom, 2015. **67**(3): p. 608-615.
4. Schaedler, T.A., et al., *Ultralight metallic microlattices.* Science, 2011. **334**(6058): p. 962-5.
5. Grandt, A.F., *Fundamentals of structural integrity: damage tolerant design and nondestructive evaluation*. 2003: John Wiley & Sons.
6. Neuber, H., *Kerbspannungslehre (Theory of notch stresses: principles for exact stress calculation)*. 1937, Julius Verlag, Berlin.
7. Peterson, R.E., *Notch sensitivity.* Metal fatigue, 1959: p. 293-306.
8. Tanaka, K., *Engineering formulae for fatigue strength reduction due to crack-like notches.* International Journal of Fracture, 1983. **22**(2): p. R39-R46.
9. ASTM, *E466.19263 Standard Practice for Conducting Force Controlled Constant Amplitude Axial Fatigue Tests of Metallic Materials*. 2015.
10. Gorny, B., et al., *In situ characterization of the deformation and failure behavior of non-stochastic porous structures processed by selective laser melting.* Materials Science and Engineering: A, 2011. **528**(27): p. 7962-7967.
11. McKown, S., et al., *The quasi-static and blast loading response of lattice structures.* International Journal of Impact Engineering, 2008. **35**(8): p. 795-810.
12. Shen, Y., et al., *The Mechanical Properties of Sandwich Structures Based on Metal Lattice Architectures.* Journal of Sandwich Structures and Materials, 2009. **12**(2): p. 159-180.
13. Sypeck, D.J. and H.N.G. Wadley, *Multifunctional microtruss laminates: Textile synthesis and properties.* Journal of Materials Research, 2001. **16**(03): p. 890-897.

14. Brenne, F., T. Niendorf, and H.J. Maier, *Additively manufactured cellular structures: Impact of microstructure and local strains on the monotonic and cyclic behavior under uniaxial and bending load.* Journal of Materials Processing Technology, 2013. **213**(9): p. 1558-1564.

15. Leuders, S., et al., *On the mechanical behaviour of titanium alloy TiAl6V4 manufactured by selective laser melting: Fatigue resistance and crack growth performance.* International Journal of Fatigue, 2013. **48**: p. 300-307.

16. Qi, H., M. Azer, and A. Ritter, *Studies of Standard Heat Treatment Effects on Microstructure and Mechanical Properties of Laser Net Shape Manufactured INCONEL 718.* Metallurgical and Materials Transactions A, 2009. **40**(10): p. 2410-2422.

17. Li, S.J., et al., *Compression fatigue behavior of Ti–6Al–4V mesh arrays fabricated by electron beam melting.* Acta Materialia, 2012. **60**(3): p. 793-802.

18. Cannon, A.H., et al., *MicroStamping for Improved Speckle Patterns to Enable Digital Image Correlation.* Microscopy and Microanalysis, 2015. **21**(SupplementS3): p. 451-452.

19. Aerospace Materials Specification, S.A.E., *AMS5662M Nickel Alloy, Corrosion and Heat-Resistant, Bars, Forgings, and Rings Solution Heat Treated, Precipitation-Hardenable*. 2009.

20. Systems, E.G.E.O., *Material Data Sheet - EOS NickelAlloy IN718.* 2014.

21. HDBK, M., *5J Metallic Materials and Elements for Aerospace Vehicle Structures*, in *Department of Defense Handbook*. 2003.

22. Fournier, D. and A. Pineau, *Low cycle fatigue behavior of inconel 718 at 298 K and 823 K.* Metallurgical Transactions A, 1977. **8**(7): p. 1095-1105.

23. Park, S.J., K.S. Kim, and H.S. Kim, *Ratcheting behaviour and mean stress considerations in uniaxial low-cycle fatigue of Inconel 718 at 649 °C.* Fatigue & Fracture of Engineering Materials and Structures, 2007. **30**(11): p. 1076-1083.

24. Goodman, J., *Mechanics Applied to Engineering*, . 1919, London: Longmans, Green and Co.

25. Smith, K., T. Topper, and P. Watson, *A stress-strain function for the fatigue of metals(Stress-strain function for metal fatigue including mean stress effect).* Journal of materials, 1970. **5**: p. 767-778.

26. Walker, K., *The effect of stress ratio during crack propagation and fatigue for 2024-T3 and 7075-T6 aluminum.* Effects of environment and complex load history on fatigue life, 1970. **462**: p. 1-14.

27. Pilkey, W.D. and D.F. Pilkey, *Peterson's Stress Concentration Factors*. 2008: Wiley.

28. ASTM, *E8/E8M − 15a Standard Test Methods for Tension Testing of Metallic Materials*. 2015.

29. Rickenbacher, L., et al., *High temperature material properties of IN738LC processed by selective laser melting (SLM) technology.* Rapid Prototyping Journal, 2013. **19**(4): p. 282-290.

30. Manfredi, D., et al., *From Powders to Dense Metal Parts: Characterization of a Commercial AlSiMg Alloy Processed through Direct Metal Laser Sintering.* Materials, 2013. **6**(3): p. 856-869.

31. Thijs, L., et al., *A study of the microstructural evolution during selective laser melting of Ti–6Al–4V.* Acta Materialia, 2010. **58**(9): p. 3303-3312.

32. Neuber, H., *Kerbspannungslehre,(1937).* Theory of notch stresses: Principles for exact stress calculation, 1958.

33. Sadowsky, M., E. Sternberg, and H. Chicago, *Stress concentration around an ellipsoidal cavity in an infinite body under arbitrary plane stress perpendicular to the axis of revolution of cavity.* J. appl. Mech, 1947. **14**(3).

34. Smith, F.W. and M.J. Alavi, *Stress intensity factors for a penny shaped crack in a half space.* Engineering Fracture Mechanics, 1971. **3**(3): p. 241-254.

35. Ma, X.-f., et al., *Fatigue and fracture behavior of nickel-based superalloy Inconel 718 up to the very high cycle regime.* Journal of Zhejiang University SCIENCE A, 2010. **11**(10): p. 727-737.

APPENDIX

Material data sheet

EOS NickelAlloy IN718

EOS NickelAlloy IN718 is a heat and corrosion resistant nickel alloy powder which has been optimized especially for processing on EOS M systems.

This document provides information and data for parts built using EOS NickelAlloy IN718 powder (EOS art.-no. 9011-0020) on the following system specifications:

- EOSINT M280 400W System with PSW3.6 and Parameter Set IN718_Performace 1.0
- EOS M290 400W System with EOSPRINT 1.0 and Parameter Set IN718_Performace 1.0

Description

Parts built from EOS NickelAlloy IN718 have chemical composition corresponding to UNS N07718, AMS 5662, AMS 5664, W.Nr 2.4668, DIN NiCr19Fe19NbMo3. This kind of precipitation-hardening nickel-chromium alloy is characterized by having good tensile, fatigue, creep and rupture strength at temperatures up to 700 °C (1290 °F).

This material is ideal for many high temperature applications such as gas turbine parts, instrumentation parts, power and process industry parts etc. It also has excellent potential for cryogenic applications.

Parts built from EOS NickelAlloy IN718 can be easily post-hardened by precipitation-hardening heat treatments. In both as-built and age-hardened states the parts can be machined, spark-eroded, welded, micro shot-peened, polished and coated if required. Due to the layerwise building method, the parts have a certain anisotropy - see Technical Data for examples.

EOS GmbH - Electro Optical Systems

Robert-Stirling-Ring 1
D-82152 Krailling / München

Telephone: +49 (0)89 / 893 36-0
Telefax: +49 (0)89 / 893 36-285
Internet: www.eos.info

Material data sheet

Technical data

General process data

Typical achievable part accuracy [1], [11]	
- small parts	approx. ± 40 – 60 µm approx. ± 1.6 – 2.4 x 10^{-3} inch
- large parts	± 0.2 %
Min. wall thickness [2], [11]	typ. 0.3 - 0.4 mm typ. 0.012 – 0.016 inch
Surface roughness [3], [11]	
- after shot-peening	R_a 4 – 6.5 µm, R_z 20 - 50 µm R_a 0.16 – 0.25 x 10^{-3} inch, R_z 0.78 – 1.97 x 10^{-3} inch
- after polishing	R_z up to < 0.5 µm R_z up to < 0.02 x 10^{-3} inch (can be very finely polished)
Volume rate [4]	
- Parameter Set IN718_Performance (40 µm)	4 mm^3/s (14.4 cm^3/h) 0.88 in^3/h

[1] Based on users' experience of dimensional accuracy for typical geometries, e.g. ± 40 µm (1.6 x 10^{-3} inch) when parameters can be optimized for a certain class of parts or ± 60 µm (2.4 x 10^{-3} inch) when building a new kind of geometry for the first time. Part accuracy is subject to appropriate data preparation and post-processing, in accordance with EOS training.

[2] Mechanical stability is dependent on geometry (wall height etc.) and application#

[3] Due to the layerwise building, the surface structure depends strongly on the orientation of the surface, for example sloping and curved surfaces exhibit a stair-step effect. The values also depend on the measurement method used. The values quoted here given an indication of what can be expected for horizontal (up-facing) or vertical surfaces.

[4] Volume rate is a measure of build speed during laser exposure. The total build speed depends on the average volume rate, the recoating time (related to the number of layers) and other factors such as DMLS-Start settings.

EOS GmbH – Electro Optical Systems
Robert-Stirling-Ring 1
D-82152 Krailling / München

Material data sheet

Physical and chemical properties of parts

Material composition	Ni (50 - 55 wt-%) Cr (17.0 - 21.0 wt-%) Nb (4.75 - 5.5 wt-%) Mo (2.8 - 3.3 wt-%) Ti (0.65 - 1.15 wt-%) Al (0.20 - 0.80 wt-%) Co (≤ 1.0 wt-%) Cu (≤ 0.3 wt-%) C (≤ 0.08 wt-%) Si, Mn (each ≤ 0.35 wt-%) P, S (each ≤ 0.015 wt-%) B (≤ 0.006 wt-%) Fe (balance)
Relative density	approx. 100 %
Density	min. 8.15 g/cm³ min. 0.294 lb/in³

EOS GmbH – Electro Optical Systems
Robert-Stirling-Ring 1
D-82152 Krailling / München

Material data sheet

Mechanical properties of parts at 20 °C (68 °F)

	As built	Heat treated per AMS 5662 [5]	Heat treated per AMS 5664 [6]
Tensile strength [7]			
- in horizontal direction (XY)	typ. 1060 ± 50 MPa (154 ± 7 ksi)		
- in vertical direction (Z)	typ. 980 ± 50 MPa (142 ± 7 ksi)	min. 1241 MPa (180 ksi) typ. 1400 ± 100 MPa (203 ± 15 ksi)	min. 1241 MPa (180 ksi) typ. 1380 ± 100 MPa (200 ± 15 ksi)
Yield strength (Rp 0.2 %) [7]			
- in horizontal direction (XY)	typ. 780 ± 50 MPa (113 ± 7 ksi)		
- in vertical direction (Z)	typ. 634 ± 50 MPa (92 ± 7 ksi)	min. 1034 MPa (150 ksi) typ. 1150 ± 100 MPa (167 ± 15 ksi)	min. 1034 MPa (150 ksi) typ. 1240 ± 100 MPa (180 ± 15 ksi)
Elongation at break [7]			
- in horizontal direction (XY)	typ. (27 ± 5) %		
- in vertical direction (Z)	typ. (31 ± 5) %	min. 12 % typ. (15 ± 3) %	min. 12 % typ. (18 ± 5) %
Modulus of elasticity [7]			
- in horizontal direction (XY)	typ. 160 ± 20 GPa (23 ± 3 Msi)		
- in vertical direction (Z)		170 ± 20 GPa 24.7 ± 3 Msi	170 ± 20 GPa 24.7 ± 3 Msi
Hardness [8]	approx. 30 HRC approx. 287 HB	approx. 47 HRC approx. 446 HB	approx. 43 HRC approx. 400 HB

[5] Heat treatment procedure per AMS 5662:
1. *Solution Anneal* at 980 °C (1800 °F) for 1 hour, air (/argon) cool.
2. *Ageing treatment;* hold at 720 °C (1330 °F) 8 hours, furnace cool to 620 °C (1150 °F) in 2 hours, hold at 620 °C (1150 °F) 8 hours, air (/argon) cool.

EOS GmbH – Electro Optical Systems
Robert-Stirling-Ring 1
D-82152 Krailling / München

Material data sheet

[6] Heat treatment procedure per AMS 5664:
1. *Solution Anneal* at 1065 °C (1950 °F) for 1 hour, air (/argon) cool.
2. *Ageing treatment;* hold at 760 °C (1400 °F) 10 hours, furnace cool to 650 °C (1200 °F) in 2 hours, hold at 650 °C (1200 °F) 8 hours, air (/argon) cool

[7] Tensile testing according to ISO 6892-1:2009 (B) Annex D, proportional test pieces, diameter of the neck area 5 mm (0.2 inch) , original gauge length 25 mm (1 inch).

[8] Rockwell C (HRC) hardness measurement according to EN ISO 6508-1 on polished surface. Note that measured hardness can vary significantly depending on how the specimen has been prepared.

EOS GmbH – Electro Optical Systems
Robert-Stirling-Ring 1
D-82152 Krailling / München

Material data sheet

Mechanical properties of parts at high temperature (649 °C, 1200 °F) [11]

	Heat treated per AMS 5662 [5]	Heat treated per AMS 5664 [6]
Tensile Strength (Rm) [9]		
- in vertical direction (Z)	min. 965 MPa (140 ksi) typ. 1170 ± 50 MPa (170 ± 7 ksi)	typ. 1210 ± 50 MPa (175 ± 7 ksi)
Yield strength (Rp 0.2 %) [9]		
- in vertical direction (Z)	min. 862 MPa (125 ksi) typ. 970 ± 50 MPa (141 ± 7 ksi)	typ. 1010 ± 50 MPa (146 ± 7 ksi)
Elongation at break [9]		
- in vertical direction (Z)	min. 6 % typ. (16 ± 3) %	typ. (20 ± 3) %
Stress-Rupture Properties [10]		
- in vertical direction (Z)	min. 23 hours at stress level 689 MPa (100 ksi)	
	51 ± 5 hours (final applied stress to rupture 792.5 MPa / 115 ksi)	81 ± 10 hours (final applied stress to rupture 861.5 MPa / 125 ksi)

[9] Elevated temperature tensile testing at 649 °C (1200 °F) in accordance with EN 10002-5 (92)

[10] Testing at 649 °C (1200 °F) in accordance with ASTM E139 (2006), smooth specimens. Test method as described in AMS 5662 (3.5.1.2.3.3): "The load required to produce an initial axial stress of 689 MPa (100 ksi) shall be used to rupture or for 23 hours, whichever occurs first. After the 23 hours and at intervals of 8 hours minimum, thereafter, the stress shall be increased in increments of 34.5 MPa (5 ksi)."

[11] Hint: these properties were determined on an EOSINT M 270 IM Xtended and EOSINT M 280-400W. Test parts from following machine types EOSINT M 270 Dual Mode, EOSINT M 280-200W and EOS M 290-400W correspond with these data.

EOS GmbH - Electro Optical Systems
Robert-Stirling-Ring 1
D-82152 Krailling / München

Material data sheet

Thermal properties of parts

	Heat treated per AMS 5662 [4]
Coefficient of thermal expansion	
- over 25 - 200 °C (36 - 390 °F)	approx. 12.5 - 13.0 x 10^{-6} m/m°C approx. 6.9 - 7.2 x 10^{-6} in/in°F
- over 25 - 750 °C (36 - 930 °F)	approx. 16.6 - 17.2 x 10^{-6} m/m°C approx. 9.2 - 9.6 x 10^{-6} in/in°F
Maximum operating temperature for parts under load	approx. 650 °C approx. 1200 °F
Oxidation resistance up to [11]	approx. 980 °C approx. 1800 °F

[12] Based on literature of conventional Ni-alloy with identical chemistry

Abbreviations

typ.	typical
min.	minimum
approx.	approximately
wt	weight

Notes

The data are valid for the combinations of powder material, machine and parameter sets referred to on page 1, when used in accordance with the relevant Operating Instructions (including Installation Requirements and Maintenance) and Parameter Sheet. Part properties are measured using defined test procedures. Further details of the test procedures used by EOS are available on request.

The data correspond to our knowledge and experience at the time of publication. They do not on their own provide a sufficient basis for designing parts. Neither do they provide any agreement or guarantee about the specific properties of a part or the suitability of a part for a specific application. The producer or the purchaser of a part is responsible for checking the properties and the suitability of a part for a particular application. This also applies regarding any rights of protection as well as laws and regulations. The data are subject to change without notice as part of EOS' continuous development and improvement processes.

EOS GmbH – Electro Optical Systems
Robert-Stirling-Ring 1
D-82152 Krailling / München